ABSTRACT

Title of Thesis:	NONLINEAR INTERACTIONS IN PLANAR JET FLOW WITH HIGH FREQUENCY EXCITATION
	Timothy Kreutzfeldt, Master of Science, 2016
Thesis Directed By:	Dr. Inderjit Chopra & Dr. Bryan Glaz Department of Aerospace Engineering

An experimental active flow control study was conducted involving excitation of a tabletop planar turbulent jet with a high frequency piezoelectric actuator. The excitation frequencies considered corresponded to the dissipative subrange of turbulent kinetic energy and were orders of magnitude greater than classical shear layer instability modes. Single-wire and dual-wire hot wire probes were used to determine how excitation induces alterations to bulk flow quantities as well as nonlinear interactions. Differences in flow receptivity to high frequency excitation were investigated by varying the development length of the turbulent jet at a Reynolds number of 8,700 and Strouhal number of 21.3. Excitation of developed turbulent flow yielded larger increases in the energy dissipation rate and higher magnitude velocity power spectrum peaks at the forcing frequency than undeveloped turbulent flow. Further tests with excitation of reduced mean velocity flow at a Reynolds number of 6,600 and a Strouhal number of 27.8 demonstrated that high frequency forcing resulted

in transfer of energy from large to small scales in the turbulent kinetic energy spectrum. This phenomenon appeared to support past literature that indicated that the mechanics of high frequency forcing are fundamentally different from conventional instability-based forcing.

Theoretical arguments are presented to support these experimental observations where it is shown that coupling between the applied forcing and background turbulent fluctuations is enhanced. An eddy viscosity model first proposed under the assumption of instability-based forcing was shown to be an effective approximation for the experimental measurements presented here in which the flow was forced directly at turbulence scales. Dimensional analysis of the coupling between the induced oscillations and the turbulent fluctuations supported experimental findings that receptivity to excitation was increased for forced flow with higher turbulent kinetic energy, higher excitation amplitude, and lower energy dissipation rate. This study is the first to present such results which validate a model that offers theoretical insight into flow control mechanics when directly forcing small scale turbulent fluctuations.

NONLINEAR INTERACTIONS IN PLANAR JET FLOW WITH HIGH FREQUENCY EXCITATION

by

Timothy Kreutzfeldt

Thesis submitted to the Faculty of the Graduate School of the
University of Maryland, College Park, in partial fulfillment
of the requirements for the degree of
Master of Science
2016

Advisory Committee:
Dr. Inderjit Chopra, Chair/Advisor
Dr. Bryan Glaz, Co-Advisor
Dr. James Baeder
Dr. Anya Jones

Acknowledgements

First and foremost, I would like to thank my advisor Dr. Inderjit Chopra for providing me the opportunity to work under his direction for the past two years. He has taught me to think very carefully about each research problem I faced, and that is a skill I will carry with me through the next phase of my career. I would also like to thank my co-advisor Dr. Bryan Glaz for all of his support and advice. Bryan's constant availability to talk about my research project is something I do not take for granted. Furthermore, thank you to the rest of my committee, Dr. James Baeder and Dr. Anya Jones, for your guidance throughout my time at Maryland as both a student and a teaching assistant.

I would like to thank Dr. John Hrynuk for all of his involvement in this research project. When I began work on this experiment last summer, I had hardly an idea of how to detach a compressed air hose. Over a year later, I feel that I have learned an immense amount about how to be a proper experimentalist, and I owe most of that to John—although admittedly it still takes me two or three tries to detach that hose. Thanks also to Mr. Chris Kroninger for his help with academic writing and experimental setup, both of which greatly benefited the writing of this thesis.

Special thanks to Dr. Vikram Hrishikeshavan and Prakruthi Hareesh for all of their help with the manufacturing and testing of my piezoelectric actuators. They each dedicated many hours of their own free time to my project, and I owe each of them a great deal of gratitude.

My sanity throughout graduate school has depended largely on the friendship of other students in the manufacturing building, especially Pete Mancini, Lauren Trollinger, Luke Smith, and Field Manar. I am sure that I would have finished writing my thesis earlier if it were not for your help with brainstorming clever helicopter acronyms, and I have each of you to thank for that. I would be remiss not to also acknowledge the role the rest of the rotorcraft group had in my growth as a student, and I am very appreciative of all of your advice.

Finally, I would like to thank my parents and my girlfriend Theresa for being great listeners throughout all of the successes and frustrations of my graduate career. I truly could not have gotten to this point without you.

Table of Contents

List of Figures

Chapter 1 – Introduction

Active flow control is the process of adding momentum or energy into a system to alter fluid transport behavior. The primary goals of using active flow control devices are improving aerodynamic efficiency with higher lift-to-drag ratio [1], delaying the onset of boundary layer separation [2], and/or reducing aerodynamic noise [3]. Because of these potential benefits, real world implementation of active flow control devices is attractive for a wide range of aerospace applications. Past studies have sought to reduce drag over an aircraft fuselage [4], alter the dynamic stall behavior of an oscillating airfoil [5], and lower the sound pressure levels of aircraft landing gear [6].

Experiments in active flow control have predominantly utilized excitation involving the periodic addition of momentum at frequencies corresponding to an inherent instability in the flow. Some studies have used devices such as oscillating flaps [7] and acoustic loudspeakers [8] to accomplish this. Instability-based forcing studies have demonstrated high effectiveness at delaying boundary layer separation by enhancing turbulent mixing [9]. However, despite potential benefits of implementing active flow control on full-scale aircraft, complex integration issues have restricted devices to laboratory settings [10].

Until recently, excitation at frequencies beyond the range of flow instabilities at Strouhal numbers greater than 5.0 has not been possible due to power and size constraints. However, advances in piezoelectric materials have enabled the development of compact devices with excitation frequencies up to several kHz. Results of active flow control experiments using such devices suggest that forcing at the high

frequencies of small scale structures in turbulent flow is capable of redistributing energy from large scales to small scales [11]. This ability to break apart large scale flow vortices is a distinct advantage over instability-based forcing which has many potential benefits for the future of active flow control (e.g. [12]), though the fundamental mechanics associated with high frequency forcing are not conclusively understood.

High frequency excitation devices have the potential to overcome the hurdles that have prevented fielding of flow control technologies in aircraft—particularly at the scale of unmanned micro air vehicles. However, before introducing vehicle-based applications of modern high frequency flow control devices, the physical mechanisms underlying high frequency excitation must be understood explored further. Past theoretical models characterized low frequency excitation using nonlinear fluid dynamics [13] and energy coupling of large and small scale turbulent structures [14]. However, the viability of such nonlinear interaction based theories to high frequency excitation remains to be established.

1.1 Background

Historic boundary layer control methods utilized continuous suction or blowing to maintain the attachment of flow to a surface [15]. However, these methods were soon eclipsed by excitation methods involving the periodic momentum addition to a flow. Compared to continuous suction or blowing boundary layer control, periodic excitation methods require a small momentum perturbation to impact bulk flow characteristics while saving up to two orders of magnitude in required input energy [16]. For the purposes of this study, two distinct types of flow control are considered: instability-based excitation and high frequency excitation.

1.1.1 Experiments in Instability-Based Flow Excitation

One common excitation method acts upon an inherent flow instability to periodically generate vortices which initiate momentum transport or affect turbulent transition. The earliest periodic excitation experiment found that the transition from laminar flow to turbulent flow over a flat plate boundary layer could be impacted through introduction of a periodic disturbance via a vibrating ribbon, entraining slower moving fluid into the shear layer [17]. This method has been used on laminar boundary layers to initiate a premature transition to turbulent flow, thereby making the flow less susceptible to separation ([18], [19]). Instability-based excitation has also been used in separated flow conditions to induce shear layer reattachment ([20], [21]). In each of these cases, the effects are maximized when the excitation frequency corresponds to a known receptivity or instability. For instance, the well-known Kelvin-Helmholtz instability underpins shear layer studies, wherein periodic perturbation at the boundary between a high and low speed fluid induces vortices which grow as they moves downstream. This phenomenon has been shown to be a useful method for enhancing turbulent mixing for Strouhal numbers up to 5.0 [10].

Excitation methods have varied widely in terms of operating frequency. In the context of flow reattachment studies, it is useful to nondimensionalize the excitation frequency f_e in terms of the Strouhal number (St):

$$St = f_e L / U_0 \tag{1.1}$$

where L is the characteristic length scale (e.g. the hydraulic diameter of a jet) and U_0 is the mean flow velocity [10].

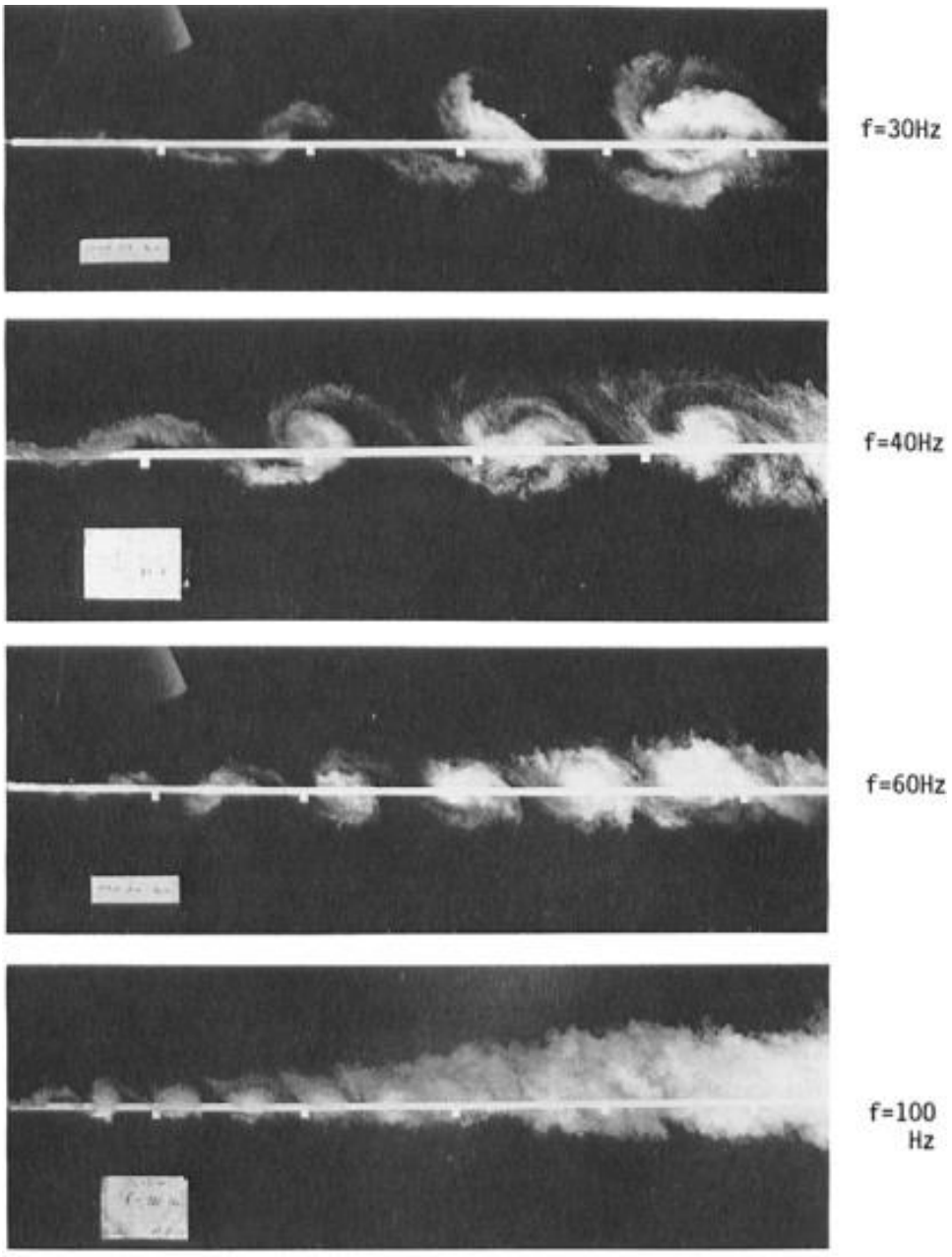

Figure 1.1: Smoke visualization of Kelvin-Helmholtz vortices induced by a vibrating flap at various excitation frequencies [9].

The effects of excitation frequency on instability mechanics have been investigated in multiple studies. Oster et al. [9] performed periodic excitation on a turbulent shear layer via a vibrating flap, which was tested with excitation frequencies

between 20 and 100 Hz ($0.3 \leq St \leq 2.4$). Excitation at all tested frequencies resulted in increased spread rate of the shear layer relative to the unforced flow. The increased spreading was attributed to the growth of the Kelvin-Helmholtz vortices (shown in Fig. 1.1) induced by the excitation. Nishri & Wygnanski [22] examined the periodic momentum required to reattach a separated flow over a deflected flap with varying excitation frequencies. The Reynolds number was varied between 200,000 and 700,000 using flaps of differing percentage of chord lengths. The effects of excitation were found to be independent of Reynolds number, but highly dependent on Strouhal number. The amount of momentum added to the flow to induce flow reattachment was minimized when St = 1.2, and the amount of added momentum to prevent boundary layer separation was minimized when $3.0 \leq St \leq 4.0$. In general, a common theme of these studies was that forcing at frequencies closer to the unstable mode amplified the effects of excitation.

In addition to flow control studies directed toward separation control, others have focused on direct aerodynamic benefits. Bar-Sever [7] positioned an oscillating wire upstream of a NASA LRN (1)-1010 low Reynolds number airfoil and measured the difference in lift coefficient between the forced and unforced cases. For St = 1.8 and Re = 150,000, the lift coefficient was increased up to 12% before stall and up to 38% after stall. Another such study experimented with loudspeakers at varying operating frequencies and found that excitation increases the lift coefficient up to 40% over a GA(W)-1 airfoil for a Strouhal number of 4.0 and a Reynolds number of 600,000 [23]. In this case, the acoustic excitation induced vibration in the walls of the wind tunnel, and the lift-to-drag ratio was maximized when the excitation frequency

corresponded to the resonant mode of the tunnel. However, lift augmentation and drag reduction through coupling with the natural modes of a wind tunnel called into question its applicability outside of controlled environments.

Despite the merits of instability-based active flow control, real world applications remain few and far between, and as a result these approaches have been limited to laboratory settings. Integrating intrusive momentum-injecting devices on potential applications such as turbine engines or helicopter blades creates high manufacturing complexity and the short lifespan of these excitation sources would require short maintenance intervals to remain effective [24]. Compressibility effects drastically lower the lift augmentation capabilities of instability-based excitation, reducing its effectiveness for high Mach number flow [1].

1.1.2 Nonlinear Interactions in Instability-Based Flow Excitation

Theoretical examinations of turbulent statistics have also contributed to the understanding of active flow control and the underlying physical mechanisms. Experimental research in instability-based flow control has focused on the propagation of instabilities such as Kelvin-Helmholtz vortices and their effects on bulk flow characteristics. In contrast, theoretical studies have demonstrated that in addition to flow instabilities, which can be described by linearized stability methods, excitation can also impact the flow through nonlinear interactions.

As a basis for understanding the nonlinear interaction mechanism that motivates this study, it is useful to briefly review the basics of Reynolds averaging. For unforced

turbulent flow, the velocity component in the streamwise direction at a given point and flow location is given by

$$u(x,t) = \bar{u}(x) + u'(x,t) \tag{1.1}$$

where $\bar{u}$ is time-averaged velocity and u' is the velocity fluctuation due to turbulence [25]. The time average of u is defined as

$$\bar{u}(x) = \lim_{T\to\infty} \frac{1}{T} \int_0^T u(x,t)dt. \tag{1.2}$$

This decomposition of the flow velocity in any direction leads to the derivation of the Reynolds-averaged Navier-Stokes (RANS) equations, which expand the general Navier-Stokes equations in terms of the time-averaged and fluctuating quantities. As a consequence of flow nonlinearities, the Reynolds stress r_{12} creates a closure problem such that a turbulence model is required to obtain a solution. In the context of a two-dimensional planar turbulent jet, the closure term is:

$$r_{12} = -\overline{u'v'} \tag{1.3}$$

where v is the spanwise velocity component [25]. The Boussinesq approximation linearizes this term using an eddy viscosity model, yielding

$$r_{12} = -\overline{u'v'} = \nu_t \left(\frac{\partial \bar{u}}{\partial y}\right) \tag{1.4}$$

in which ν_t is the eddy viscosity which varies as a function of streamwise flow location and must be determined empirically [25].

Reynolds & Hussain [13] proposed a "triple decomposition" of the streamwise flow velocity in the context of excitation-based flow control:

$$u(x,t) = \bar{u}(x) + \tilde{u}(x,t) + u'(x,t) \tag{1.5}$$

where $\tilde{u}$ is the coherent wave motion due to an applied simple harmonic excitation. The wave motion is defined as

$$\tilde{u}(x,t) = \langle u(x,t) \rangle - \bar{u}(x) \tag{1.6}$$

in which $\langle u \rangle$ is the phase average of the streamwise velocity. When an excitation source is introduced to the flow, Reynolds & Hussain argued, it causes a component of the decomposed flow velocity to exhibit oscillation at the excitation frequency, and the amplitude and phase of this oscillation can be extracted by phase-averaging this velocity such that

$$\langle u(x,t) \rangle = \lim_{N \to \infty} \frac{1}{N} \sum_{n=0}^{N} u(x, t + n\tau) \tag{1.7}$$

where τ is the period of the excitation. It follows that the adoption of the triple decomposition of the flow velocities results in a new closure problem for the RANS equations. When applied to planar jet flow, the closure term $\tilde{r}_{12}$ is represented by

$$\tilde{r}_{12} = \langle u'v' \rangle - \overline{u'v'}. \tag{1.8}$$

Conceptually, this term signifies the oscillation of the background Reynolds stress as a result of the wave motion caused by the excitation. An inherent assumption in this

interpretation put forth by Reynolds & Hussain [13] is that the wave motion induced by excitation does not impact the background turbulence.

To substantiate their proposed decomposition of the RANS equations, Reynolds & Hussain [13] set up an instability-based flow control experiment in which vibrating ribbons were used to excite a turbulent channel flow (Re = 13,600) at frequencies from 25 to 100 Hz ($0.19 \leq St \leq 0.95$). A single-wire hot wire anemometer was used in conjunction with a wave-form eductor to extract the amplitude and phase of the flow oscillations at the excitation frequency. Planar jet theory was used to approximate the spanwise velocity statistics at each point, allowing the indirect measurement of the closure term $\tilde{r}_{12}$. This closure term was demonstrated to have a non-negligible effect on bulk flow energy and momentum transport, in which the coherent wave components couple to the turbulent fluctuations in a nonlinear manner. It should be noted that the effect on bulk flow transport shown theoretically by Reynolds & Hussain [13] do not invoke any assumptions of linearization. Such mechanisms are fully nonlinear and are clearly differentiated from the more common instability based flow control mechanisms that rely on linearization. In addition to fully nonlinear interaction terms in the bulk flow transport, the coupling of the coherent wave motions with other velocity decomposition components results in modified Orr-Sommerfeld differential equations governing the linearized stability of the Navier-Stokes equations [13]. In a later study, Reynolds & Hussain [26] used multiple models to approximate the form of the closure term and compare to experimental measurements. The model which resulted in the best agreement was an eddy viscosity model taking the form of

$$\tilde{r}_{12} = \langle u'v' \rangle - \overline{u'v'} = \nu_t \left(\frac{\partial \tilde{u}}{\partial x} + \frac{\partial \tilde{v}}{\partial x} + \frac{\partial \tilde{u}}{\partial y} + \frac{\partial \tilde{v}}{\partial y} \right). \quad (1.9)$$

The eddy viscosity ν_t was assumed to be equivalent to the eddy viscosity of the Boussinesq approximation (Eq. 1.4) of the unforced flow. This assumption was based on the frequency of the coherent wave motions being far from small scale turbulence. Such an assumption is valid for many studies in which large instability scales are considered, which correspond to the lowest frequencies found in the turbulence kinetic energy spectrum. The validity of the model in Eq. 1.9 has never been established when considering direct excitation of turbulence scales. Understanding the validity of this model for high frequency forcing is important to understand if the theoretical mechanics put forward by Reynolds & Hussain [13] are valid for this regime.

Theoretical analysis of the nonlinear coupling of turbulent fluctuations have also been used to explain the effects of excitation on bulk flow quantities. Liu [27] studied the development of an instability wave behind a thin body using mean flow momentum and kinetic energy equations. The results suggested that the nonlinear contributions of excitation are inherently linked to the rates of turbulent decay and dissipation as the flow develops downstream. Chan [28] examined the spatial growth of a wave oscillation in a circular turbulent jet using Reynolds & Hussain's [13] triple decomposition (Eq. 1.5) of the Navier-Stokes equations. Experimental data was obtained using loudspeakers to induce pressure oscillations which acted as a basis of comparison for the theoretical model. Both the theoretical and experimental analyses found a direct relationship between amplitude of excitation and the spread rate of the shear layer. Reau & Tumin [29] used the triple decomposition to model the growth of

a perturbation in a turbulent shear flow with actuation $0.10 \leq St \leq 0.25$ and compare it to experimental data from previous studies. The authors used the eddy viscosity model (Eq. 1.9) to approximate the closure term $\tilde{r}_{12}$, and it was found that the theoretical results had better agreement with experimental data for the amplitude of the perturbation when this term was not neglected. As was the case in Reynolds & Hussain [13], none of these studies considered direct high frequency excitation of turbulence scales.

1.1.3 Turbulent Kinetic Energy

In addition to the effects of nonlinearities which appear in the Navier-Stokes equations, excitation may also alter flow characteristics through nonlocal coupling of large and small scale turbulent structures. An understanding of turbulent kinetic energy is important because the distinction between statistically distinct scales of turbulent structures has large implications for the field of high frequency excitation [11].

The wavenumber κ of a turbulent eddy is

$$\kappa = \frac{2\pi}{l} \tag{1.10}$$

where l is the length scale of the structure [25]. This wavenumber scales with frequency such that low frequencies correspond to large eddies and high frequencies correspond to small eddies.

The turbulent kinetic energy $E(\kappa)$ contained in a given wavenumber differs across scales due to anisotropy in large eddies and the increased effect of viscosity for

small eddies. Kolmogorov's 1941 hypothesis of local isotropy states that for sufficiently high Reynolds number, all turbulent eddies above a certain wavenumber are statistically isotropic and independent from the directional biases of larger structures [25]. In other words, large scale turbulence structures are affected by directionality of the mean flow such that statistically, the magnitude of the velocity fluctuation in any given direction may be larger than other directions. Kolmogorov argued that at a certain length scale, this directionality disappears and the average magnitude of the velocity fluctuation is the same in every direction. The corresponding wavenumber of this scale marks the end of the energy-containing subrange of turbulent kinetic energy. It is important to note that the unstable modes targeted by instability-based excitation methods correspond to the energy-containing subrange.

Within the range of local isotropy, Kolmogorov's first similarity hypothesis states that the statistics of a turbulent eddy with a given wavenumber are solely dependent on the energy dissipation rate ε and the viscosity ν [25]. Conceptually, the energy dissipation rate signifies the rate at which energy is transferred from large scale turbulent structures to small scale turbulent structures. It follows that a characteristic length scale η can be derived using dimensional analysis:

$$\eta = \left(\frac{\nu^3}{\varepsilon}\right)^{1/4} \tag{1.11}$$

This length scale, termed the Kolmogorov length scale, corresponds to the smallest eddies which exist at a given flow location before extinction due to viscosity.

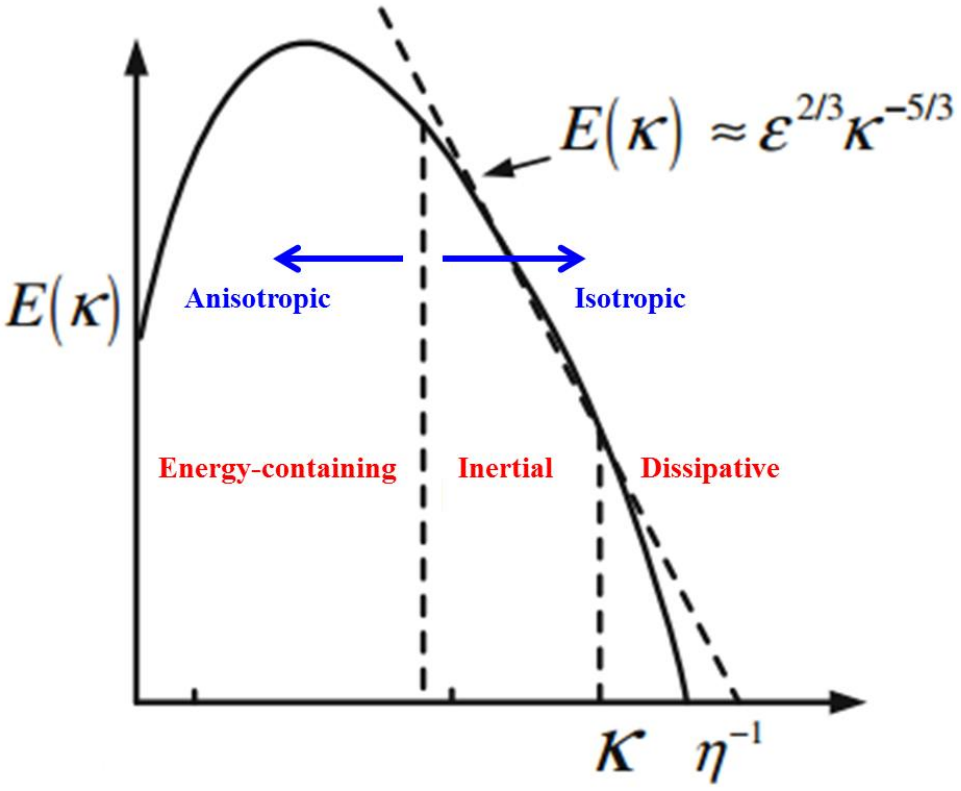

Figure 1.2: Plot of turbulent kinetic energy versus wavenumber (adapted from [30]).

Likewise, dimensional analysis can also be used to derive the form of the turbulent kinetic energy. Kolmogorov's second similarity hypothesis identifies a range of wavenumbers corresponding to eddies which are much smaller than the anisotropic eddies in the energy-containing range and much larger than Kolmogorov scale structures [25]. Within this range, the turbulent statistics are independent of viscosity, and $E(\kappa)$ takes the form of

$$E(\kappa) = C_\kappa \varepsilon^{2/3} \kappa^{-5/3}. \tag{1.12}$$

where C_κ is the Kolmogorov constant. This equation became known as "Kolmogorov's 5/3 Law." The inertial range can be highlighted experimentally by plotting the turbulent kinetic energy spectrum as a function of wavenumber on a log-log scale as demonstrated in Fig. 1.2.

In the context of active flow control, Kolmogorov's theories have been disputed by numerous studies suggesting that large and small scale turbulent structures are in fact inherently coupled, even at very high Reynolds numbers. Yeung & Brasseur [31] examined the effects of anisotropic forcing in the energy-containing range on the energy transfer function to separate scales using direct numerical simulation (DNS). It was discovered that structures at small scales were increasingly affected by energy transfer from structures in the energy-containing region, and that this effect persisted for high Reynolds number flow. In a further study, Yeung, Brasseur, & Wang [14] found that turbulent scales of motion were "dynamically coupled over large separations in scale, the strength of the coupling increasing with the relative energies of the large- and small-scale modes." These nonlocal interactions were strongest between the energy-containing range and the dissipative range of turbulent kinetic energy. A more recent DNS study calculated that an average of 20% of the total energy flux in a turbulent flow with forcing applied at multiple wavenumbers in the energy-containing region was due to nonlocal interactions across scales [32].

Whereas instability-based flow excitation has enacted forcing within the energy containing subrange of the turbulent kinetic energy spectrum, experiments in high frequency excitation have targeted forcing of the inertial and dissipative subranges.

Kolmogorov's hypotheses suggest a preliminary explanation for why excitation would impact structures at these scales differently. Furthermore, computational studies looking into the isotropy of small scale structures have shown that instability-based excitation results in coupling between structures in the energy-containing range and the dissipative range. A possible implication of this phenomenon is that the same coupling mechanism could be used to impact structures in the energy-containing subrange through excitation of dissipative subrange structures.

1.1.4 High Frequency Actuators

Experiments in instability-based excitation have predominantly studied active flow control with Strouhal numbers less than 5.0. A main reason for the narrow body of work at high frequencies is that physical actuators designed for high frequencies were not previously available due to high power requirements at those frequencies. However, recent advances in piezoceramic materials have enabled excitation devices to be driven at high amplitudes at frequencies well beyond typical instability scales.

Experiments in high frequency excitation have employed two categories of flow control devices: piezoelectric flaps and synthetic jet actuators (SJAs). Piezoelectric flap actuators generally consist of piezoelectric material mounted on a cantilever beam which vibrates to induce vortices in the flow [33]. Although the operating frequency must be tuned to the natural frequency of the beam to produce high amplitude oscillations, they are compact and simple to design and manufacture, enabling production of actuators corresponding to many different operating frequencies of interest [34].

Synthetic jet actuators (also known as zero-net mass-flux actuators) involve a piezoelectric diaphragm embedded on a cavity to alternatingly absorb and expel fluid [33]. Similar to piezoelectric flaps, synthetic jets are resonance-based devices which can only produce high amplitude flow oscillations when operated in resonance with the natural frequency of the piezo disc. Synthetic jets are relatively more complex to design and manufacture than piezoelectric flaps, making it more difficult to target multiple specific operating frequencies of interest [35].

1.1.5 Experiments in High Frequency Flow Excitation

An important set of active flow control studies with excitation frequencies beyond the range of flow instabilities was done by Wiltse & Glezer [36]. Inertial range forcing of a planar turbulent jet was investigated using a piezoelectric flap actuator mounted on a steel cantilever. It was found that excitation at St = 5.4 made the turbulent flow less susceptible to instabilities induced by low-frequency excitation. In a later study Wiltse & Glezer [11] used an optimized piezoelectric flap actuator to enact excitation on the low end of dissipative range turbulence frequencies (St = 29.5) of a planar turbulent jet. As shown in the velocity power spectra in Fig. 1.3, the excitation resulted in "enhanced energy transfer from the large to the small scales" and "a substantial increase in the dissipation and in the decay rate of turbulent kinetic energy." This method of flow control was referred to by Wiltse & Glezer [11] as "direct excitation" of small scale turbulent structures as opposed to "indirect excitation" of small scale structures via the breakdown of large structures excited at an instability frequency. These results provide compelling evidence that coupling between kinetic

energy scales can act as mechanisms for affecting turbulent flows when forcing beyond instability frequencies. Wiltse & Glezer focused on experimental characterization of this phenomena rather than a theoretical model underpinning the mechanics; no explicit connection with nonlinear interactions (e.g. [13]) was made.

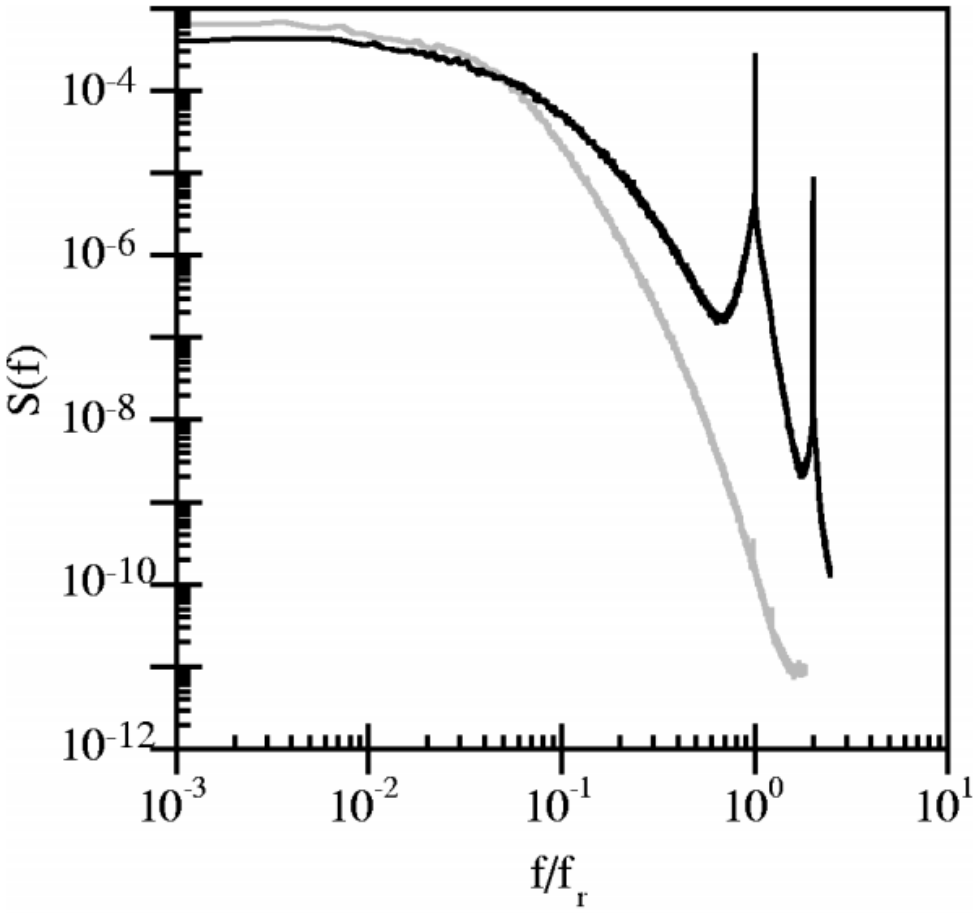

Figure 1.3: Velocity power spectra of unforced (grey) and forced (black) turbulent shear flow [11].

More recent experimental studies in high frequency excitation have utilized synthetic jets as an actuation source. A particle image velocimetry (PIV) study of turbulent flow over a backward-facing step with inertial range excitation (St = 13.1)

was performed with variable amplitude synthetic jets at the base of the step [37]. As shown in Fig. 1.4, despite adding more turbulent kinetic energy to the system, high momentum excitation resulted in greater reduction of vorticity downstream of the excitation than low amplitude forcing. This corresponded with lower total turbulent kinetic energy, lower turbulent production, and higher dissipation downstream of the excitation.

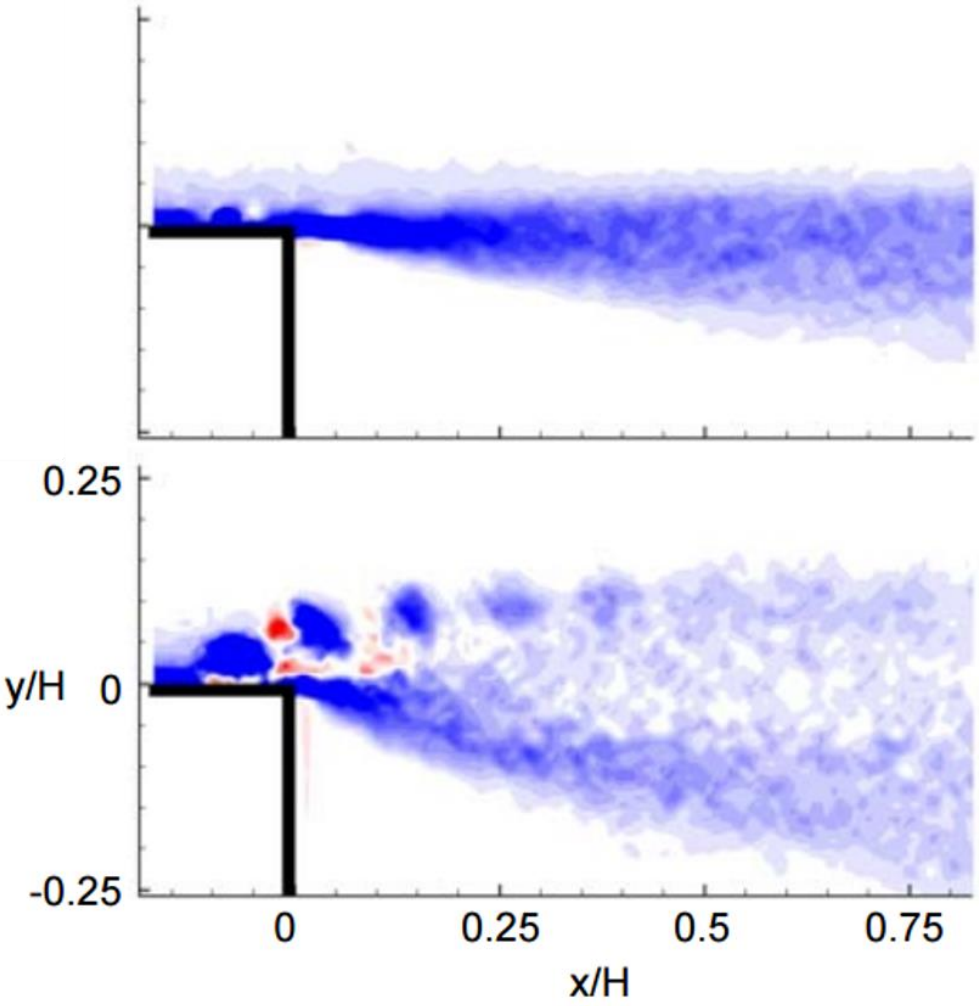

Figure 1.4: Vorticity plots for turbulent flow excited with low amplitude (upper) and high amplitude (lower) excitation [37].

A follow-on experiment studied differences in the flow behavior near the excitation and far downstream of the excitation [38]. Measurement locations nearest the excitation showed less energy at large scales and more energy at small scales relative to the baseline flow, and these differences were attributed to higher increases in production and dissipation. The main effect of the forcing far downstream of the excitation was less energy in the turbulent scales associated with instabilities, which was consistent with past findings that large scale instabilities are suppressed as a result of high frequency excitation [36]. Glezer, Amitay, & Honohan [39] compared low frequency (St = 0.7, 1.1, 2.05, 3.3) and high frequency (St = 10) synthetic jet excitation of flow over a cylinder. The introduction of high frequency forcing to the leading edge of the cylinder resulted in higher lift and lower drag relative to the effect of the low frequency, instability-based forcing. This finding warrants further examination to determine the viability of implementing high frequency actuators on aircraft.

Advances in acoustic technology also opened opportunities for sound-based high frequency excitation sources. The development of devices such as the nanomaterial actuators described by Xiao et al. [40] have demonstrated broadband actuation potential which are particularly effective at high frequencies. Furthermore, such materials have the additional benefit of being able to conform to aerodynamic surfaces. Recently, a large eddy simulation (LES) study motivated by the potential of new nanomaterial based actuators was conducted involving high frequency acoustic forcing of turbulent flow over a hump [12]. It was concluded that dissipative scale acoustic forcing at 110 dB broke up large scale vortical structures and altered the mean flow pressure region in the wake, resulting in significant drag reduction over the hump.

The study provided initial evidence for the viability of active flow control using acoustic-based actuators. However, experimental validation of high frequency acoustic actuators is necessary before aircraft-based applications can be pursued. Perhaps more importantly, theoretical explanations to compliment the LES results of Yeh et al. [12] are needed before further research investment can be justified for high frequency forcing actuator development, nanomaterial or otherwise.

Further experimental exploration of high frequency excitation has identified beneficial effects of forcing beyond potential aerodynamic efficiency applications. High frequency excitation has been demonstrated to reduce aeroacoustic noise. McGrath & Shaw [41] implemented a high frequency tone generator in a supersonic cavity flow (Re = 2,000,000) with operating frequencies two orders of magnitude above the dominant cavity frequency. Their results showed that acoustic excitation was able to reduce sound pressure levels at the dominant cavity frequency up to 30 dB. This result was supported by Stanek et al. [42], who observed acoustic suppression up to 28 dB for a cavity flow (Re = 800,000) excited by synthetic jet actuators. High frequency actuators also have implications on the field of aero-optics. A study examining the optical access of a laser propagating through turbulent flow in a wind tunnel encountered fewer optical aberrations while pulsing plasma through the flow at both 5 kHz and 12.5 kHz [43]. The authors justify this result by claiming that the excitation suppressed the formation of large scale turbulent structures.

1.1.6 Simulations of High Frequency Flow Excitation

Multiple studies have sought to explain the physical mechanisms responsible for the effects of high frequency excitation. Cain & Rogers [44] performed a DNS study of low and high frequency excitation which showed that the reduced turbulent kinetic energy at large scales coincided with a substantial decrease in the production rate and increase in the dissipation rate. It was found that the effects of high frequency excitation were stronger and longer lasting in transitional flows relative to fully turbulent flow. The authors hypothesized that the reason behind the reduction in energy at large scales was due to nonlinear coupling between large and small scales—consistent with the ideas of Yeung, Brasseur & Wang [14] on nonlocal interactions. However, a later study by Stanek et al. [42] contested this explanation, claiming that high frequency excitation "modifies the inviscid stability properties of the mean flow in such a way as to stabilize the mean shear flow and prevent the growth of large-scale instabilities in the first place." According to this theory, the reason why flow subjected to high frequency excitation is less susceptible to instability-based excitation is that the two types of excitation have opposing effects on the stability of turbulent flow; i.e., one cannot both suppress and encourage the stability of a turbulent shear layer at the same time.

This stabilization theory suggests that the effects of high frequency excitation on turbulent flow can be explained by linear stability analyses of mean velocity profiles rather than by comprehensive investigation of nonlocal interactions. Stanek et al. [45] later used an LES-RANS hybrid model to show that this stabilization effect is due to interactions between adjacent spanwise vortices, which only occur when they are pulsed above a certain critical frequency. A computational study by Dandois, Garnier,

& Sagaut [46] on a separated flow was performed to compare the separation length between flow excited at low and high frequencies. Their results show that the separation length decreases with low frequency excitation and increases with high frequency excitation. The authors attribute this result to alterations to the stability of the mean velocity profile, supporting the findings of Stanek et al. [42].

1.2 Objective

Despite the emergence of various types of high frequency actuators, high frequency excitation is still a relatively unsettled area of active flow control research with multiple contradictory theories. The current study aims to better understand the nonlinear interactions induced by high frequency excitation and to inform future dissipative scale forcing studies. Limited experimental results in high frequency excitation warrant further investigation of the effects of mean velocity, stage of turbulent development, and excitation amplitude to better understand the fundamental physics of high frequency forcing. While past research has identified multiple physical environments under which high frequency excitation is effective, the conditions under which such excitation is ineffective remain unclear. Furthermore, analysis of the nonlinear dynamics of forced flows has the potential to introduce theoretical models to better understand experimental results. This study sought to investigate the effects of high frequency excitation of turbulent shear flow through spectral analysis of the streamwise flow velocity and through nonlinear interaction analyses which were developed for instability-based excitation methods.

The experimental approach for this study involved the high frequency excitation via a piezoelectric actuator of planar turbulent jet flow with variable development length. Analysis of this flow included spectral analyses of the streamwise velocity at locations within the shear layer. Single-wire hot wire anemometer measurements were used to analyze bulk flow quantities and velocity power spectra at locations within the shear layer. Dual-wire hot wire anemometer measurements were then used to calculate nonlinear closure terms at flow locations which were most susceptible to excitation. Measurement of this term was critical to developing theoretical understanding of nonlinear interaction mechanisms, as no such measurements exist for turbulent flow under direct small scale turbulence forcing.

Specific objectives of this thesis were to:

i. Analyze the susceptibility of turbulent shear flow to high frequency excitation at different stages of turbulent development.
ii. Determine optimal flow conditions to maximize the power spectral density peak of the forced flow by varying the mean flow velocity and excitation amplitude.
iii. Experimentally measure the $\tilde{r}_{12}$ closure term in the context of direct excitation of small turbulence scales.
iv. Generate a linear model for the $\tilde{r}_{12}$ closure term and compare it to experimental measurements.

Chapter 2 – Experimental Setup

Turbulent planar jet flow is considered as a canonical system to study the effects of turbulence scale forcing on flow transport quantities [47]. A turbulent duct was powered by compressed air exited to the atmosphere to form the free turbulent planar jet. Single-wire and dual-wire hot wire anemometers were used to measure velocities at a range of locations up to 2.5 duct hydraulic diameters downstream of the jet exit. High frequency forcing was applied near the exit using a piezoelectric actuator, and measurements were obtained to characterize the evolution of the forced and unforced flow.

2.1 Turbulent Jet

Experiments were conducted at the U.S. Army Research Laboratory (ARL: Aberdeen Proving Ground) Micro Aeromechanics Wind Tunnel (MAWT) facility. The jet was 3D-printed using a Fortus 400mc 3D printer using ABSM30 thermoplastic. A diagram of the turbulent jet used in the experiments is shown in Fig. 2.1.

The jet was powered by standard building compressed air and controlled with a standard regulator valve. The compressed air jet entered an expansion section that contained a grid structure to uniformly expand the flow before the contraction section. The following contraction section had a contraction ratio of 25:1 with a wind-tunnel-like contraction shape. The purpose of the expansion and contraction sections was to convert the compressed air jet into uniform flow entering the duct. After exiting the contraction section, the turbulent flow was developed in a square duct with a hydraulic diameter of D_H = 2.54 cm.

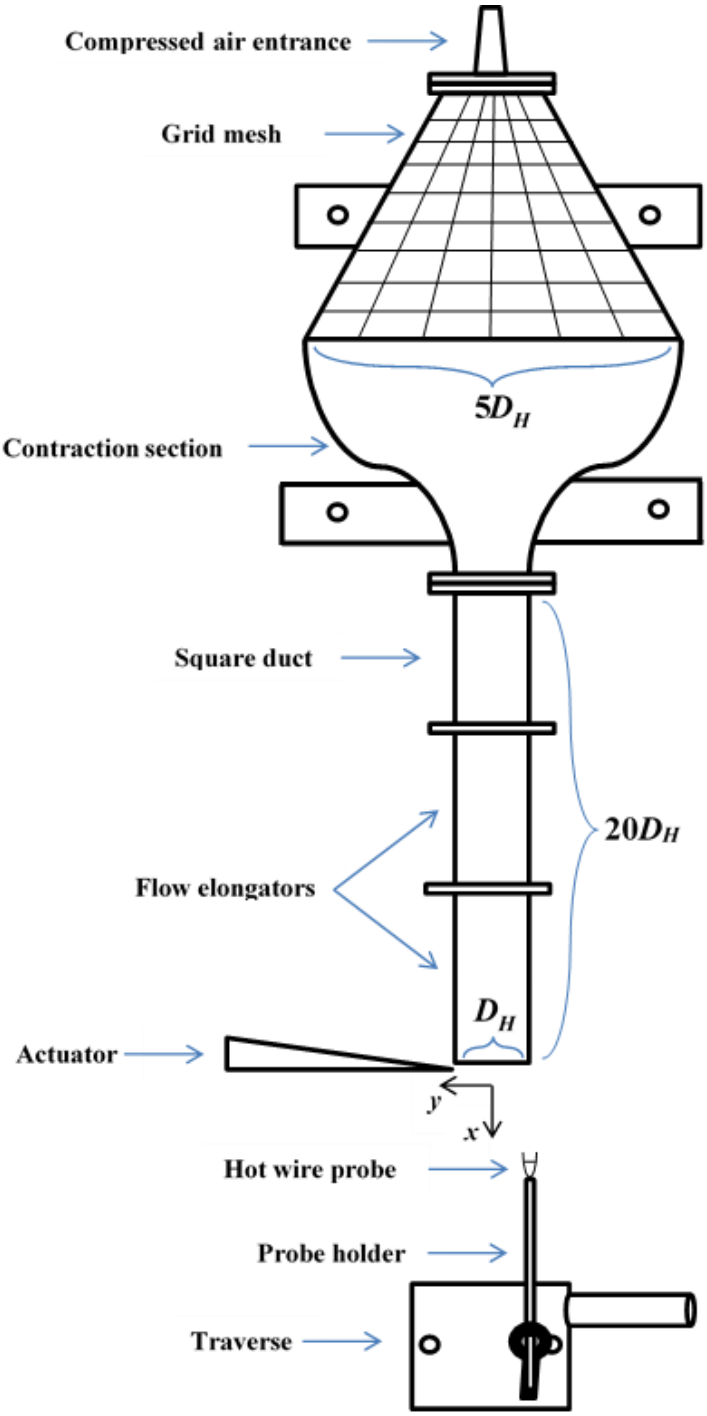

Figure 2.1: Diagram of turbulent jet setup with D_H = 2.54 cm.

The length of the duct could be varied using attachable duct sections to elongate the flow and vary the mean velocity profile at the exit. Without using the flow

elongators, the length of the duct was $6D_H$ and the flow was in the transitional stage of turbulent development. With the additional duct sections attached, the length of the duct was $20D_H$ resulted in nearly fully developed turbulent flow at the jet exit [48]. The jet was assumed to be symmetric and to have only streamwise and spanwise flow along the plane at the vertical midpoint of the duct. Fluctuations in the out-of-plane direction were assumed to be negligible.

2.2 Velocity Measurements

Flow velocity measurements were taken using a Dantec MiniCTA hot wire anemometer (HWA) system with a miniature straight single-wire probe (Dantec 55P11) and a straight dual-wire X-probe (Dantec 55R51). The wires of the dual-wire probe were separated by 1.0 mm spacing and aligned at a 45 degree angle with respect to the probe axis. The anemometer system manufacturer listed a response frequency of 10 kHz and typical noise of 1-2 mV on the output voltage signal.

The hot wire anemometers were calibrated before each experiment using a StreamLine Pro Automatic Calibrator. The hot wire anemometer was placed at the exit of the calibrator, which used compressed air to emit an extremely low turbulence free jet with precisely set mean velocity using pressure and temperature transducers. The calibration process enabled the voltage signal which was produced by the hot wire anemometer to be converted into a velocity signal. The mean velocity was variable between 0.5 m/s and 300 m/s at the jet exit and the turbulence intensity on the jet centerline was less than 0.25% for mean velocities lower than 20 m/s.

For the single-wire velocity calibration, the jet mean velocity was sampled at 0.5 and 0.75 m/s and then varied linearly between 1 and 20 m/s. A fourth-order

polynomial fit was performed on these data as shown in Fig. 2.2 to yield a single-wire probe calibration curve. This curve was used to convert single-wire voltage E into measurements of the streamwise flow velocity U.

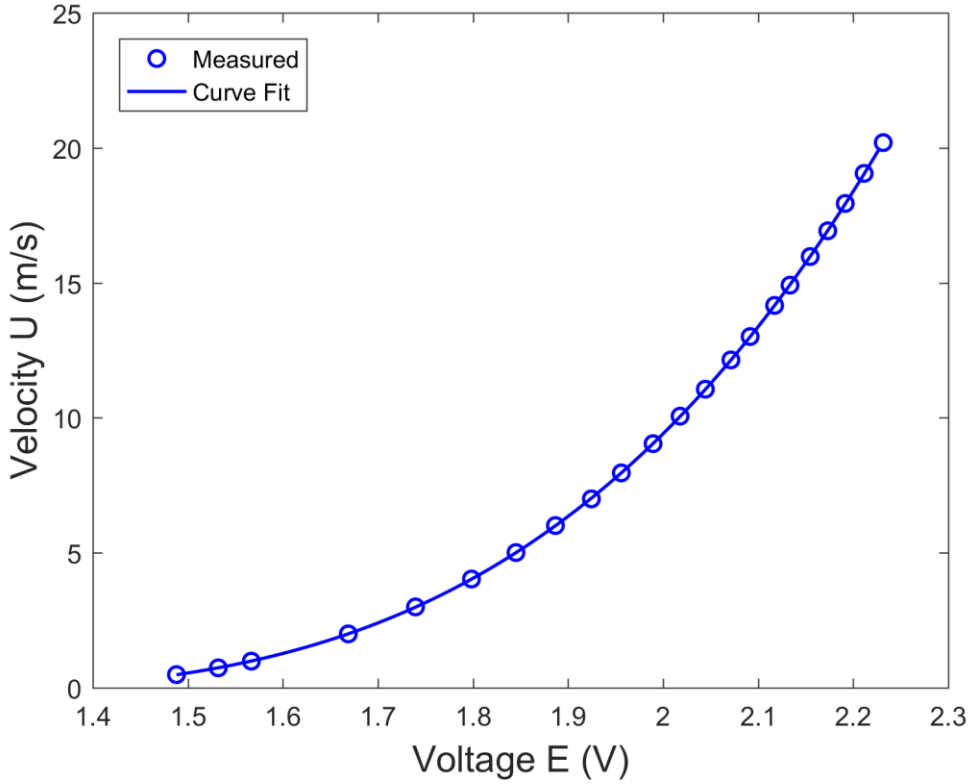

Figure 2.2: Single-wire probe velocity calibration curve.

Calibration of the dual-wire probe consisted of a velocity calibration and a directional calibration. For the velocity calibration, the dual-wire probe was positioned at the centerline of the jet exit such that the probe axis was parallel to the direction of the flow. The mean velocity was varied logarithmically between 0.5 m/s and 15 m/s. Two separate fourth-order polynomial curve fits were used to convert the voltages E_1

and E_2 of each wire into the calibrated velocities U_{cal1} and U_{cal2}, respectively. The velocity calibration curves of the dual-wire probe are shown in Fig. 2.3.

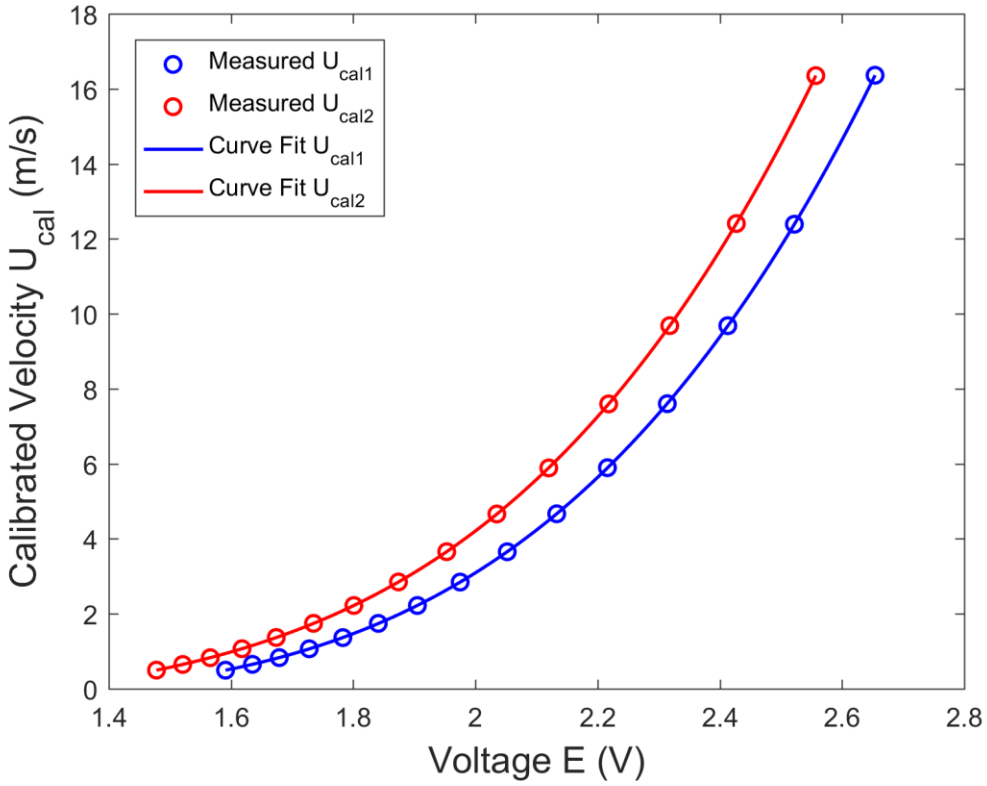

Figure 2.3: Dual-wire probe velocity calibration curves.

It was necessary to convert the dual-wire probe measurements from the wire-axis frame to the flow-axis frame. Velocity calibration provided the calibration velocities U_{cal1} and U_{cal2} which were obtained from the voltage measured by each wire. The calibration velocities were related to the wire-axis velocities U_1 and U_2 such that

$$U_1 = \frac{\sqrt{2}}{2}\sqrt{(1 + {k_2}^2){U_{cal2}}^2 - {k_2}^2{U_{cal1}}^2} \tag{2.1}$$

$$U_2 = \frac{\sqrt{2}}{2}\sqrt{(1 + {k_1}^2){U_{cal1}}^2 - {k_1}^2{U_{cal2}}^2} \tag{2.2}$$

in which k_1 and k_2 are the yaw coefficients for the respective wires. The objective of the directional calibration was to calculate the yaw coefficients to enable measurement of the wire-axis velocities. When the yaw coefficients are known, the wire-axis velocities can be converted into the respective in-plane and out-of-plane velocity components U and V:

$$U = \frac{\sqrt{2}}{2}U_1 + \frac{\sqrt{2}}{2}U_2 \tag{2.3}$$

$$V = \frac{\sqrt{2}}{2}U_1 - \frac{\sqrt{2}}{2}U_2. \tag{2.4}$$

For directional calibration, the dual-wire probe was initially positioned at the centerline of the calibrator jet exit parallel to the direction of the flow. The mean velocity of the jet U_0 was set to 4.8 m/s, which was the expected mean velocity of the turbulent planar jet flow. The angle of incidence of the probe α with respect to the jet exit was varied using a Dantec ISEL lightweight traverse. Velocity measurements were obtained for angles of incidence between -40 and 40 degrees, after which accuracy of the dual-wire probe significantly degrades. The wire-axis velocities were expected to vary with α such that

$$U_1 = U_0 \sin\left(\alpha + \frac{\pi}{4}\right) \tag{2.5}$$

$$U_2 = U_0 \sin\left(-\alpha + \frac{\pi}{4}\right). \tag{2.6}$$

The values of k_1 and k_2 were selected to minimize the difference between the measured values (Eqs. 2.1 and 2.2) and the expected values (Eqs. 2.5 and 2.6) of the wire-axis velocities. The measured and expected values of U_1 and U_2 are shown in Fig. 2.4 for the calibrated yaw coefficients k_1 = 0.2889 and k_2 = 0.2734.

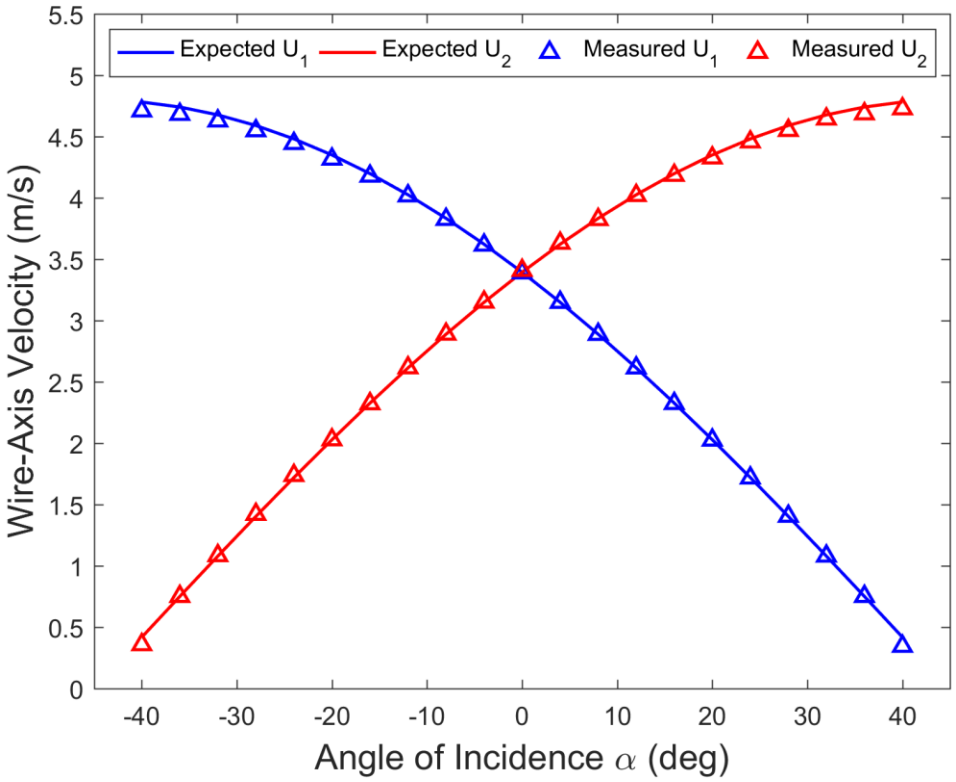

Figure 2.4: Dual-wire probe directional calibration curves.

2.3 Flow Characterization

The single-wire probe was used to obtain streamwise velocity measurements and velocity power spectra of the forced and unforced flows. The dual-wire probe was used to simultaneously measure the streamwise and spanwise flow velocity in order to

obtain the Reynolds stresses of the unforced flow and coherent wave oscillations of the forced flow at select locations.

Hot wire probe orientation was an important factor to ensure only downstream velocity was measured. For each experiment, the probe was positioned such that the probe was vertically centered on the jet exit. The probe was attached onto a linear traverse, which was used to precisely alter its spanwise position. The error in probe location was assumed to be a function of error in the traverse and potential misalignment of the probe holder. A maximum misalignment angle of 0.25 degrees was assumed, making the error in spanwise probe location approximately 0.87 mm (~$0.034D_H$). The downstream distance of the probe was fixed for each set of spanwise measurements using markings on the probe holder spaced 6.35 mm apart. The width of each marking was 1.50 mm. Thus, the error in downstream measurement locations was assumed to be 0.75 mm (~$0.031D_H$) based on a maximum positional misalignment of half the width of the marking.

The mean flow velocity at the jet exit U_0 was determined using the hot wire probe positioned at the jet exit on the centerline. Based on the expected noise in the output voltage signal of 1-2 mV, the maximum assumed error in the mean velocity was 0.06 m/s for a mean velocity of 6.5 m/s.

2.3.1 Single-wire Hot Wire Measurements

Single-wire probe data were collected within a two-dimensional measurement domain as shown in Fig. 2.5 with the streamwise direction represented by x and the spanwise direction represented by y. The spanwise centerline of the jet was represented

by y/D_H = 0 and the wall of the jet exit was represented by y/D_H = 0.50. The closest downstream location for which measurements were taken was x/D_H = 0.25. Velocity measurements were taken at 10 streamwise distances between $0.25 \leq x/D_H \leq 2.50$. At each streamwise distance, measurements were taken at 16 spanwise locations between $0 \leq y/D_H \leq 0.75$. For the unforced flow symmetry of the jet was assumed, and while actuation was asymmetric, it was assumed that actuation effects were minimal opposite the jet centerline for the measurement region in Fig. 2.5. As such, measurements for the opposite side of the jet which were represented by $-0.75 \leq y/D_H \leq 0$ were not recorded.

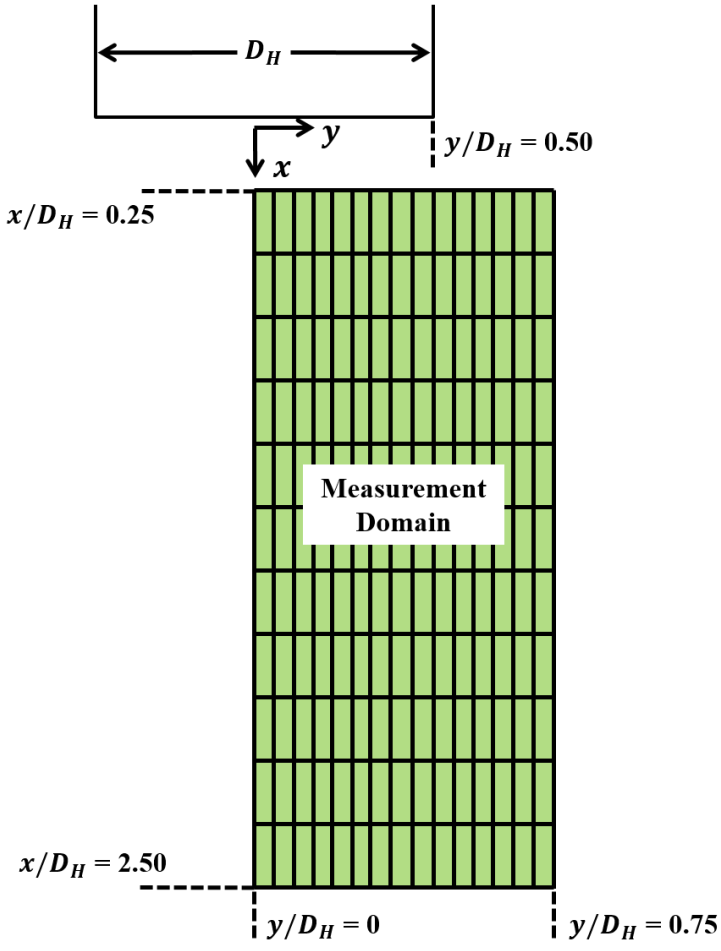

Figure 2.5: Measurement domain for single-wire flow characterization.

Single-wire probe velocity measurements for the unforced and forced flows were recorded at each measurement location at 25 kHz for 10 seconds. Because of the orientation of the probe wire, these measurements were assumed to be the streamwise velocity u and contain no out of plane components. Velocity measurements were analyzed using the Reynolds & Hussain [13] triple decomposition as a function of streamwise location, spanwise location, and time.

$$u(x,y,t) = \bar{u}(x,y) + \tilde{u}(x,y,t) + u'(x,y,t). \tag{2.7}$$

The wave oscillation $\tilde{u}$ was referenced to the frequency of excitation and was assumed zero for the unforced flow.

The single-wire probe was also used to obtain bulk flow quantities in addition to decomposition of the streamwise velocity. Energy dissipation rate at each point in the flow was evaluated using Taylor's hypothesis:

$$\varepsilon = 15\nu \frac{1}{\bar{u}^2} \overline{\left(\frac{\partial(\tilde{u}+u')}{\partial t}\right)^2} \tag{2.8}$$

in which ν is the kinematic viscosity of air, which was 18.3 μPa·s in the laboratory. The Kolmogorov scale of turbulent structures η (i.e., the length scale of the smallest eddies in the flow) was calculated at all flow locations using Eq. 1.11 with the energy dissipation rate obtained from Taylor's hypothesis. Wiltse & Glezer [11] define the passage frequency f_l for turbulent structures with characteristic size l and subsequently the passage frequency f_η for Kolmogorov scale structures as

$$f_l = \frac{U_0}{2l} \tag{2.9}$$

$$f_\eta = \frac{U_0}{2\eta}. \tag{2.10}$$

Conceptually, the passage frequency approximates the excitation frequency which is required to directly interact with turbulent structures of a known length scale. It follows that the Kolmogorov scale passage frequency indicates the highest excitation frequency which is capable of interacting with turbulent structures which exist in the flow.

2.3.2 Dual-wire Hot Wire Measurements

After completing the single-wire hot wire measurements, the dual-wire probe was used to target specific flow locations of interest. The goal of the dual-wire probe measurements was to enable experimental measurements of the unforced and forced nonlinear closure terms (Eqs. 1.3 and 1.8, respectively) through simultaneous measurements of the streamwise and spanwise velocity components.

For the unforced flow, the measurement domain consisted of one streamwise location at x/D_H = 1.0 and 16 streamwise locations between $0 \leq y/D_H \leq 0.75$. The dual-wire probe was positioned such that the wire spacing corresponded to the out-of-plane axis of the jet in order to measure only the streamwise and spanwise velocity components. Velocity measurements were taken for 60 seconds at 25 kHz at each measurement location. After converting the hot wire voltage signals into velocity components in the jet frame of reference, the velocities were decomposed into mean, wave oscillation, and fluctuating components as shown in Eq. 2.7. The wave oscillation term was assumed zero for the unforced case.

Measurements of the spanwise velocity gradient were necessary to calculate the Boussinesq approximation of the Reynolds stress (Eq. 1.4). The gradients were calculated at each location using a central difference approximation.

$$f'(x) = \frac{f(x+h) - f(x-h)}{2h} \tag{2.11}$$

where h is the spacing between points, which was 1.27 mm ($0.05D_H$) for this calculation. The spanwise gradient was then multiplied by the flow eddy viscosity ν_t, yielding the Boussinesq approximation for the Reynolds stress. A sweep of magnitudes for the eddy viscosity was performed in order to minimize the error ε_v in the approximation such that

$$\varepsilon_v = \sum_j -\overline{u_j' v_j'} - \nu_t \frac{\partial \overline{u}_j}{\partial y}. \tag{2.12}$$

For the forced flow, the measurement domain consisted of one measurement location (x/D_H = 1.0, y/D_H = 0.40) and four surrounding points on the streamwise and spanwise axes in order to calculate the gradients. A large ensemble of points was necessary to obtain a coherent wave signal in the phase-averaging process due to the small magnitude of the wave oscillations relative to the magnitude of the background turbulence fluctuations.

In order to perform phase-averaging of the velocity signals, the voltage signal produced by the function generator was recorded simultaneously with the hot wire measurements. The excitation frequency f_e of the voltage signal acted as the reference signal for the phase-averaging process. The phase angle ϕ was determined at each time using

$$\phi(t) = 2\pi f_e \left(t \; mod \; \frac{1}{f_e} \right) + \phi_0 \tag{2.13}$$

where t = 0 denoted the time at which measurements began being taken and ϕ_0 was initial phase of the voltage signal.

After obtaining the phase angle at each time, the velocity measurements were binned such that all velocities corresponding to a small range of phase angles were averaged. The number of bins and the time period required to extract a coherent wave from the signal were highly dependent on the strength of the signal. Up to 30 minutes of velocity measurements were necessary in order to extract a coherent wave signal for low amplitude forcing. Experimental noise was still apparent in the data after undergoing phase-averaging. As a result, all phase-averaged terms underwent a sinusoidal fit for the purposes of visualization and to better estimate the amplitude and phase offset of each wave.

2.4 Piezoelectric Actuator

Bimorph piezoelectric actuators (as seen in Fig. 2.6) were created at the University of Maryland (College Park) to serve as the excitation source for the turbulent jet. An aluminum wedge was used as the base of the actuator with a length of 69 mm, a width of 15 mm, and a tapered thickness from 8.3 to 0.25 mm. Four centimeters of constant thickness aluminum on one end of the wedge allowed the actuator to be clamped at the beginning of the taper.

Two 260 μm thick sheet of PZT-5H2 with nickel electrodes of 1 μm thickness were used to actuate each wedge. The actuator area was defined photolithographically on the PZT sheet using an IKONICS RapidMask dry film photoresist. As specified by

Misri et al. [49], micropowerblasting was performed in which the PZT sheet was subjected to a pressurized mixture of air and 25 μm alumina particles through a specialized nozzle. Conductive epoxy was then used to bond the PZT sheets to both sides of the wedge. The PZT sheets were polarized with respect to thickness by the manufacturer and were operated in the d_{31} mode.

Figure 2.6: Image of a bimorph piezoelectric actuator.

The actuator was excited using a white noise spectrum and the resonant frequencies were measured using a scanning laser Doppler vibrometer [50]. Multiple actuators were used throughout the course of the experiment, each with a second resonant frequency of approximately 5.3 kHz. The actuator tip velocity was measured by actuating using a sine wave at the desired modal frequency. The laser vibrometer was capable of measuring the actuator tip velocity up to a maximum of 1 m/s. Excitation of the actuator at the second resonant frequency with a peak-to-peak voltage of 200 V was confirmed to result in a tip velocity larger than 1 m/s.

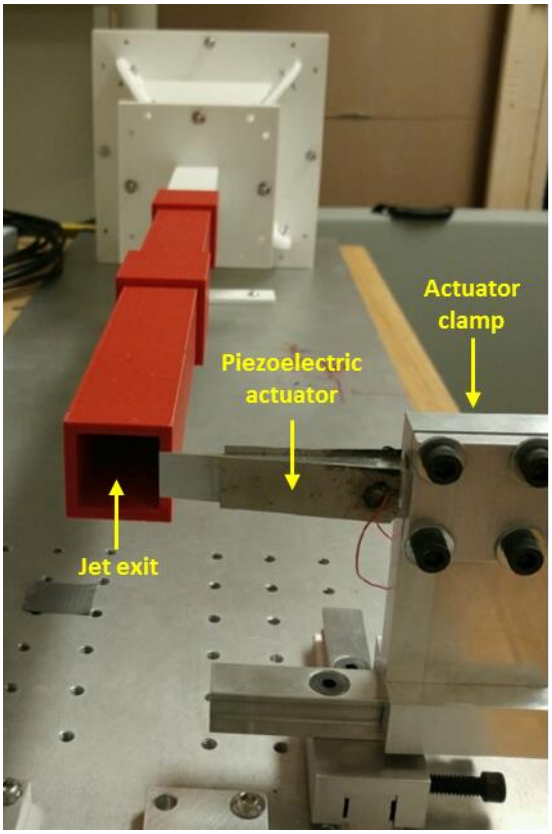

Figure 2.7: Image of the actuator position during measurements.

The actuator was cantilevered with a variable position clamp mechanism which was attached to an aluminum plate that was also used to mount the turbulent jet. The natural frequency of the clamp was approximately 7 kHz, ensuring that the actuator could be operated in its second resonant mode without interference from the cantilever. As seen in Fig. 2.7, the tip of the actuator was positioned 1 mm downstream of the jet exit and aligned flush with the inner surface of the square duct such that the vertical midpoint of the actuator tip was located at the vertical midpoint of the jet exit. This orientation ensured that the bulk flow quantities were not impacted while the actuator was not activated.

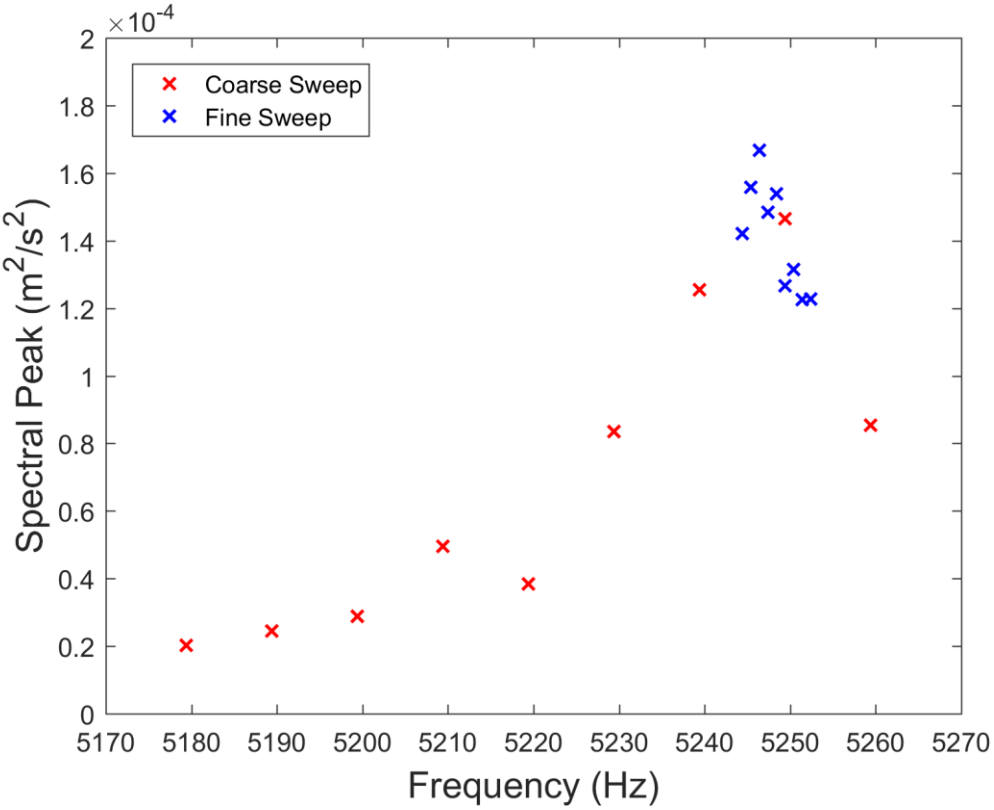

Figure 2.8: Coarse and fine frequency sweeps of the spectral peak.

The second resonant frequency was verified before each use in order to maintain optimal tip velocity. Resonant frequency verification was carried out by setting the actuator to the low voltage mode and measuring the spectral peak of the jet velocity power spectra using a single-wire probe before each use. The jet was set on during these experiments to determine the maximum turbulent sub-structure generation in the flow, which was assumed to correspond with the maximum actuator tip velocity. The probe was placed on the jet centerline at x/D_H = 1.0 and the jet was set to a mean velocity of 6.5 m/s. A coarse frequency sweep with 10 Hz steps was followed by a fine frequency sweep with 1 Hz steps before each experiment. The operating frequency with

the highest spectral peak was chosen as the excitation frequency. A plot of a coarse and fine frequency sweep is shown in Fig. 2.8.

A BK Precision 4014B function generator was used in conjunction with a Trek high-voltage power amplifier to drive the actuator at its second resonant frequency. The input voltage signal of the actuator was chosen such that the actuator could be operated at its second resonant frequency for extended periods of time with maximal tip velocity. In this case, an AC voltage signal was applied with a DC offset to set the maximum and minimum voltages to the limitations of the PZT material. The maximum electric field applied to piezoelectric cantilevers is limited at negative voltages by depolarization and at positive voltages by arcing (electric discharge across the PZT due to microcracks formed during the manufacturing process) and dielectric breakdown, all of which can significantly reduce the tip velocity of an actuator [51]. The limiting electric fields for PZT-5H2 were reported to be -4.72 kV/cm and +14.15 kV/cm due to depolarization and dielectric breakdown, respectively. These electric field strengths corresponded to voltages of -122 V and 367 V for 260 μm thick piezoelectric sheets, which were the type used in the actuator in this study. However, these findings were obtained experimentally for the operation of a piezoelectric actuator at 40 Hz. Because dielectric breakdown occurs after an actuator has accumulated many cycles, at high frequency and voltage, the peak voltage an actuator can withstand is reduced. Experiments were conducted on the actuators in the current study to determine the effective operating range of the actuators.

The actuator was characterized over a range of input voltage signals to determine the positive voltage at which dielectric breakdown occurs. For each test, the

actuator was run for 30 minutes with a sinusoidal input voltage ranging from 0 V to the maximum voltage. Depolarization was neglected by limiting the signal to positive voltages. The tests were run in succession on the same actuator with a minimum voltage of 0 V and a maximum voltage varying from 50 V (1.92 kV/cm) from 200 V (7.69 kV/cm). The turbulent jet was operated with a mean velocity of 6.5 m/s and the streamwise velocity at x/D_H = 1.0 was recorded for 60 seconds every three minutes using the single-wire probe. The spectral peak of the velocity power spectrum was determined at each time to detect when dielectric breakdown occurs.

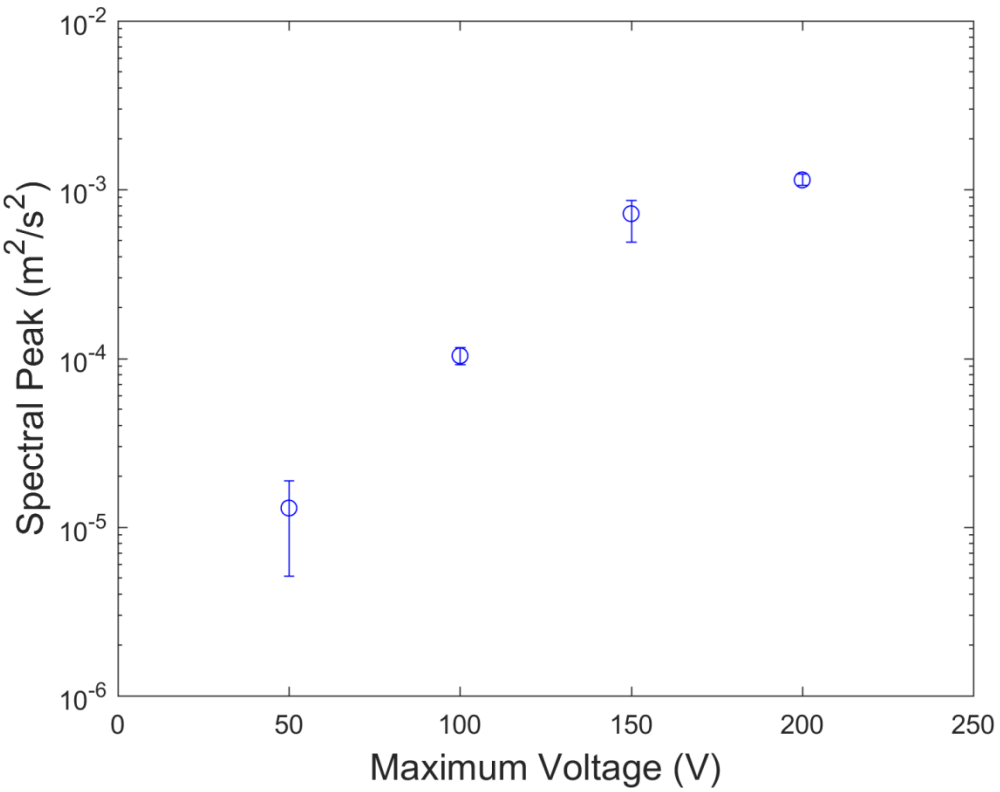

Figure 2.9: Magnitude of spectral peak versus maximum voltage for a minimum voltage of 0 V.

As shown in Fig. 2.9, the average spectral peak increased with maximum voltage and was highest when the actuator was operated at a maximum voltage of 200

V. The error bars indicate the variation in the spectral peak during the full 30 minutes of operation. There was an order of magnitude reduction in the spectral peak after 24 minutes of operation for 200 V maximum voltage, indicating the onset of dielectric breakdown. Measurements after dielectric breakdown were not included in the average of the spectral peak shown in Fig. 2.9.

A follow-up experiment was performed to determine the life of the actuator for operation with an input voltage signal with a maximum voltage of 200 V and a minimum voltage of 0 V without successively increasing the magnitude as was done in prior tests. This experiment showed that the actuator was capable of more than 180 minutes of operation (corresponding to 57,240,000 cycles) for this input voltage signal without onset of dielectric breakdown. However, it should be noted that the average spectral peak was approximately 35% lower for this test, suggesting that the actuator had a lower tip velocity than the actuator used for the previous dielectric breakdown characterization. While the actuators in this study have been observed to have significant variation under similar operating conditions, the actuators themselves were not the focus of the study and were used primarily because of their simplicity in actuating a free turbulent jet flow.

Including a negative bias voltage in the input voltage signal can increase the actuator tip velocity, but also causes the PZT to gradually degrade over time [52]. Depolarization of a PZT sheet can be reversed by applying a positive DC voltage to the sheet, but the tip velocity of a repolarized actuator is reduced relative to its initial magnitude. The voltage at which the actuator initially depoles decreases in magnitude as the excitation frequency increases, limiting potential increases in the actuator tip

velocity by introducing a negative bias to the input voltage signal in the context of high frequency excitation. A series of input voltage signals were tested with the maximum voltage set to 50 V and the minimum voltage was gradually decreased from 0 to -50 V. Similar to the dielectric breakdown characterization, the jet was operated with a mean velocity of 6.5 m/s and the velocity signal at x/D_H = 1.0 was recorded for 60 seconds for each voltage signal tested. As shown in Fig. 2.10, the spectral peak increases linearly as the magnitude of the negative bias increases up to a minimum voltage of -40 V. The spectral peak for a voltage signal with a minimum voltage of -50 V has a lower spectral peak than a minimum voltage of -40 V, indicating that the actuator began to depolarize between -40 (-1.54 kV/cm) and -50 (-1.92 kV/cm).

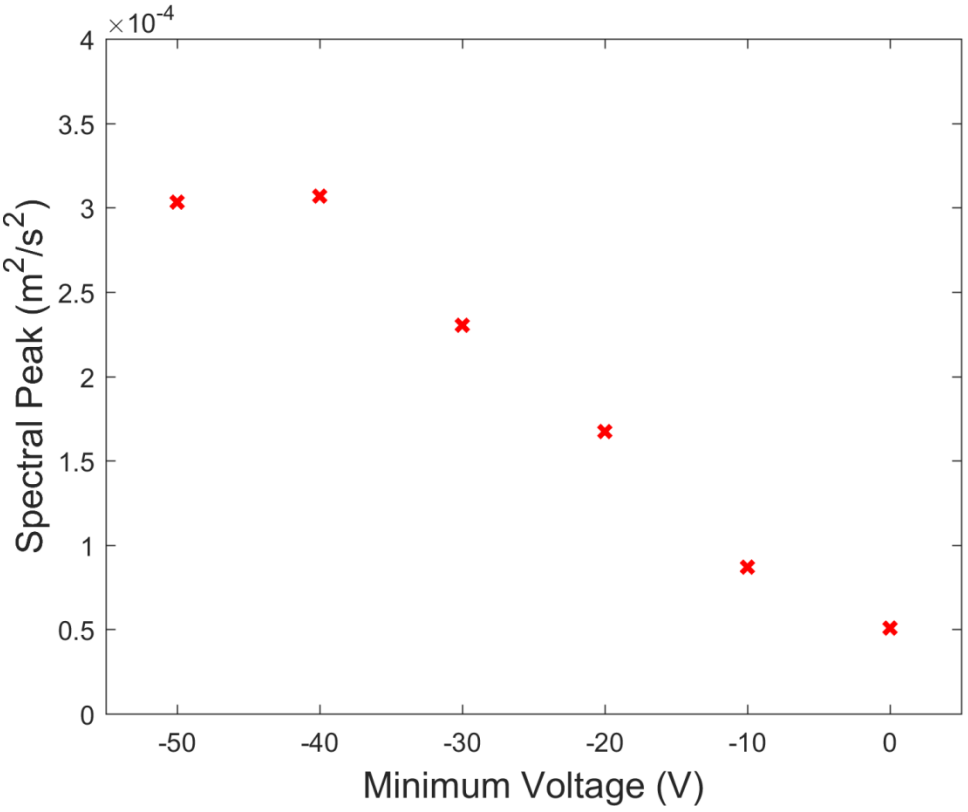

Figure 2.10: Magnitude of spectral peak versus minimum voltage for a maximum voltage of 50 V.

Two input voltage signals (shown in Fig. 2.11) were ultimately chosen for actuator operation throughout this study. The first signal was a high amplitude wave with a maximum voltage of 200 V and a minimum voltage of -40 V. This signal was intended to maximize the generation of turbulent kinetic energy by operating at the previously tested limits of dielectric breakdown and depolarization. It was assumed that this voltage signal also maximized the tip velocity of the actuator. The second signal was a low amplitude wave with a maximum voltage of 150 V and a minimum voltage of -30 V. This signal was used for tests which required the actuator to be operated for longer periods of time without significantly reducing the amount of turbulent kinetic energy added to the flow.

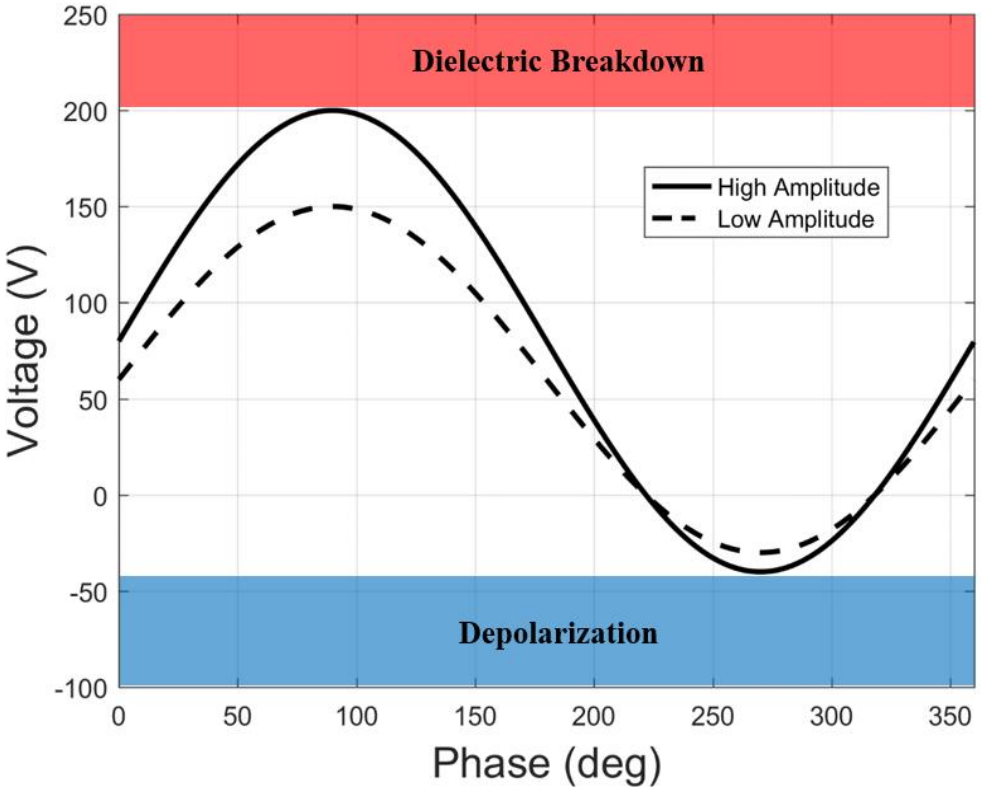

Figure 2.11: Input voltage signals as a function of phase at 5.3 kHz.

For each experiment, the spectral peak in the middle of the jet at $x/D_H = 1.0$ was tested before and after taking measurements. These tests verified that neither dielectric breakdown nor depolarization reduced the actuator tip during the course of the measurements over the measurement domain. Dielectric breakdown was the primary limiting factor of the actuators, and the actuator was replaced after this occurred.

Chapter 3 – Results

Past numerical results [44] have suggested that transitional flow may be more susceptible to high frequency excitation than fully turbulent flow. To investigate this phenomenon, a spatially evolving flow was analyzed at different stages of turbulent development with and without excitation over the full measurement domain using the single-wire probe. The first condition was termed undeveloped turbulent flow, (U_0 = 6.34 m/s) with no flow elongators attached to the jet exit, resulting in a square duct development length of $6D_H$. The second condition was termed developed turbulent flow, (U_0 = 6.33 m/s) with two flow elongators attached to the end of the jet, which yielded a longer development length ($20D_H$) and increased the turbulence intensity at the jet exit (from 0.016 to 0.040). The flows were characterized first for the unforced baseline flow and then for the forced flow with the actuator operated at high amplitude. Bulk flow quantities and velocity power spectra were analyzed to determine the effects of high frequency excitation.

After completing the analysis of the undeveloped and developed flow, the developed flow condition was chosen for further examination. A sweep of mean velocities for the forced flow was completed in order to find the velocity at which the spectral peak was maximized. Afterward, measurements were taken for the jet with two flow elongators and reduced mean velocity (U_0 = 4.80 m/s). Single-wire measurements of the forced flow with the actuator operating in the low amplitude mode were obtained and compared to unforced results. Dual-wire probe measurements of the unforced flow were then taken to approximate the eddy viscosity using the Boussinesq approximation. The Reynolds & Hussain [13] nonlinear closure term $\tilde{r}_{12}$ was measured experimentally

for both low and high amplitude forcing. The experimental measurements were compared to the linear model in Eq. 1.9 which was generated with the eddy viscosity from the Boussinesq approximation. The results presented here are the first experimental measurements of the Reynolds & Hussain [13] closure term under direct excitation of small scale turbulence.

3.1 Baseline Flows

Unforced flow measurements were taken for the undeveloped and developed flows to serve as a baseline for comparison with forced flow quantities. As shown in Fig. 3.1, the measurement domain encompassed one of the turbulent shear layers from the jet centerline to the outer edge of the jet expansion at the farthest streamwise location. Velocity measurements on for the shear layer opposite the side of the piezoelectric actuator were not recorded for either flow condition.

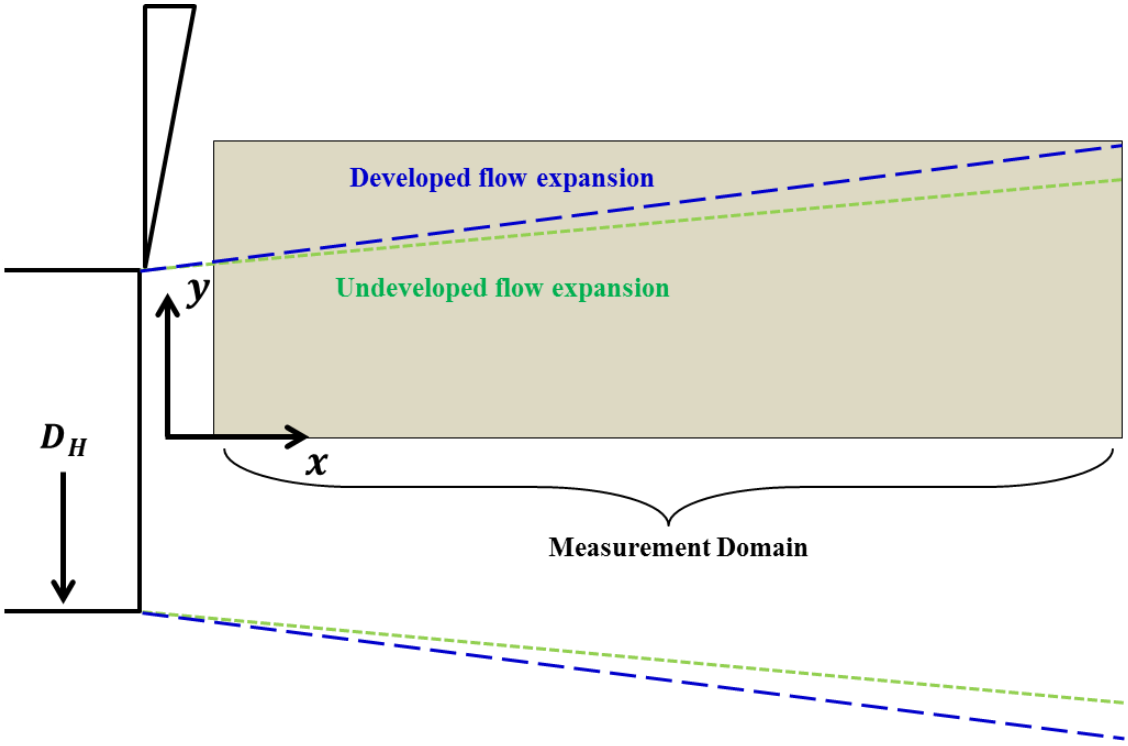

Figure 3.1: Diagram of the undeveloped and developed flow expansion.

It should be noted that all unforced measurements were taken with the actuator located in the same position as for the forced measurements, but no voltage was applied to the actuator. Due to the positioning of the actuator tip at the edge of the shear layer no appreciable differences were observed between the unforced flow with and without the unpowered actuator. Bulk flow quantities were calculated using single-wire probe measurements at each measurement location.

3.1.1 Near-Exit Measurements

Additional attention was given to the bulk flow quantities near the exit due to the fact that the undeveloped flow became more turbulent with increasing downstream distance. As a result, the differences between the undeveloped and developed flows were highlighted at the closest measurement location to the jet exit.

The mean velocity profiles at x/D_H = 0.25 for each flow condition are plotted in Fig. 3.2. Data at spanwise locations greater than y/D_H = 0.50 (farther than the inner edge of the jet exit boundary) are not shown because the mean velocities at these points were near zero close to the jet exit. The undeveloped flow had a mean velocity U_0 of 6.34 m/s at the jet exit and a Reynolds number of 8,700 based on the hydraulic diameter of the jet (D_H = 2.54 cm). The undeveloped flow mean velocity was fairly constant between the jet centerline and y/D_H = 0.30, after which there was a sharp drop-off. This top-hat shaped profile was expected for flow which was transitioning from laminar to turbulent [47]. The developed flow mean velocity was 6.33 m/s (Re = 8,700), and the mean velocity decreased from the centerline to the jet exit relatively gradually with

respect to the undeveloped flow. This profile resembled the Gaussian shape which was expected for fully turbulent flow.

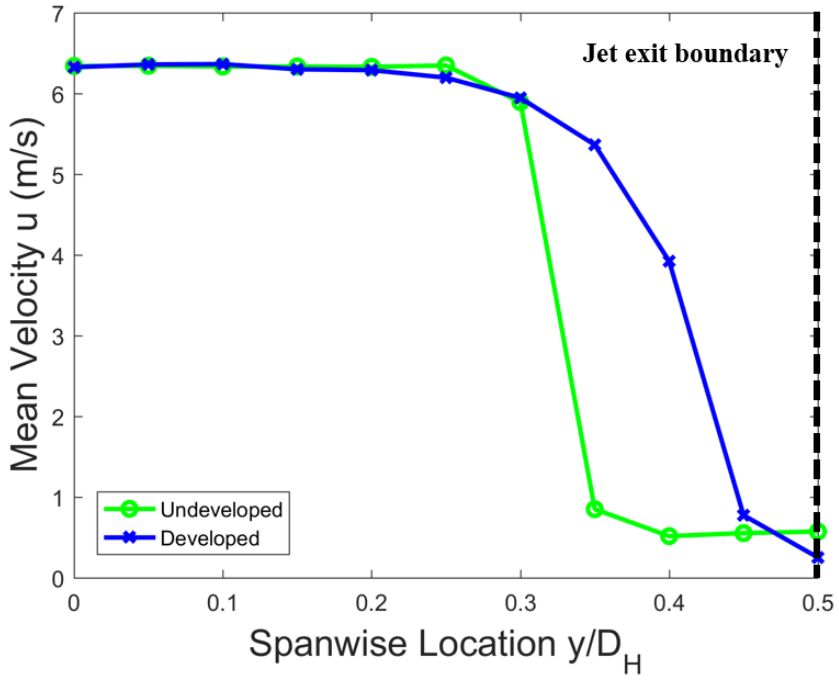

Figure 3.2: Mean velocity profiles at x/D_H = 0.25.

The root mean square (RMS) velocity fluctuation u' at each spanwise measurement location at x/D_H = 0.25 is plotted in Fig. 3.3. For the undeveloped flow, the turbulence intensity (u'/U_0) on the centerline of the jet exit was 1.6%. The magnitude of the RMS velocity fluctuation reached a peak of $0.11U_0$ at y/D_H = 0.30, which coincided with the spanwise position just before the sharp drop-off in the mean velocity. The developed flow case had a turbulence intensity of 4.0% at the jet exit on the centerline, and the peak RMS velocity fluctuation was $0.19U_0$ at y/D_H = 0.40. The magnitude of the velocity fluctuation for the developed flow was larger than the undeveloped flow at all spanwise locations except y/D_H = 0.30.

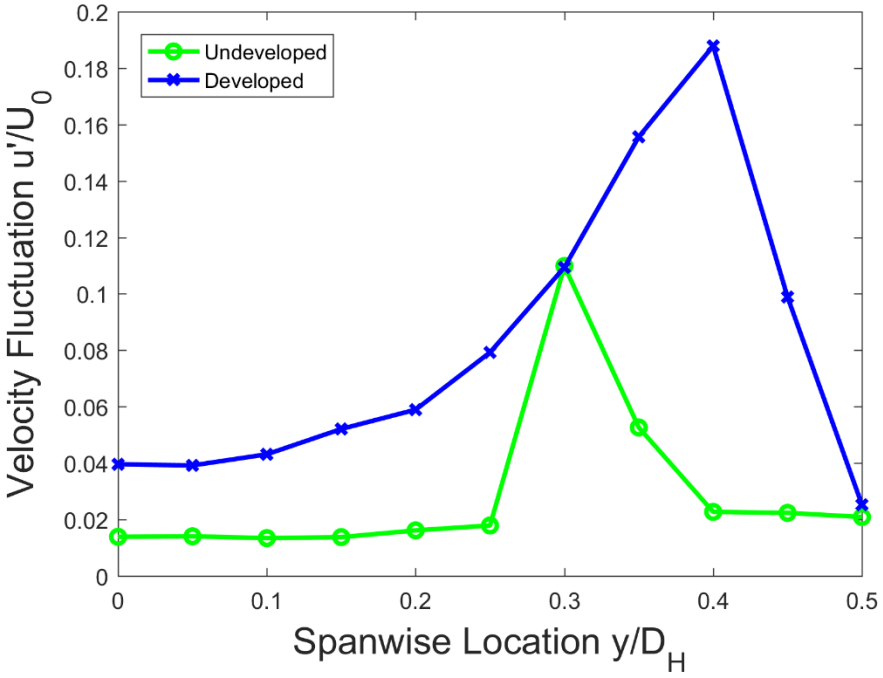

Figure 3.3: Spanwise distribution of RMS velocity fluctuation at x/D_H = 0.25.

The energy dissipation rate ε was approximated using Taylor's hypothesis as demonstrated in Eq. 2.8. The spanwise variation in energy dissipation rate at x/D_H = 0.25 is shown in Fig. 3.4. Transitional flow energy dissipation rate was 44 m^2/s^3 at jet centerline and 572 m^2/s^3 at y/D_H = 0.35. The developed flow energy dissipation rate had a minimum of 18 m^2/s^3 at the jet centerline and a maximum of 320 m^2/s^3 at y/D_H = 0.45. The undeveloped flow energy dissipation rate was larger than the developed flow energy dissipation rate at all spanwise locations within the high mean velocity region of the flow (i.e. prior to the sharp decrease in the mean velocity profile). For both the undeveloped and developed flow, the peak in energy dissipation rate coincided with the spanwise position after this large drop-off in the mean velocity, signifying that dissipation was highest in locations where low velocity

fluid was entrained into the flow. This was expected due to the fact that Taylor's hypothesis for the energy dissipation rate is inversely related to the mean velocity.

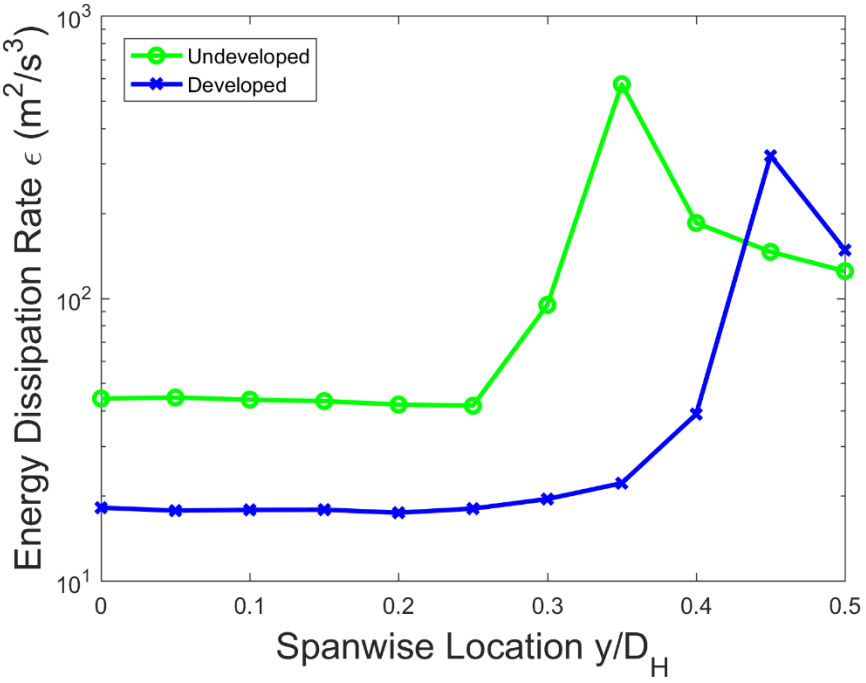

Figure 3.4: Spanwise distribution of energy dissipation rate at x/D_H = 0.25.

The Kolmogorov scale η was calculated at each measurement location near the jet exit using Eq. 1.11. A plot of the Kolmogorov scale structure size for spanwise locations at x/D_H = 0.25 are shown in Fig. 3.5. The Kolmogorov scale is inversely related to the energy dissipation rate, and as a result the Kolmogorov scale structures were smallest at the locations of maximum ε. The undeveloped flow Kolmogorov scale ranged from 0.057 mm to 0.109 mm, and the developed flow Kolmogorov scale ranged from 0.066 mm to 0.136 mm.

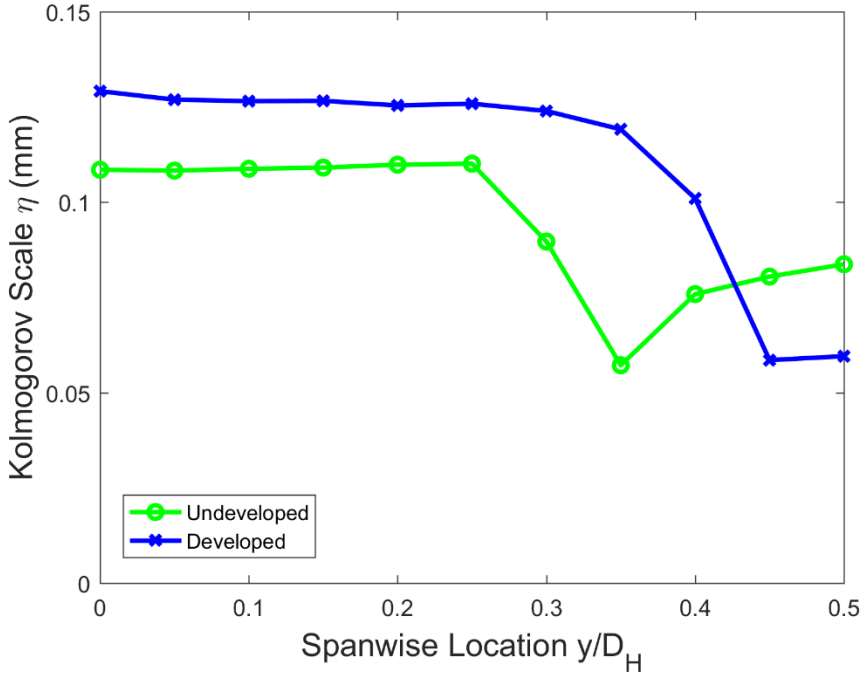

Figure 3.5: Spanwise distribution of Kolmogorov scale at x/D_H = 0.25.

The passage frequency corresponding to the Kolmogorov scale structure size is shown in Fig. 3.6. The maximum passage frequency at x/D_H = 0.25 was 32.8 kHz for the undeveloped flow and 23.3 kHz for the developed flow. The spanwise location of the actuator tip was y/D_H = 0.50, where the Kolmogorov passage frequencies were 3.4 kHz and 1.6 kHz for the undeveloped and developed flows, respectively. For each case, the excitation frequency of the actuator (5.3 kHz) was less than the Kolmogorov passage frequency at the jet centerline but greater than the Kolmogorov passage frequency at the location of the actuator tip. However, Wiltse & Glezer [11] indicated that the passage frequency on the centerline was a better indication of the relative location of the Kolmogorov scale frequency at each spanwise location. This observation was supported by the velocity power spectra presented in the following

sections, for which the unforced and forced spectra each extend past the forcing frequency.

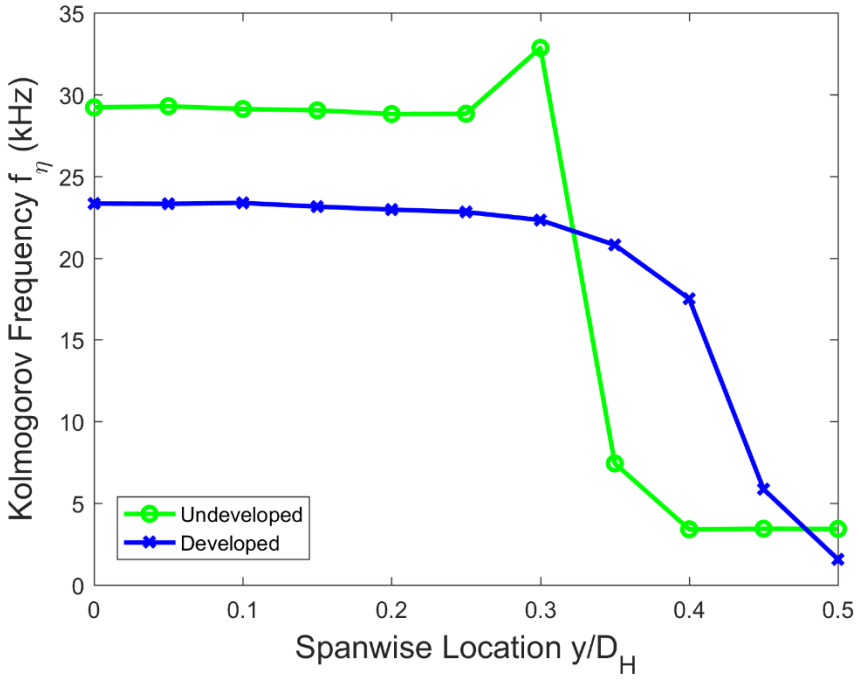

Figure 3.6: Spanwise distribution of Kolmogorov frequency at x/D_H = 0.25.

3.1.2 Full Domain Measurements

Contours of the mean velocity for each flow obtained with the single-wire probe are shown in Fig. 3.7. The undeveloped flow in Fig. 3.7(a) exhibited the beginning of a potential core (a cone-shaped region of constant mean velocity emanating from the jet exit) which was anticipated for undeveloped turbulent flow [47]. The spread rate of the undeveloped flow was less than that of the developed flow (Fig. 3.7(b)), resulting in lower mean velocity at farther spanwise locations as the flow moved downstream. This was exemplified at x/D_H = 2.50, where the mean velocity decreases to half of the

centerline value at y/D_H = 0.35 for the undeveloped flow and y/D_H = 0.50 for the developed flow.

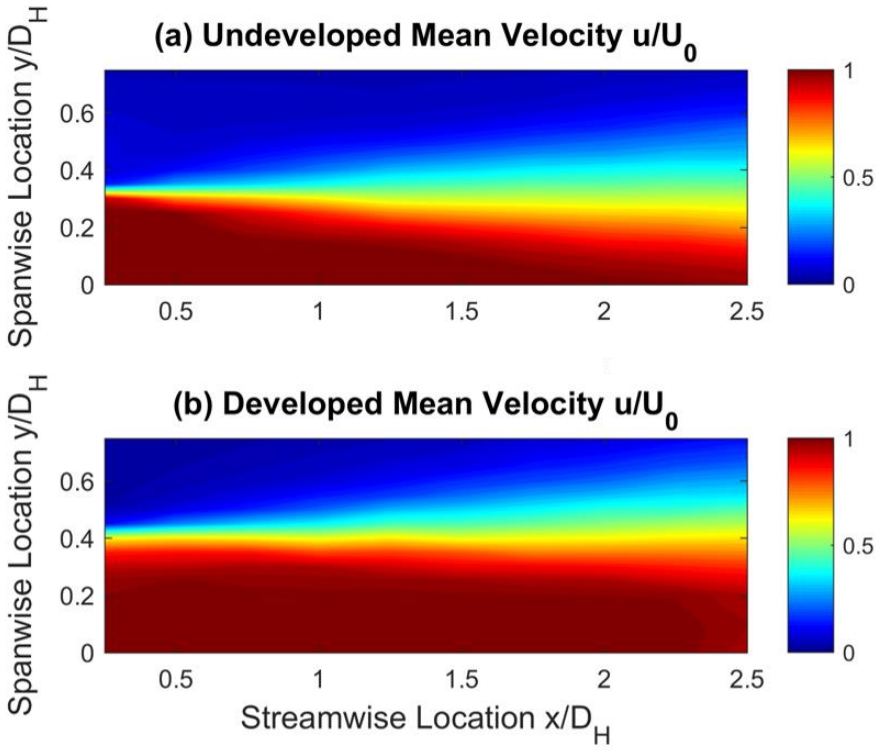

Figure 3.7: Mean velocity contour for (a) undeveloped and (b) developed flows.

The RMS velocity fluctuation contours in Fig. 3.8 highlight the expansion of the shear layer of each flow they moved downstream. In general, each flow condition had low velocity fluctuation along the jet centerline which gradually increased as the spanwise mean velocity decreased. The spanwise location with peak velocity fluctuation stayed relatively constant for both undeveloped and developed flow experiments. For the undeveloped flow in Fig. 3.8(a), this peak velocity fluctuation increased between x/D_H = 0.25 and x/D_H = 0.75, indicating that the undeveloped flow became more developed within this region. This phenomenon did not occur for the

developed flow (Fig. 3.8(b)). The general trend of each of the flow conditions was for the velocity fluctuation to gradually decrease as the flows moved downstream.

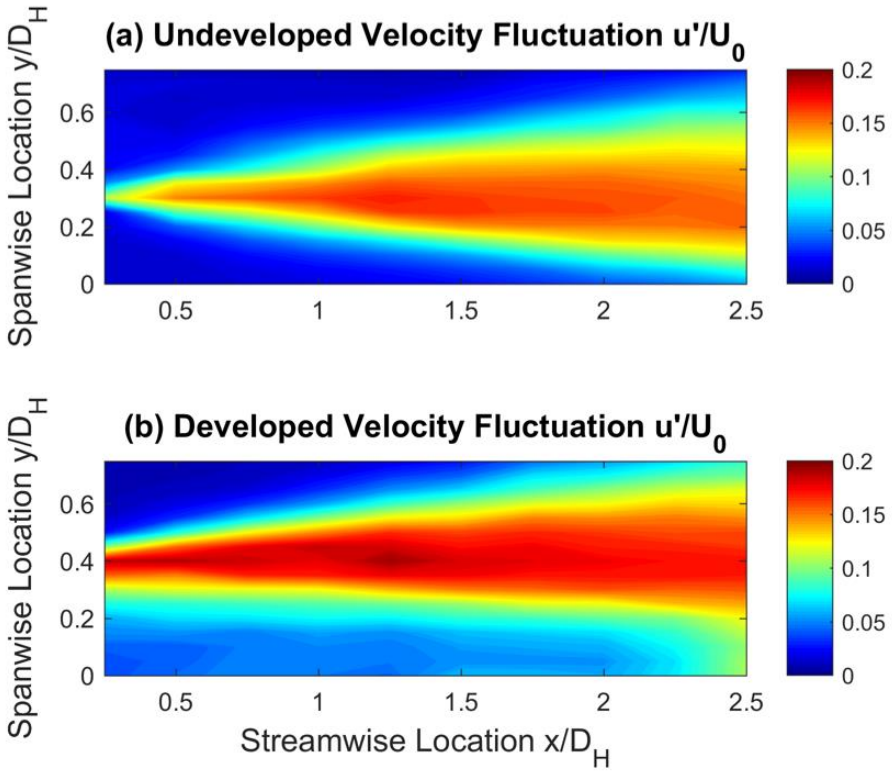

Figure 3.8: Velocity fluctuation contours for (a) undeveloped and (b) developed flows.

Energy dissipation rate contours for the two cases are seen in Fig. 3.9. The energy dissipation rate was higher for the undeveloped flow than the developed flow for all measurement locations close to the jet exit. The regions of high energy dissipation roughly followed the outer (high y) edges shear layers which can be seen in the velocity fluctuation contours in Fig. 3.8. Energy dissipation rate decreased with downstream distance more rapidly than the velocity fluctuation. The spanwise peak in energy dissipation rate was 82% higher closest the jet exit compared to measurements at the farthest downstream location for the undeveloped flow. For the developed flow,

the decrease in maximum streamwise energy dissipation was 72%. The energy dissipation rate was clearly larger for the undeveloped flow than the developed flow close to the jet exit at x/D_H = 0.25, with a percent difference of 56% for the maximum spanwise value. The percent difference in peak energy dissipation rate dropped to 8% farthest downstream, which was attributed to the undeveloped flow becoming more developed with increasing downstream distance.

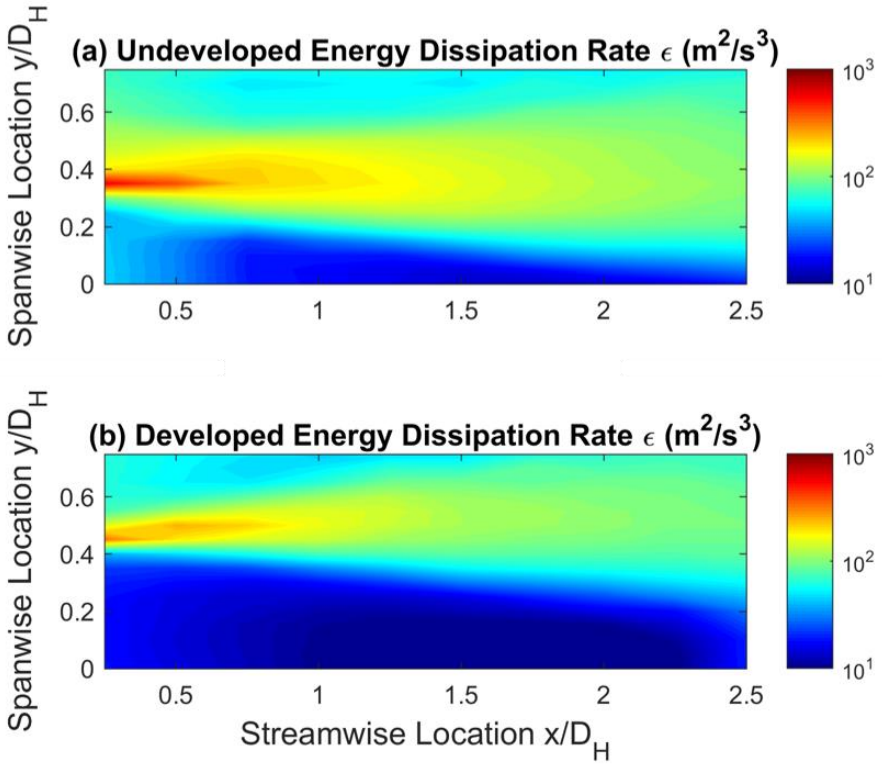

Figure 3.9: Energy dissipation contours for (a) undeveloped and (b) developed flows.

3.2 Forced Flow

Each flow condition was subjected to high frequency excitation using a single piezoelectric actuator operating in its high amplitude mode and excited at its second resonant frequency of 5320 Hz. The same actuator was used for the undeveloped flow

forcing and the developed flow forcing in order to maintain consistency between the two experiments. This excitation frequency corresponded to a characteristic length scale l of 0.60 mm which was calculated from Eq. 2.9. The characteristic length scale was expected to be the size of the vortices which the actuator injected into the flow at the jet exit. The Strouhal number (calculated from Eq. 1.1 based on the hydraulic diameter of the jet) of the undeveloped flow was 21.3. For each flow condition, forced measurements were obtained in succession with unforced measurements to minimize differences to due small changes in ambient conditions in the laboratory.

3.2.1 Near-Exit Excitation

The effects of excitation were most apparent for each flow closest to the jet exit. Hence, forced and unforced quantities at x/D_H = 0.25 were analyzed individually in order to emphasize the forcing effects near the tip of the actuator.

Mean velocity profiles of the unforced and forced flows for each case are shown in Fig. 3.10. Data outside of the jet wall boundary (y/D_H = 0.25) due to near zero mean velocities at those locations. For undeveloped flow seen in Fig. 3.10(a), the forced flow distribution was smoother than the unforced distribution near the jet exit, with the initial decrease in mean velocity occurring closer to the jet centerline. The forced flow mean velocity at y/D_H = 0.25 was $0.97U_0$ while the unforced flow was $1.00U_0$ at this location, which was a larger difference than the expected error due to voltage fluctuation of the hot wire anemometer ($0.01U_0$). For the developed flow in Fig. 3.10(b), the forced mean velocity profile was slightly increased relative to the unforced mean velocity profile at all spanwise locations, and this increase was larger

than the expected error of the anemometer. Despite slight differences in the forced mean velocity profiles near the jet exit, the general shapes of each distribution remained the same. Stanek et al. [42] theorized that high frequency excitation had a stabilizing effect on turbulent flow, resulting in mean velocity distributions which decreased to zero more gradually with increasing spanwise distance. However, this effect was not observed in either flow, and in fact the most apparent mean velocity differences occurred in regions of high velocity, with the low velocity regions remaining unaffected.

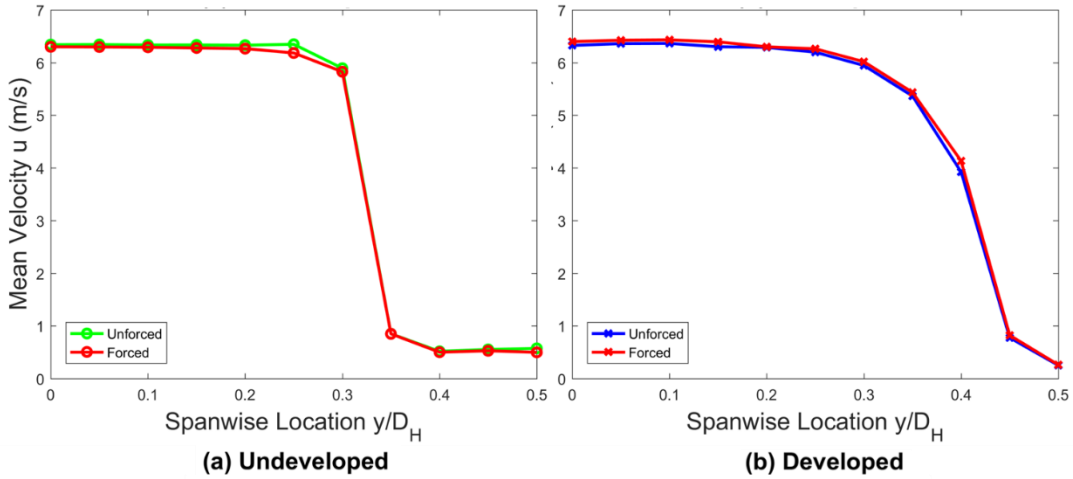

Figure 3.10: Forced and unforced mean velocity profiles at x/D_H = 0.25 for the (a) undeveloped (b) and developed flows.

The forced and unforced velocity fluctuation distributions for each flow are shown in Fig. 3.11 at x/D_H = 0.25. At the centerline, the forced turbulence intensity was unchanged relative to the unforced flow in each case. The unforced velocity fluctuation in the undeveloped flow had a sharp increase to its maximum at y/D_H = 0.30 as seen in Fig. 3.11(a), while the forced flow velocity fluctuation

increased up to its maximum value more gradually. Additionally, the maximum forced velocity fluctuation of $0.12U_0$ was larger than the unforced maximum of $0.11U_0$ for undeveloped flow. These increases appear to demonstrate that the forcing caused the undeveloped flow to become more turbulent at the jet exit. Unlike the undeveloped flow, no clear trend emerged in the velocity fluctuation distributions of the developed flow in Fig. 3.11(b). While forcing appeared to cause the undeveloped velocity fluctuation distribution to appear more turbulent, the appearance of the unforced developed velocity fluctuation distribution appeared turbulent before forcing was applied.

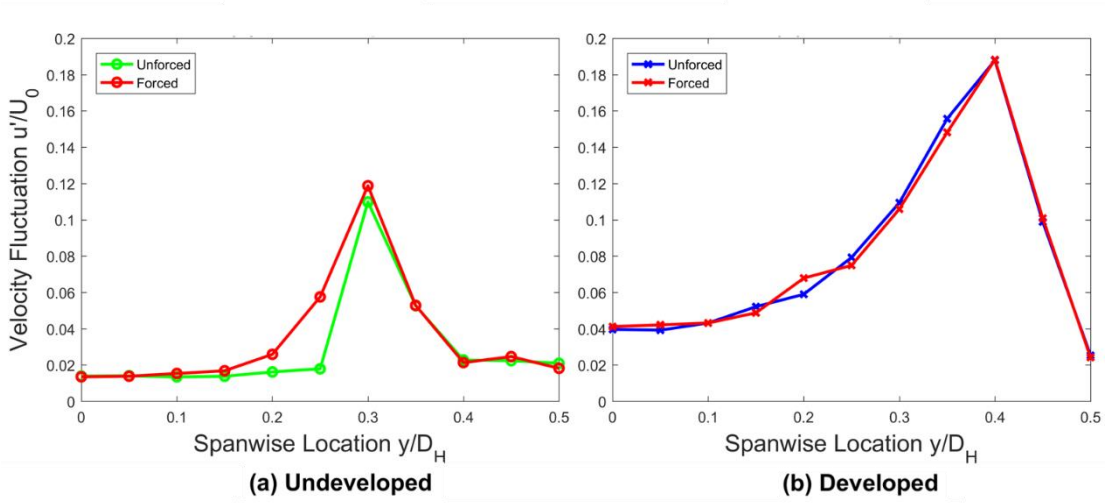

Figure 3.11: Forced and unforced spanwise distributions of velocity fluctuation at x/D_H = 0.25 for the (a) undeveloped and (b) developed flows.

Spanwise variation in forced and unforced energy dissipation rate at x/D_H = 0.25 is plotted in Fig. 3.12 for each flow condition. The undeveloped flow showed no appreciable effects of forcing near the jet centerline in Fig. 3.12(a). However, at the peak at y/D_H = 0.35, the forced flow energy dissipation rate was 875

m^2/s^3 versus 572 m^2/s^3 for the unforced flow—a 53% increase. The undeveloped energy dissipation rate in the forced flow remained larger than the unforced flow outside of this peak, corresponding to the low velocity region of the undeveloped profile. The developed energy dissipation rate, on the other hand, showed appreciable effects of forcing at each spanwise location as seen in Fig. 3.12(b). The forced flow energy dissipation rate was higher than the unforced flow at all spanwise locations near the exit, and the maximum forced energy dissipation rate at y/D_H = 0.45 was increased to 522 m^2/s^3, 63% larger than the unforced maximum. The general shape forced distribution for the undeveloped flow was similar except at y/D_H = 0.50, where the unforced energy dissipation rate sharply decreased but the forced energy dissipation rate remained large.

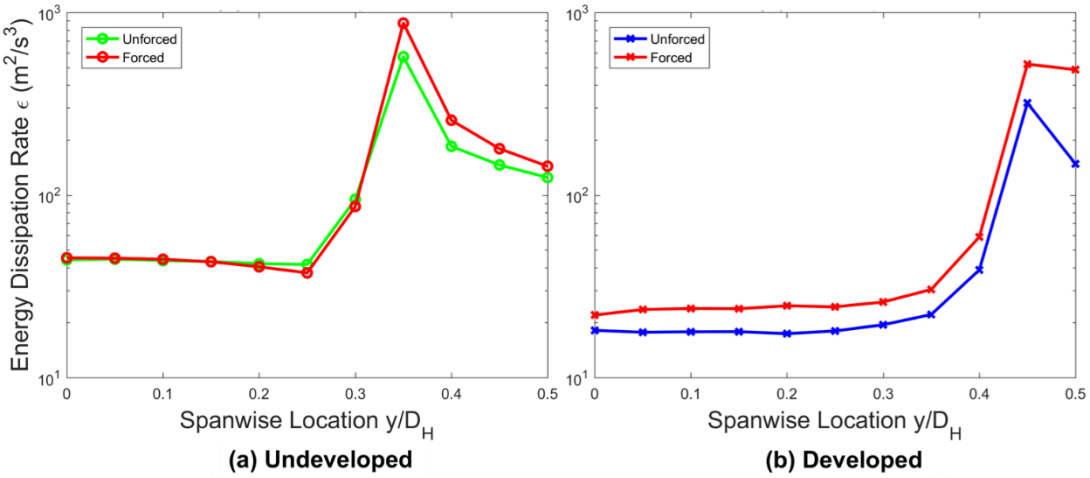

Figure 3.12: Forced and unforced spanwise distributions of energy dissipation rate at x/D_H = 0.25 for the (a) undeveloped and (b) developed flows.

It should be noted that Wiltse & Glezer [11] found that the energy dissipation rate was highly impacted by the introduction of high frequency excitation to the flow.

Similar to the results presented in the developed flow distributions above, the energy dissipation rate was increased at all spanwise locations, but the largest increases appeared at the farthest spanwise locations. However, the forced energy dissipation rates observed by Wiltse & Glezer were increased by more than an order of magnitude near the actuator tip. The increased energy dissipation rates in both forced flows shown here were small by comparison.

As a result of differences in the energy dissipation rate, the Kolmogorov scale at x/D_H = 0.25 (shown in Fig. 3.13) was also altered due to forcing. As expected due to the inverse correlation between energy dissipation rate and Kolmogorov scale, the most notable effects on the Kolmogorov scale at each location corresponded to the locations in which the energy dissipation rate was increased. In the undeveloped flow, the Kolmogorov scale was 0.051 mm at the peak energy dissipation rate location, which was 11% smaller than the unforced Kolmogorov scale of 0.057 mm. Increased energy dissipation rate at all spanwise locations in the developed flow coincided with reduced size Kolmogorov scale structures at these locations, as is demonstrated in Fig. 3.13. The smallest Kolmogorov scale size was 0.059 mm at y/D_H = 0.45, which was 12.5% smaller than that of the unforced flow.

Extending the idea that the Kolmogorov scale at the jet centerline is the determinant of the Kolmogorov passage frequency, the new developed passage frequency of Kolmogorov scale structures at the jet exit was 24.7 kHz (from 23.3 kHz in the unforced case). The substantial effects of high frequency excitation on the energy dissipation rate observed by Wiltse & Glezer [11] also nearly doubled the forced Kolmogorov passage frequency, effectively moving the end of the dissipative subrange

to a much higher frequency. In the case of each forced flow examined in this study, this considerable extension of the turbulent kinetic energy spectrum toward higher frequencies was not observed.

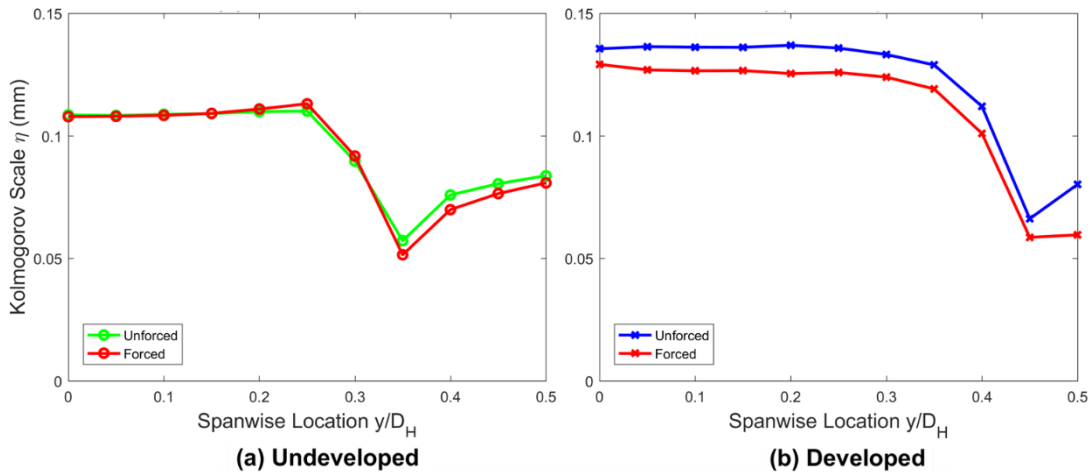

Figure 3.13: Forced and unforced spanwise distributions of the Kolmogorov scale for the (a) undeveloped and (b) developed flows at x/D_H = 0.25.

3.2.2 Full Domain Excitation

The effects of excitation on the bulk flow quantities over the full measurement domain were analyzed by comparing contours of the unforced and forced flows for each flow condition. The mean velocity contours of the undeveloped flow are shown in Fig. 3.14. The forced flow demonstrated notably increased spreading from $0.50 \leq x/D_H \leq 1.0$, which was indicative of the mean velocity of more turbulent flow. Differences between the unforced and forced flows were indistinguishable outwards of x/D_H = 1.0. In contrast with the contours of the developed flow (Fig. 3.15), the forced mean velocity was not appreciably different than the unforced mean velocity, and this increased spread rate close to the jet exit was not observed.

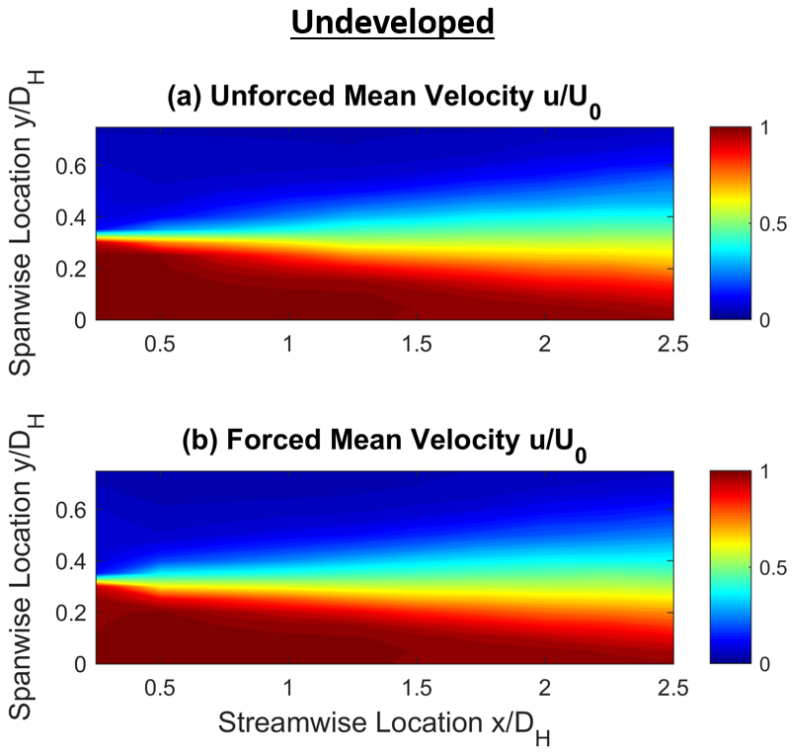

Figure 3.14: Mean velocity contours of (a) unforced and (b) forced undeveloped flow.

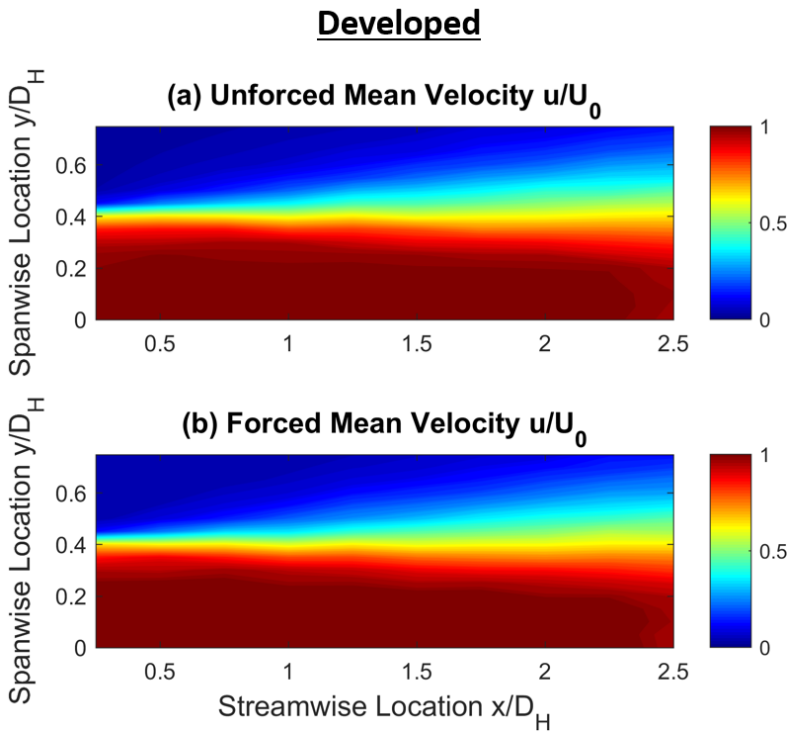

Figure 3.15: Mean velocity contours of (a) unforced and (b) forced developed flow.

Contours of the unforced and forced velocity fluctuation are shown in Fig. 3.16 for the undeveloped flow. Spreading of the peak velocity fluctuation was visible within the shear layer for $x/D_H \leq 1.0$. This region of high velocity fluctuation, associated with high shear region of the flow, expanded more rapidly with added forcing. Outwards of x/D_H = 1.0, the velocity fluctuation in the unforced and forced flows were similar, and the increased spreading of the velocity fluctuation peak was not observed for the forced flow relative to the unforced flow. Similar to the contours of the developed flow mean velocity, no consistent differences emerged between the unforced and forced conditions for the developed flow velocity fluctuation contours shown in Fig. 3.17.

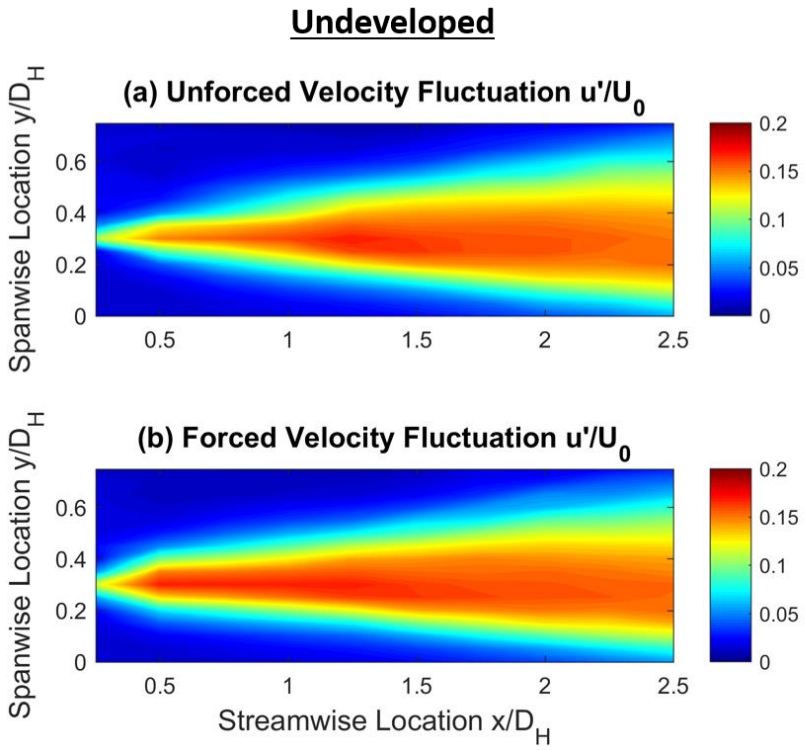

Figure 3.16: Velocity fluctuation contours of (a) unforced and (b) forced undeveloped flow.

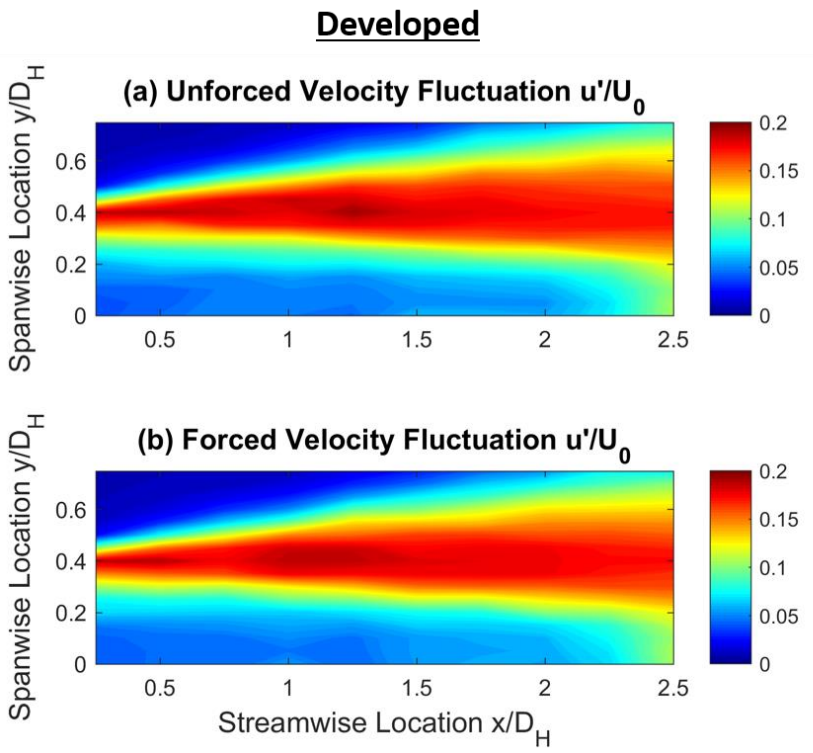

Figure 3.17: Velocity fluctuation contours of (a) unforced and (b) forced developed flow.

Undeveloped flow energy dissipation rate contours for the forced and unforced cases are shown in Fig. 3.18. The most notable differences between the forced flow and the unforced flow in this case appeared near the actuator close to the jet exit, with a maximum energy dissipation rate increase of 53%. But this increase was rapidly attenuated dropping to a 5% increase at x/D_H = 1.25 and 0.6% increase at x/D_H = 2.50. Inside the high velocity region of the undeveloped flow, energy dissipation rate did not appear to be affected. Developed flow energy dissipation rate over the full measurement domain is examined in the unforced and forced contours in Fig. 3.19. Similar to the undeveloped flow, the forced energy dissipation rate reached a maximum at x/D_H = 0.25 and was attenuated with increasing downstream distance. However,

unlike the forced undeveloped flow, the energy dissipation rate was visibly increased within the high velocity region of the flow. Furthermore, the attenuation of the forced energy dissipation rate relative to the unforced flow did not occur as rapidly for the forced developed flow. The spanwise maximum energy dissipation rate at x/D_H = 1.25 was 14% higher in the forced flow, and at x/D_H = 2.50 it was 9% higher in the forced flow. In terms of its impact on bulk flow quantities, high frequency excitation appeared to have the most noticeable effect on the energy dissipation rate within each flow condition, consistent with the findings of Wiltse & Glezer [11]—albeit with reduced magnitude increases.

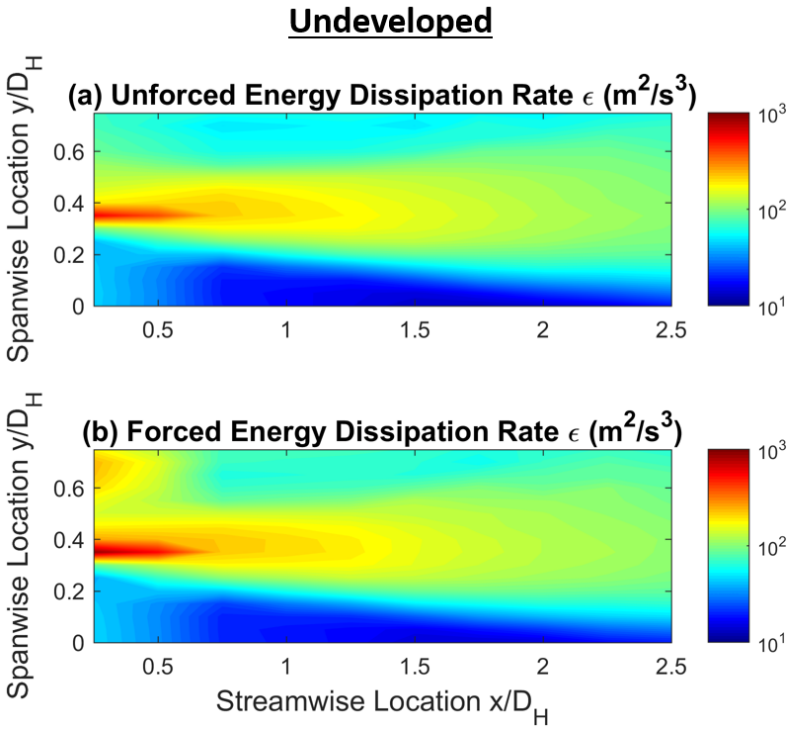

Figure 3.18: Energy dissipation rate contours of (a) unforced and (b) forced undeveloped flow.

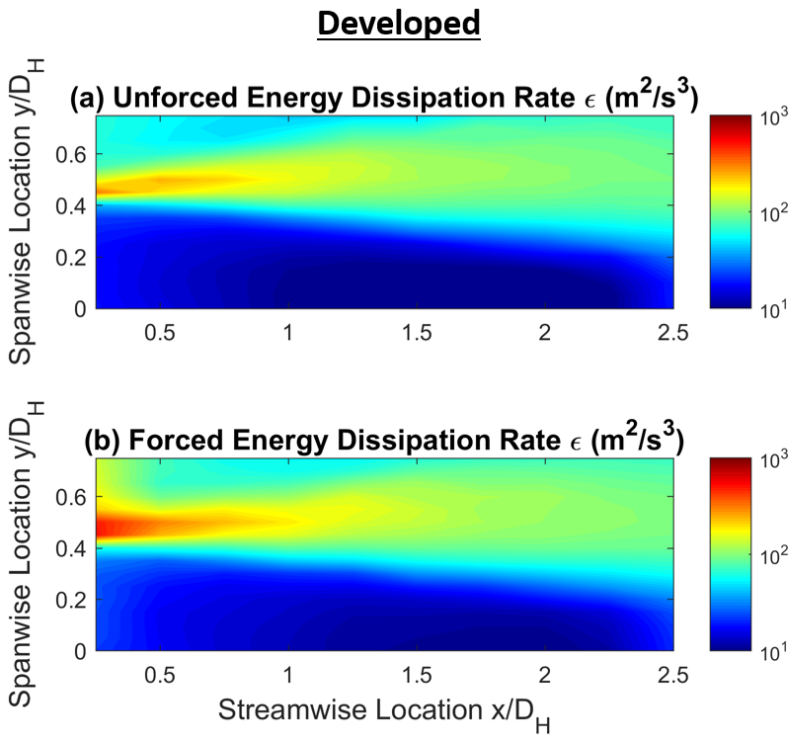

Figure 3.19: Energy dissipation rate contours of (a) unforced and (b) forced developed flow.

The developed flow appeared most similar to the past results of Wiltse & Glezer [11], which was expected because their experiment also involved the use of a developed turbulent flow. Increased stability in the forced mean velocity profiles was not observed in either flow as suggested by Stanek et al. [42], but it is possible that this effect could have been realized with higher amplitude excitation (i.e., an actuator with higher tip velocity). Introduction of the forcing appeared to cause the undeveloped flow to develop more rapidly than the unforced case, which was seen in the increased spreading of the mean velocity and more gradual increases up to the peak velocity fluctuation at measurement locations near the jet exit. However, these effects were not observed in the developed flow. Overall, the introduction of a high frequency excitation source appeared to influence the developed flow more significantly than the

undeveloped flow, contrary to the numerical findings of Cain & Rogers [44]. A more complete analysis of power spectral density of the velocity was necessary to fully assess the influence forcing had on each flow.

3.2.3 Spectral Analysis

The velocity power spectra at each measurement location were analyzed to determine which bands of frequencies were most affected by the excitation. In each of the spectra for the forced flow measurements, there was a discernable peak at the forcing frequency f_e. The magnitude of this spectral peak varied with location in the flow. In the context of nonlinear interactions, the spectral peak magnitude was important because past research has suggested that it is correlated with the magnitude of the $\tilde{r}_{12}$ closure term [29]. As a result, the location of the highest magnitude spectral peak in the flow may also correspond to the location where this closure term is maximized. Furthermore, Vukasinovic, Rusak, & Glezer [37] linked larger magnitude spectral peaks in a high frequency excitation study to the level of energy redistribution, which occurred at other frequencies in the velocity power spectra. Thus, pinpointing the measurement location with the largest magnitude spectral peak had large implications on the direction of this study.

A contour of spectral peak height is presented in Fig. 3.20 for the forced undeveloped and developed flows. For the undeveloped flow (Fig. 3.20(a)), the spectral peak attained a maximum of $1.80 \cdot 10^{-3}$ m^2/s^2 at $x/D_H = 0.25$, $y/D_H = 0.20$. This spanwise location did not align with the location of the maximum energy dissipation rate ($y/D_H = 0.35$), as the results of Wiltse & Glezer [11] would suggest. This raised

the question of whether determining the location of the maximum increase in energy dissipation rate was a comprehensive indicator of the effects of excitation at that location. The magnitude of the spectral peak decreased with downstream distance, with the spanwise maximum decreasing by 94% between x/D_H = 0.25 and x/D_H = 2.50. A contour of the spectral peak magnitude in the developed flow is shown in Fig. 3.20(b). The largest spectral peak observed in the flow at x/D_H = 0.25 and y/D_H = 0.40 was $6.5 \cdot 10^{-3}$—361% higher than the maximum observed in the undeveloped flow. Similar to the undeveloped contour, the maximum spectral peak did not coincide to the location of maximum energy dissipation rate at the closest measurement location. The degradation of the developed maximum spectral peak was similar to that of the undeveloped flow, dropping by 92% from x/D_H = 0.25 to x/D_H = 2.50.

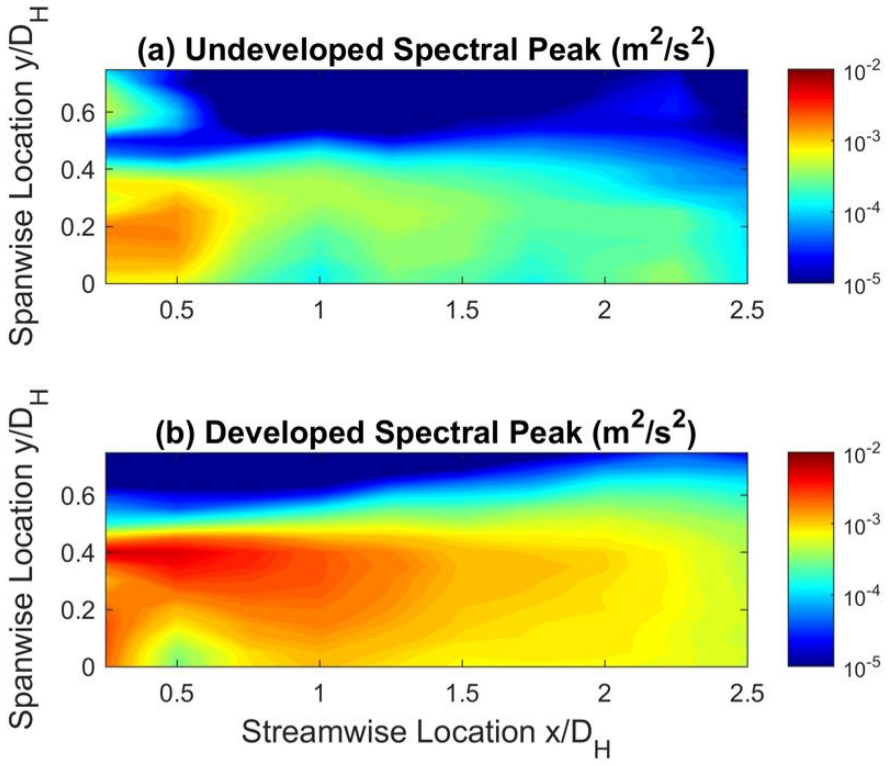

Figure 3.20: Contours of (a) undeveloped and (b) developed flow spectral peak height at f_e.

Further analysis of the velocity power spectra was done to determine the effects of forcing on neighboring frequencies outside of the excitation frequency. In each of the following figures, a local smoothing filter was used with bins of 50 neighboring frequencies to reduce experimental noise. As a result of this filter, the forced spectral peak denoted by f_e remained visible, but was reduced by approximately an order of magnitude. Thus, the spectra shown in the plots below are not representative of the height of the spectral peak relative to the other features of the spectra.

Three spanwise locations along x/D_H = 0.25 were analyzed in detail to provide a sense for how the forced and unforced spectra vary with spanwise location for the undeveloped flow. Velocity power spectra at the jet centerline (y/D_H = 0), the location of maximum magnitude spectral peak (y/D_H = 0.20), and the location of maximum energy dissipation rate (y/D_H = 0.35) are shown in Fig. 3.21. Due to the transitional nature of the flow close to the jet exit, none of the spectra appeared similar to the expected profile of turbulent kinetic energy (e.g. Fig. 1.2). The centerline unforced and forced spectra shown in Fig. 3.21(a) had few appreciable differences other than the presence of the spectral peak for the forced case. The spectra at the largest magnitude spectral peak y/D_H = 0.20 are plotted in Fig. 3.21(b). There was a clear increase in the energy of the forced flow and the unforced flow at low frequencies for this location, but no differences in the high frequency content. This location also corresponded with a greater RMS velocity fluctuation for the forced flow relative to the unforced flow, which naturally resulted in more energy in low frequency, large scale structures. Thus, it appeared that the actuator impacted the spectral content of the undeveloped flow through augmentation of the velocity fluctuation. Forced and unforced spectra for the

location of maximum energy dissipation rate at y/D_H = 0.35 are shown in Fig. 3.21(c). Unlike previous spectra analyzed above, the forced flow showed no appreciable differences between the unforced flow at low frequencies, but energy was increased at high frequencies over the range from approximately 3000 to 6000 Hz. Two peaks appeared at frequencies adjacent to the forcing frequency peak. These peaks perhaps indicated the presence of local interactions between the high frequency excitation and other vortices in the dissipative subrange. However, this phenomenon was distinct from the energy redistribution from large to small scales which was observed by Wiltse & Glezer [11].

Velocity power spectra along the y/D_H = 0.20 are shown in Fig. 3.22 at x/D_H = 0.25, 0.50, and 1.25 to demonstrate the streamwise evolution of the forced and unforced undeveloped flows at the location of the largest magnitude velocity peak. As mentioned above, the forced spectrum at x/D_H = 0.25 (Fig. 3.22(a)) was increased relative to the unforced spectrum at low frequencies up to 600 Hz. The forced spectrum farther downstream at x/D_H = 0.50 (Fig. 3.22(b)) had increased energy over a wider range of frequencies up to 4000 Hz. This increase again coincided with a higher magnitude velocity fluctuation, indicating that the undeveloped forced flow was developing more quickly than the undeveloped unforced flow. Spectra at x/D_H = 1.25 (Fig. 3.22(c)) appeared similar to the turbulent kinetic energy spectrum, which was indicative of flow at a later stage in turbulent development. The unforced and forced spectra were indistinguishable aside from the spectral peak at this location. The slope of the inertial subrange from Kolmogorov's -5/3 Law was noted for reference, suggesting that excitation affected the dissipative subrange of turbulent kinetic energy.

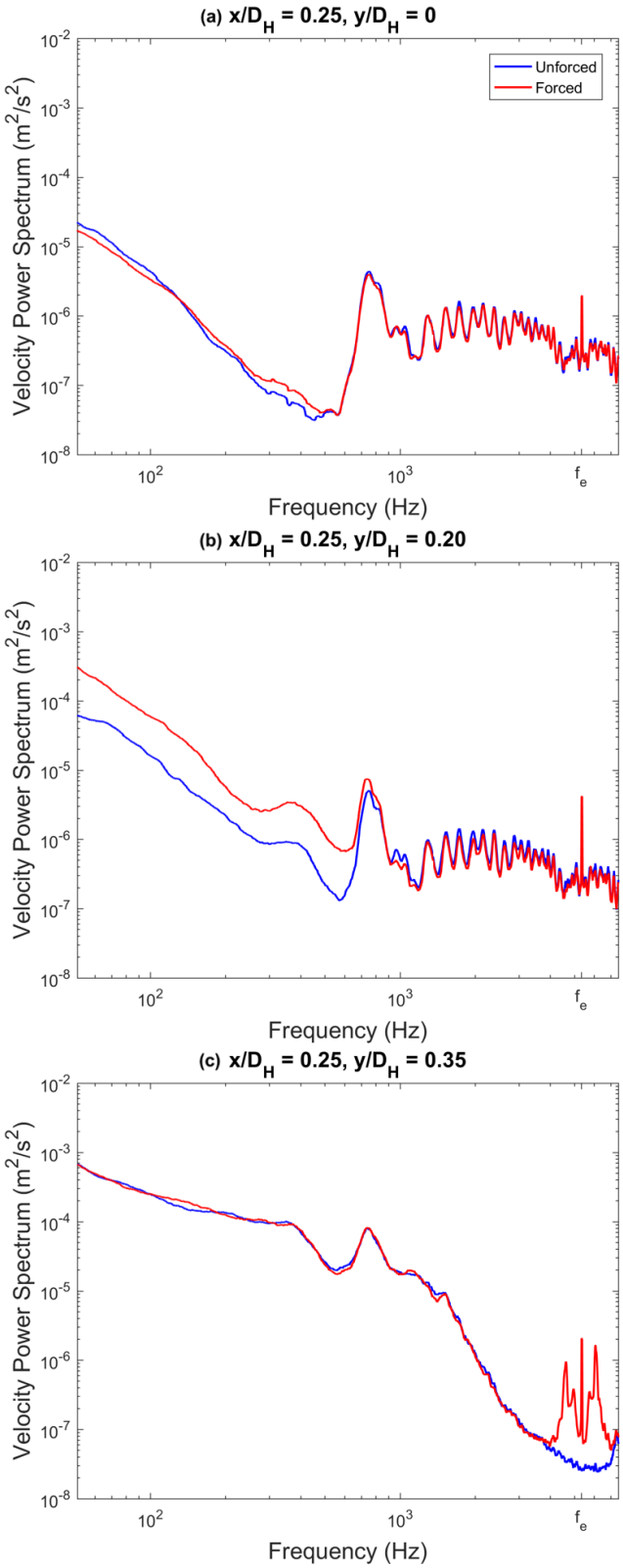

Figure 3.21: Filtered velocity power spectra of the forced and unforced undeveloped flow at x/D_H = 0.25 and (a) y/D_H = 0, (b) y/D_H = 0.20, and (c) y/D_H = 0.35.

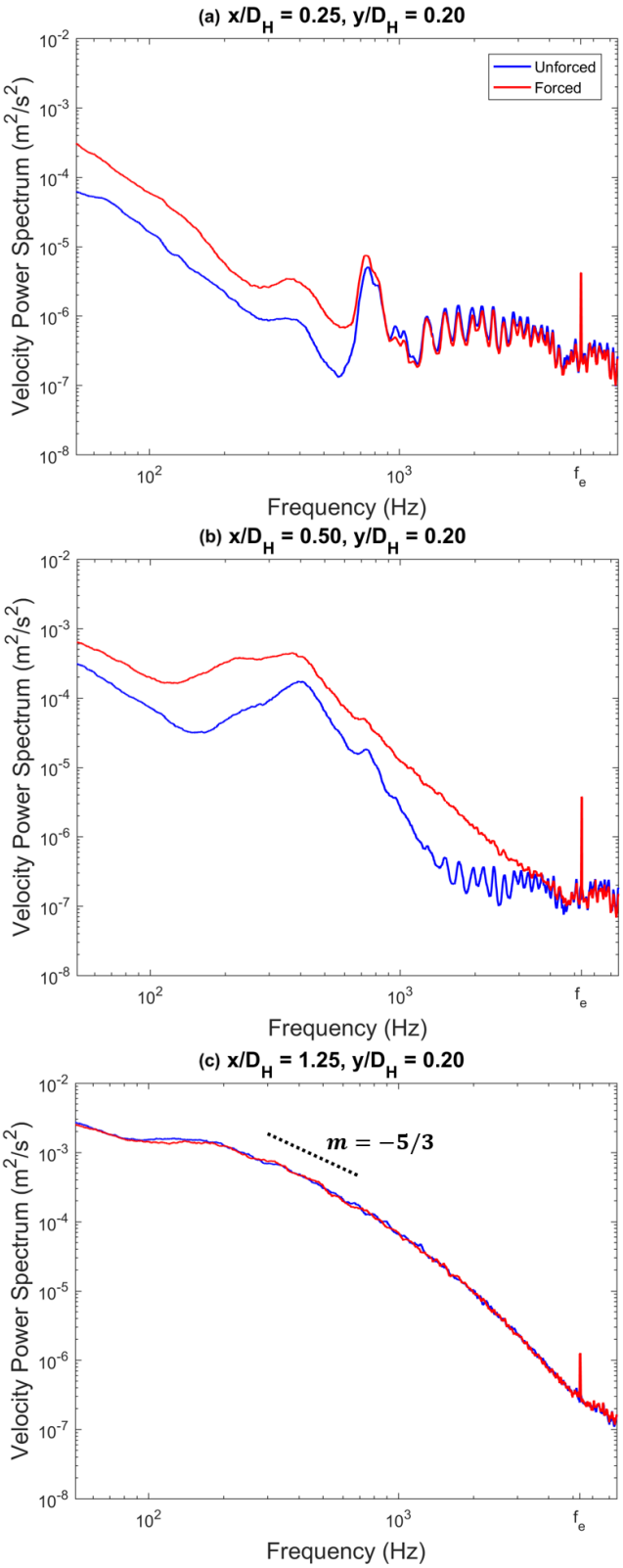

Figure 3.22: Filtered velocity power spectra of the forced and unforced undeveloped flow at y/D_H = 0.20 and (a) x/D_H = 0.25, (b) x/D_H = 0.50, and (c) x/D_H = 1.25.

Once again, points were selected along x/D_H = 0.25 in order to assess the impact of excitation on the developed flow velocity power spectra near the actuator. Figure 3.23 shows the unforced and forced spectra on the centerline, at the location of maximum magnitude spectral peak (y/D_H = 0.40), and the location of maximum energy dissipation rate (y/D_H = 0.45). The location of the inertial subrange given by Kolmogorov's -5/3 Law was apparent at each measurement location this time, which was expected for developed turbulent flow. At the jet centerline (Fig. 3.23(a)), the only discernable difference between the forced and unforced spectra is the forced spectral peak at the excitation frequency. At the location of the largest magnitude spectral peak (Fig. 3.23(b)), the forced spectrum was noticeably increased relative to the unforced spectrum within a range of high frequencies near the forcing frequency. This spreading of the velocity peak to nearby frequencies may have indicated the presence of local interactions at that point. Increased energy in the forced spectra and neighboring frequencies was even more apparent at the maximum energy dissipation rate location Fig. 3.23(c)). This was a common theme for locations corresponding to high forced energy dissipation rate in both the undeveloped and developed flows. Despite relatively lower magnitude spectral peaks at these locations, a large increase in energy dissipation rate seemed to designate the presence of increased energy in vortices corresponding to frequencies nearby the actuation frequency. Like the undeveloped flow, this increases were limited to frequencies within the dissipative subrange and did not indicate the presence of large scale to small scale energy transfer.

The streamwise evolution of the velocity power spectra at streamwise locations was examined in Fig. 3.24 along the spanwise location of maximum magnitude spectral

peak (y/D_H = 0.40). The spreading of energy to frequencies near f_e in the forced spectra was clearly visible near the jet exit at x/D_H = 0.25 (Fig. 3.24(a)). However, as the flow moved farther downstream to x/D_H = 0.50 ((Fig. 3.24(b)), this phenomenon persisted but was not as apparent. At x/D_H = 1.25 (Fig. 3.24(c)), the spreading phenomenon was no longer visible and the only difference between the unforced and forced spectra was the excitation frequency peak. It should be noted that with increasing downstream distance, the disappearance of the spreading phenomenon coincided with decreased magnitude spectral peak.

The magnitude of the spectral peak of the developed flow had a larger maximum and propagated more thoroughly into the measurement domain than the undeveloped flow. Increased energy within the dissipative subrange was apparent in the forced velocity power spectra of both flow conditions at locations corresponding to large increases in the energy dissipation rate. The velocity power spectra of the developed flow were impacted more significantly at these locations than the undeveloped flow. These locations also corresponded to relatively low velocity flow, which was in contrast to Wiltse & Glezer [11] who observed energy redistribution across scales at the centerline where the mean velocity was high. These results indicate that high frequency excitation may have a greater impact on developed flow than on undeveloped flow, which was in direct contrast to past numerical results which found that transitional flow was more responsive to high frequency excitation than fully turbulent flow. In addition, low velocity flow may be more susceptible to excitation than high velocity flow, warranting further investigation of the velocity power spectra of developed flow at lower mean velocities.

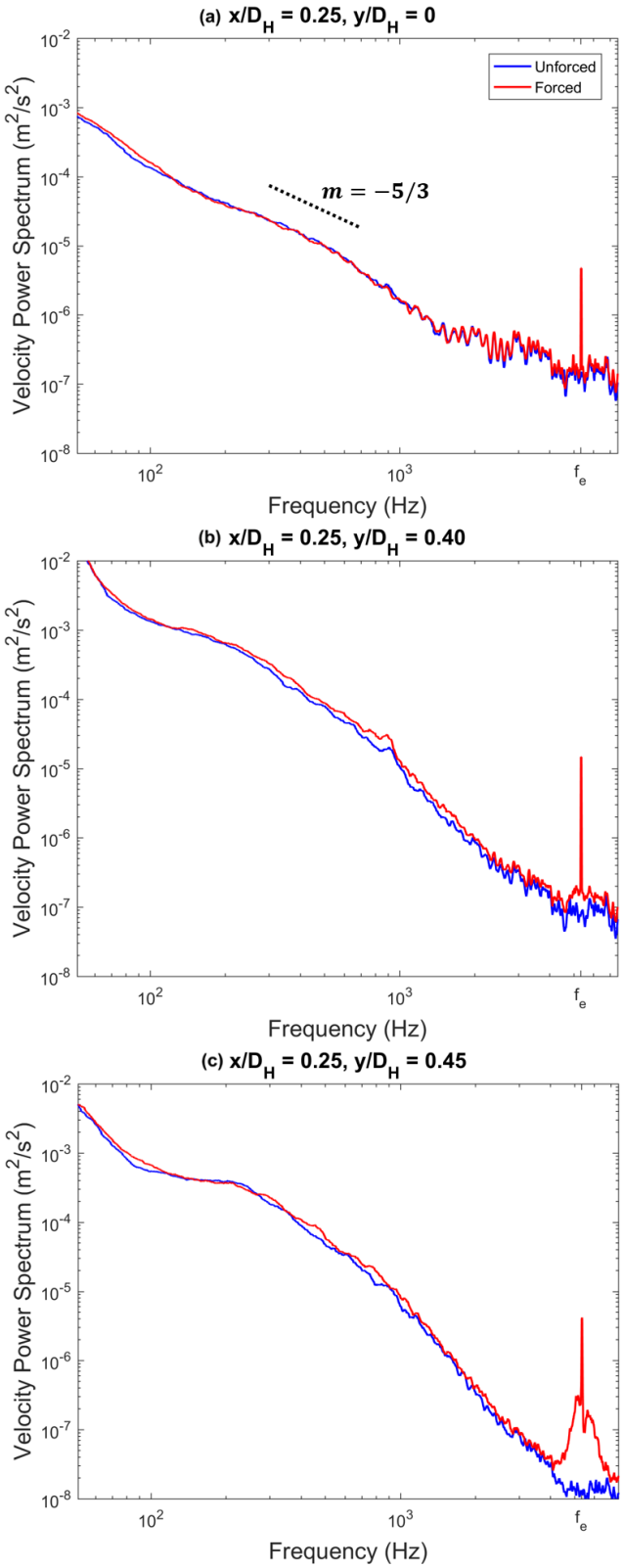

Figure 3.23: Filtered velocity power spectra of the forced and unforced developed flow at x/D_H = 0.25 and (a) y/D_H = 0, (b) y/D_H = 0.40, and (c) y/D_H = 0.45.

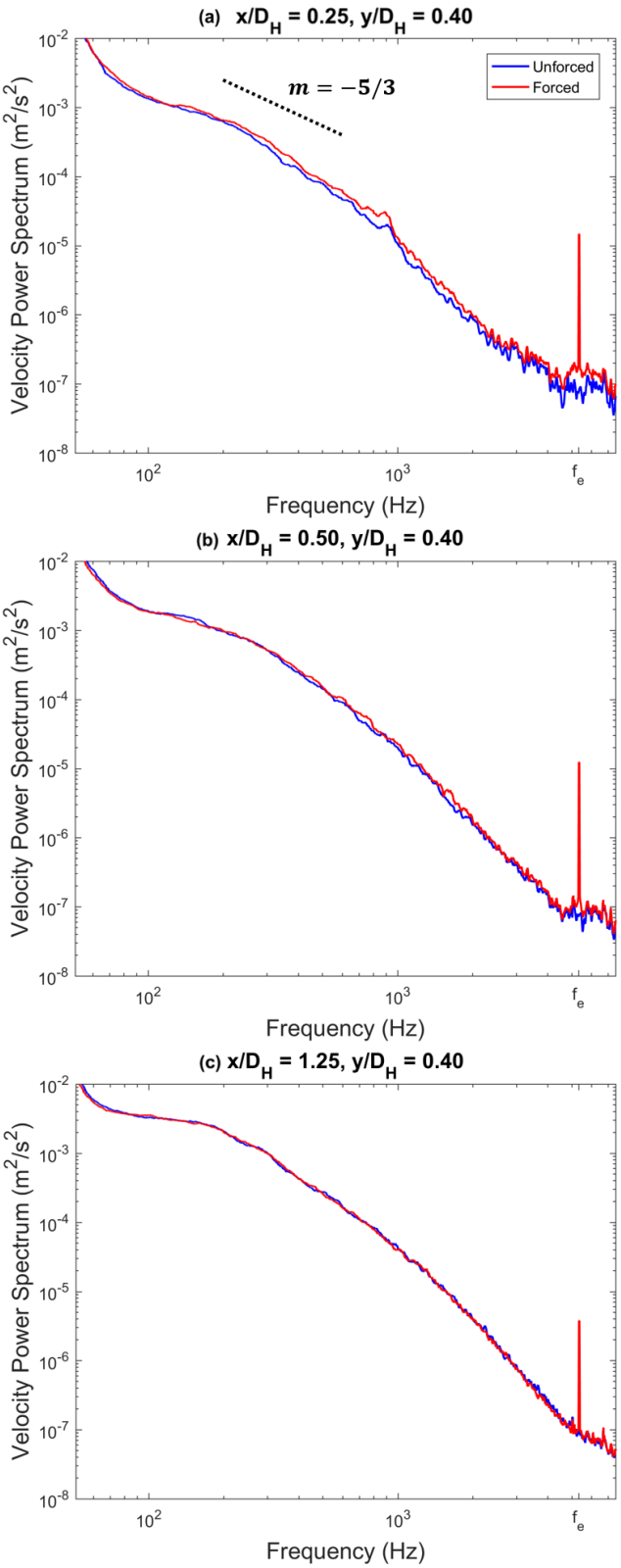

Figure 3.24: Filtered velocity power spectra of the forced and unforced developed flow at y/D_H = 0.40 and (a) x/D_H = 0.25, (b) x/D_H = 0.50, and (c) x/D_H = 1.25.

3.2.4 Mean Velocity Sweep

The receptivity of the developed flow energy dissipation rate and spectral peak magnitude to high frequency excitation relative to that of the undeveloped flow guided the decision to undergo further forcing experiments with the developed flow. The goal of the following experiment was to choose a flow condition with optimal receptivity to actuation before obtaining dual-wire measurements of nonlinear interactions in the flow. The same actuator that was used in undeveloped and developed forcing experiments was operated in the high amplitude mode for developed flow with two flow elongators.

The mean velocity was varied from 4.80 m/s to 10.39 m/s, and measurements of the energy dissipation rate and velocity power spectra were taken to determine how each flow responded to the excitation. Mean velocities lower than 4.80 m/s (Re = 6,600) were not tested to avoid approaching undeveloped flow. Due to the variation in the location of the maximum energy dissipation observed in previous experiments, the single-wire probe was positioned on the jet centerline (y/D_H = 0) at x/D_H = 1.0 to ensure consistency between trials. A plot of energy dissipation rate at the centerline at x/D_H = 1.0 versus flow mean velocity is shown in Fig. 3.25. Higher energy dissipation rate was observed in both the unforced and forced flow as the mean velocity increased. However, as shown in Fig. 3.26, the difference between the forced and unforced energy dissipation rate decreased with increasing mean velocity, indicating that excitation had a greater impact on lower velocity flow than higher velocity flow.

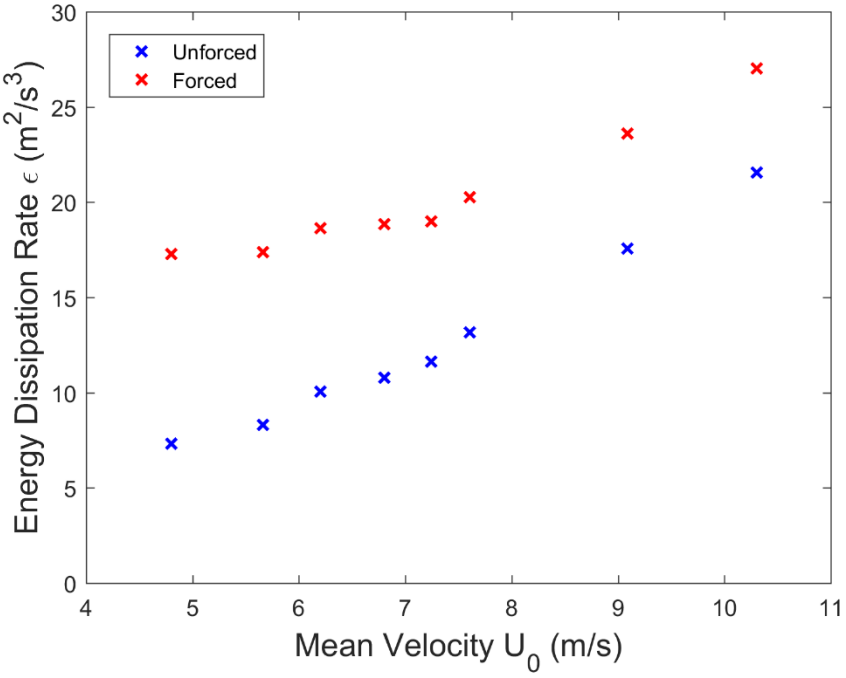

Figure 3.25: Energy dissipation at x/D_H = 1.0, y/D_H = 0 versus mean velocity.

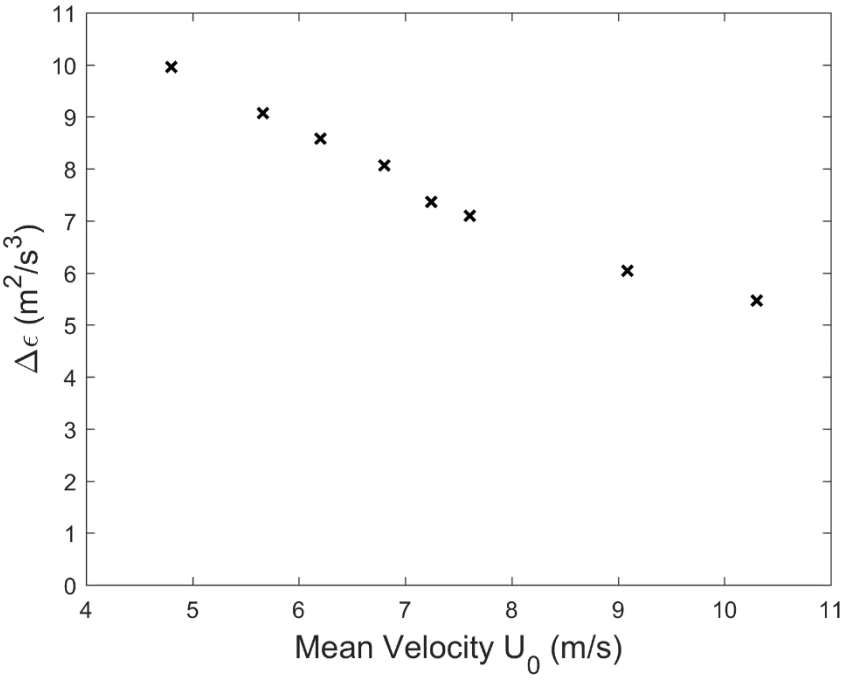

Figure 3.26: Energy dissipation rate difference versus mean velocity.

The magnitude of the spectral peak at the forcing frequency was also dependent on the mean velocity, as shown in Fig. 3.27 at x/D_H = 1.0 on the centerline (y/D_H = 0). As the mean velocity of the flow was increased, the peak at the forcing frequency was reduced. The general trend of the spectral peak variation seemed to follow the variation with the difference in energy dissipation for the forced and unforced flow from Fig. 3.26.

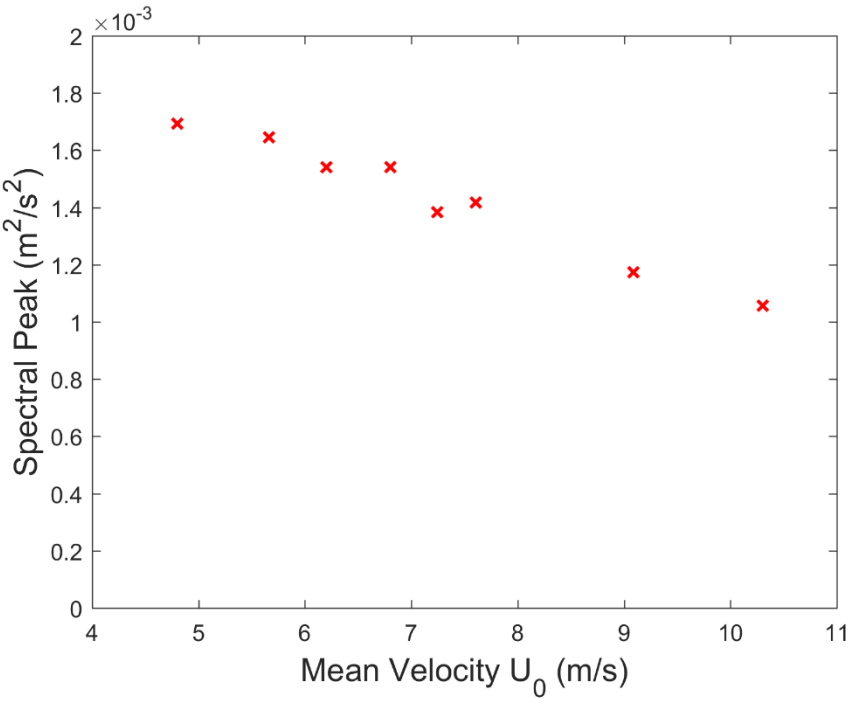

Figure 3.27: Spectral peak height at f_e for x/D_H = 1.0, y/D_H = 0 versus mean velocity.

This result was consistent with past synthetic jet excitation studies which have linked the momentum coefficient—a dimensionless parameter which is directly proportional to the synthetic jet velocity, but inversely proportional to the mean velocity of the flow—to the magnitude of spectral energy redistribution ([38], [39]). It

seems plausible to assume that a similar quantity could be calculated for this study comparing the momentum added to the flow by the vibration of the piezoelectric actuator and the mean velocity of the flow, and that such a quantity could be used as a relative indicator to compare the degree of coupling of dissipative scale forcing to the flow.

3.3 Reduced Velocity Developed Flow

The mean velocity of the turbulent jet was set to 4.80 m/s for this experiment, corresponding to the highest spectral peak and largest difference between forced and unforced energy dissipation rate from the sweep of mean velocities in Subsection 3.2.4. To facilitate dual-wire experiments, a specific measurement location needed to be targeted for the reduced velocity developed flow which contained large gradients and a high magnitude forced spectral peak. The measurement location which was chosen was x/D_H = 1.0, y/D_H = 0.40 due to its location in the middle of the shear layer and the high magnitude spectral peak which was observed in the previous section. All measurements for the reduced velocity developed flow were performed at or adjacent to this location using the dual-wire hot wire probe.

3.3.1 Spectral Analysis

More detailed analysis of the velocity power spectra at lower mean velocities was necessary to determine how the energy at frequencies close to the excitation frequency were impacted by the actuator. A separate actuator was used for this experiment which had a second resonant frequency of 5247 Hz. The actuator was operated in both its low amplitude and high amplitude modes (as defined in Section 2.4)

to determine the effects of excitation amplitude on the flow. The Strouhal number at this mean velocity and excitation frequency was 27.8.

Velocity measurements were recorded for 60 seconds each using the dual-wire probe for the unforced flow, the low amplitude forced flow, and the high amplitude forced flow in order to determine trends in the velocity power spectra. These measurements were also utilized in the calculation of closure terms. A plot of the low amplitude forced spectrum and the unforced spectrum is shown in Fig. 3.28. The unfiltered height of the spectral peak at this location was $2.8 \cdot 10^{-3}$ m^2/s^2. There was a slight decrease in the forced spectrum relative to the unforced spectrum ranging from approximately 30 Hz to 1450 Hz, after which the forced spectra was increased relative to the unforced flow.

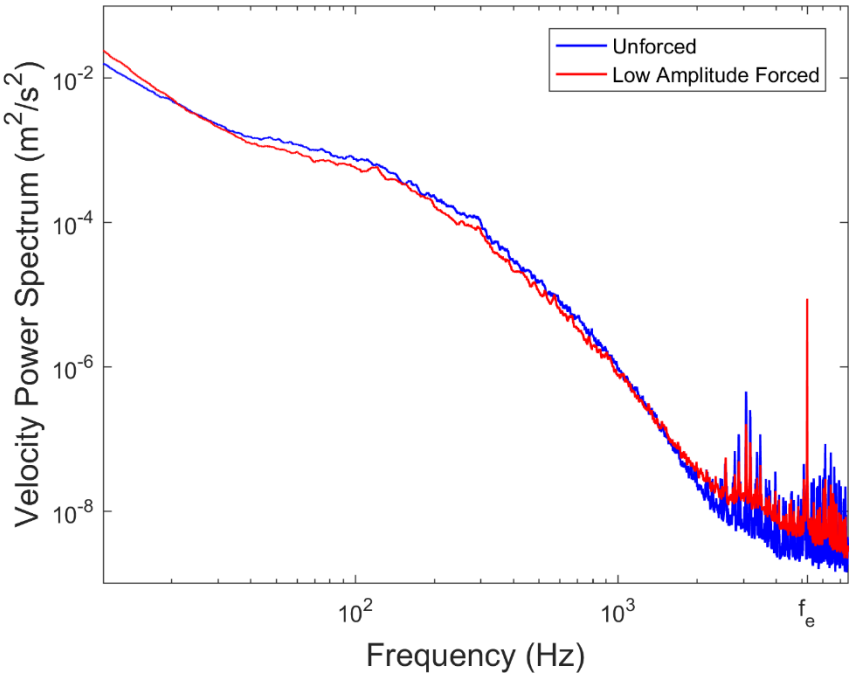

Figure 3.28: Filtered unforced and low amplitude forced velocity power spectra at x/D_H = 1.0, y/D_H = 0.40.

This was distinct from the spectra which were examined in previous sections, and was representative of the Wiltse and Glezer (1998) result for which high frequency excitation caused a redistribution of energy from large scales to small scales. Further, unlike the undeveloped velocity power spectra shown in Fig. 3.21, these differences did not coincide with major differences in the bulk flow quantities such as the mean velocity and velocity fluctuation which could have been an alternative explanation for the altered spectra. Thus, it was concluded that low amplitude forcing was responsible for the transfer of energy between the large and small scales.

Figure 3.29 shows the unforced and high amplitude forced velocity power spectra at x/D_H = 1.0, y/D_H = 0.40. The unfiltered spectral peak height for high amplitude excitation was $3.0 \cdot 10^{-2}$ m^2/s^2, more than an order of magnitude greater than the low amplitude peak. The decrease in the forced spectrum relative to the unforced spectrum was much more pronounced in the high amplitude forcing case than in the low amplitude forcing case. The crossover frequency at which the forced spectrum was increased relative to the unforced spectrum also occurred further into the dissipative subrange at approximately 2300 Hz. It should be noted that limitations in the response frequency of the hot wire anemometer limited the analysis of the forced spectrum beyond 7500 Hz without introducing significant experimental noise. It is possible that the increase in energy at higher frequencies could be better resolved using an anemometer with a higher response frequency. This result further supported the Wiltse & Glezer [11] hypothesis that high frequency excitation leads to decreased energy at the large scales of turbulence and increased energy at the small scales. Furthermore,

maximizing amplitude of the actuator through the voltage signal proved to be necessary to observe these effects in the flow.

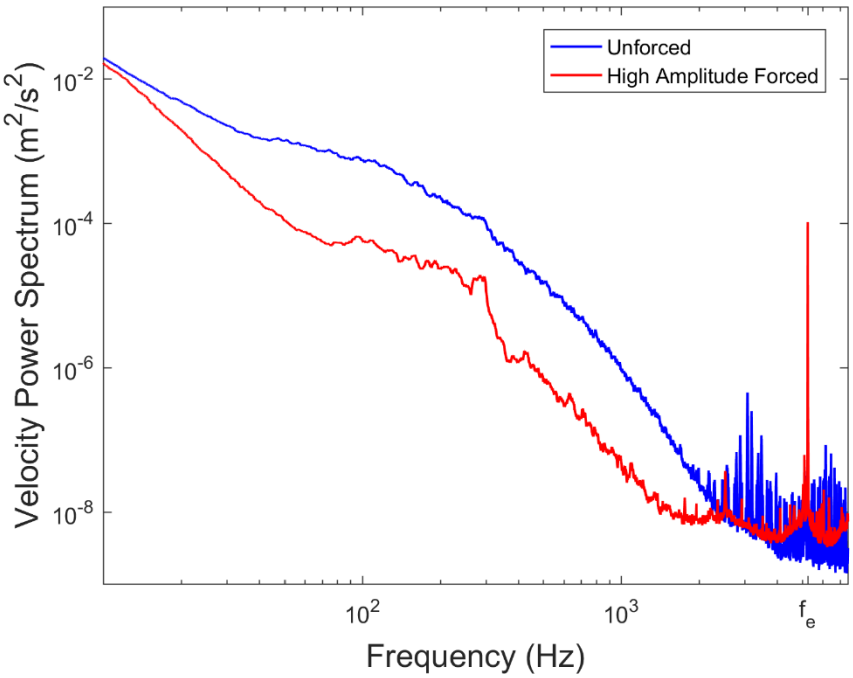

Figure 3.29: Filtered unforced and high amplitude forced velocity power spectra at x/D_H = 1.0, y/D_H = 0.40.

3.3.2 Nonlinear Interactions

Investigation of nonlinearity within the reduced velocity baseline flow was carried out to estimate the magnitude of the eddy viscosity at x/D_H = 1.0. Equations 2.11 and 2.12 were used to estimate the spanwise velocity gradients and calculate the eddy viscosity that minimized error. Figure 3.30 shows the experimentally measured Reynolds stress with the linear Boussinesq approximation with the calculated eddy viscosity of $1.16 \cdot 10^{-4}$ m^2/s. Using this eddy viscosity, it was possible to create a linear

model for the Reynolds & Hussain [13] closure term via Eq. 1.9 and compare it to experimental results for both low and high amplitude forcing.

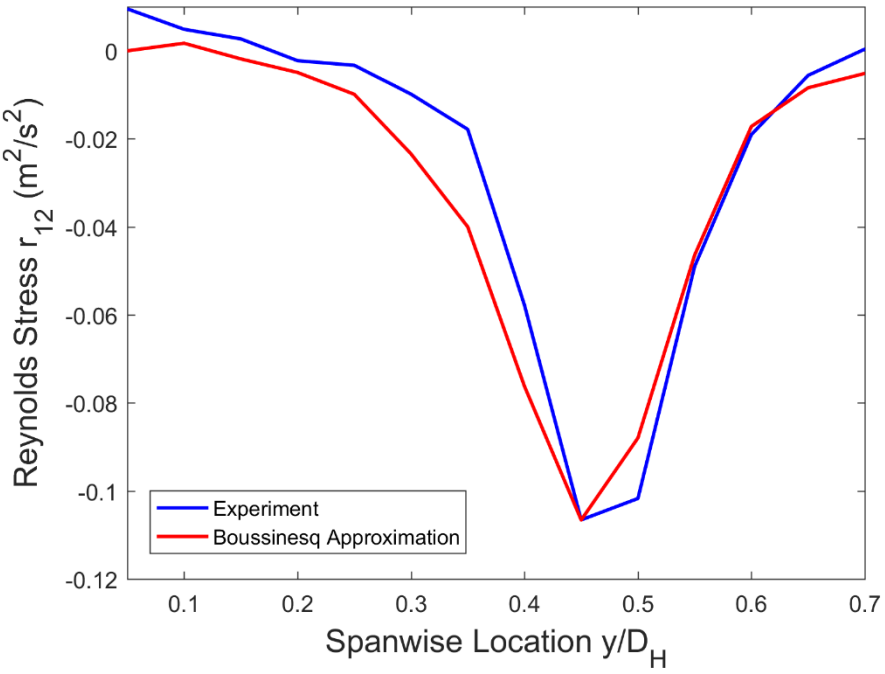

Figure 3.30: Experimental measurements and Boussinesq approximation for the Reynolds stress along x/D_H = 1.0.

The oscillation of the Reynolds & Hussain closure term $\tilde{r}_{12}$ was dependent upon the relative phase of the actuator, thus requiring a large number of samples in order to maintain coherent information about the wave at each phase angle. A phase-averaging process described in Subsection 2.3.2 was needed to reduce experimental noise, which was particularly problematic for the actuator operating in its low amplitude mode. In general, the signal became more coherent when fewer bins were used to complete the phase-averaging, but this risked loss of information about the amplitude and relative phase of the wave.

Signal extraction for low amplitude excitation at x/D_H = 1.0, y/D_H = 0.40 involved 30 minutes of data collection and phase-averaging with 48 bins, corresponding to averaging phase angles separated by 7.5 degrees or less. The experimental measurement and the eddy viscosity model for the $\tilde{r}_{12}$ closure term is shown in Fig. 3.31 for the low amplitude forcing. A sinusoidal fit for each term was overlaid for reference. The approximate amplitude of the experimental closure term was $4.0 \cdot 10^{-4}$ while the approximate amplitude of the eddy viscosity model was almost an order of magnitude lower at $6.7 \cdot 10^{-5}$. The estimated phase offset between the two quantities was 98 degrees.

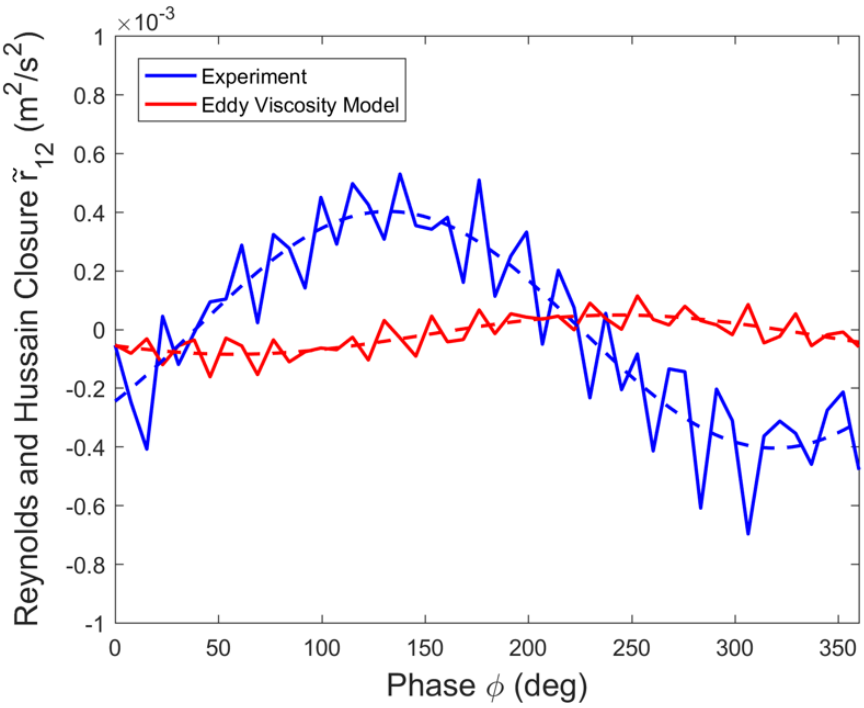

Figure 3.31: Experimental and approximate $\tilde{r}_{12}$ closure term for low amplitude excitation at x/D_H = 1.0, y/D_H = 0.40.

The high amplitude forcing case was phase-averaged using 10 minutes of forced data and 144 phase bins, yielding 2.5 degrees of spacing between bins. The

experimental closure term and the eddy viscosity model for high amplitude excitation are plotted in Fig. 3.32. The experimental and approximate closure terms appeared to correlate with each other much more closely for the high amplitude excitation case than the low amplitude excitation case. The estimated amplitudes of the experimental and approximate closure terms were $4.3 \cdot 10^{-3}$ and $3.9 \cdot 10^{-3}$, respectively, each of which were roughly an order of magnitude higher than the experimental closure term from low amplitude forcing. The phase offset between the two terms was 7 degrees.

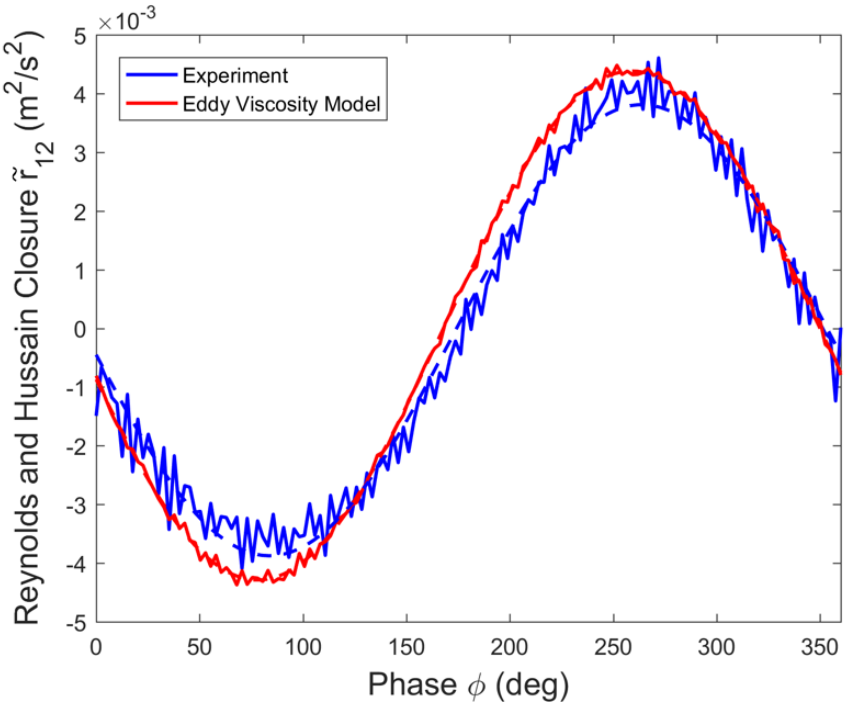

Figure 3.32: Experimental and approximate $\tilde{r}_{12}$ closure term for high amplitude excitation at x/D_H = 1.0, y/D_H = 0.40.

Clearly, amplitude of the actuator was a critical determinant of both energy redistribution in the velocity power spectra and in the magnitude $\tilde{r}_{12}$ closure term. The accuracy of the eddy viscosity model was also improved in the high amplitude forcing

case relative to the case of low amplitude forcing. The usefulness of this model at approximating the nonlinear closure term suggests that the interaction of high frequency excitation with dissipative scale structures does not invalidate the fundamental assumptions put forward by Reynolds & Hussain [13] for use with instability-based excitation studies.

3.3.3 Fluctuation Kinetic Energy Derivation

In the interest of facilitating the use of the eddy viscosity model used above to approximate the oscillating closure term in future theoretical and computational studies, it is useful to derive a formula for the oscillating kinetic energy. The high correlation of the eddy viscosity model with experimental results enables assumptions to be made about the parameters that drive the coupling mechanism between the excitation and turbulent fluctuations of the flow.

Using the Boussinesq approximation (Eq. 1.4) for the Reynolds stress, the mean flow kinetic energy can be written as

$$\frac{1}{2}\frac{d}{dx}\int \bar{u}^3 dy = -\int \overline{-\tilde{u}\tilde{v}}\frac{\partial \bar{u}}{\partial y}dy - \nu_t \int \left(\frac{\partial \bar{u}}{\partial y}\right)^2 dy. \tag{3.1}$$

At this point, the time-averaged momentum can be subtracted to obtain the kinetic energy of the turbulent fluctuations. However, the closure term $\tilde{r}_{12}$ prevents the acquisition of a solution without the use of a linearized model. By substituting in the eddy viscosity model for the closure term, the fluctuation kinetic energy takes the form of

$$\frac{1}{2}\frac{d}{dx}\int(\overline{\tilde{u}^2}+\overline{\tilde{v}^2})\bar{u}dy=-\int\overline{-\tilde{u}\tilde{v}}\frac{\partial\bar{u}}{\partial y}dy \tag{3.2}$$

$$-\nu_t\int\left(\overline{\left(\frac{\partial\tilde{u}}{\partial x}\right)^2}+\overline{\left(\frac{\partial\tilde{u}}{\partial y}\right)^2}+\overline{\left(\frac{\partial\tilde{v}}{\partial x}\right)^2}+\overline{\left(\frac{\partial\tilde{v}}{\partial y}\right)^2}\right)dy.$$

As suggested by Reynolds & Hussain [13], conceptually, the final term in the equation signifies the coupling between the turbulent fluctuations and the coherent wave oscillations.

Using dimensional analysis, it can be shown that the eddy viscosity in this model is dependent on the total kinetic energy K and the energy dissipation rate such that

$$\nu_t \propto \frac{K^2}{\varepsilon}. \tag{3.3}$$

Furthermore, if the organized wave oscillation $\tilde{u}$ is assumed to take the form of a wave equation then

$$\tilde{u}(x,t)=A_0e^{i(kx-\omega t)}. \tag{3.4}$$

where A_0 is the amplitude, k is the wavenumber, and ω is the angular frequency of the oscillation. It follows that

$$\int\left(\overline{\left(\frac{\partial\tilde{u}}{\partial x}\right)^2}+\overline{\left(\frac{\partial\tilde{u}}{\partial y}\right)^2}+\overline{\left(\frac{\partial\tilde{v}}{\partial x}\right)^2}+\overline{\left(\frac{\partial\tilde{v}}{\partial y}\right)^2}\right)dy\propto {A_0}^2 \tag{3.5}$$

$$\nu_t\int\left(\overline{\left(\frac{\partial\tilde{u}}{\partial x}\right)^2}+\overline{\left(\frac{\partial\tilde{u}}{\partial y}\right)^2}+\overline{\left(\frac{\partial\tilde{v}}{\partial x}\right)^2}+\overline{\left(\frac{\partial\tilde{v}}{\partial y}\right)^2}\right)dy\propto\frac{K^2{A_0}^2}{\varepsilon} \tag{3.6}$$

Of course, other proportionalities could be derived for the coupling between the wave oscillations and the turbulent fluctuations.

The proportionalities derived in Eq. 3.6 coincided with experimental results reported above. The developed turbulent flow had higher total turbulent kinetic energy at each measurement location, and it was found the developed flow was more responsive to high frequency excitation than the undeveloped flow. Additionally, the undeveloped flow had higher energy dissipation near the jet exit than the developed flow with and without forcing. Finally, higher amplitude induced oscillations corresponded to transfer of energy from large scale structures to small scale structures and resulted in good agreement between the experimentally measured $\tilde{r}_{12}$ and the eddy viscosity model. These findings support the dependencies suggested by Eq. 3.6 for factors that influence the magnitude of coupling between the induced oscillations and turbulent fluctuations.

Chapter 4 – Conclusions

This thesis sought to extend some of the theories which guided early instability-based flow control studies to a new area of active flow control research. Experiments in high frequency excitation up to this point have left many questions unanswered regarding the physics behind the effects of high frequency forcing and the responsiveness of different types of flow to high frequency excitation sources. The experimental results of this study provide insight into the basic trends associated with high frequency forcing and will serve as an important data set for development of rigorous theories and validation of numerical simulations to capture such effects in more complex systems.

The major findings of this thesis were:

i. Developed flow was found to be more receptive to high frequency excitation as evidenced by increased energy dissipation rate and higher magnitude power spectral density peaks both near the excitation source and farther downstream. This was contrary to past numerical results.
ii. Redistribution of energy from large scale to small scale turbulent structures supported past results that suggest high frequency excitation is fundamentally different from instability-based excitation.
iii. The eddy viscosity model for the $\tilde{r}_{12}$ closure term closely agreed with experimental measurements of flow under direct excitation, despite the inherent assumption that the model is not valid when excitation interacts with background turbulence.

4.1 Discussion

The turbulent jet setup, piezoelectric actuator excitation source, and instrumentation in this study were similar to past high frequency excitation studies, raising the question of why energy distribution in the velocity power spectra only occurred at a relatively low Reynolds number. One possible explanation is that the turbulent jet used in this study had a hydraulic diameter which was 33% shorter than the jet used by Wiltse & Glezer [11], enabling the larger jet to achieve higher Reynolds number flow for lower mean velocities. This combination of high Reynolds number, low mean velocity flow may have been a helpful combination for the effects of high frequency excitation, given that the vortices injected into the flow by the actuator are expected to interact with vortices of similar length scale. Further study investigating the variation in the effects of high frequency excitation with Reynolds number and Strouhal number would be useful for the expansion of the field.

An important finding in this study was that for high amplitude direct excitation of the dissipative subrange, the eddy viscosity model was found to have high correlation with the forced oscillating closure term. A fundamental assumption in the derivation of this term in the triple decomposition Navier-Stokes equations was that the wave motion induced by excitation did not impact the background turbulence. One of the unique aspects of high frequency excitation is that it is capable of directly interacting with structures as small as the dissipative subrange, which would seemingly cause the premises on which this derivation was based to break down. However, a simple linear eddy viscosity model which was originally intended for use with

instability-based active flow control had remarkably close agreement with experimental measurements of the wave oscillating closure term. This finding could have significant implications for the future of numerical and theoretical studies hoping to model active flow control with a high frequency excitation source.

Dimensional analysis of the coupling between the induced wave oscillations and the turbulent fluctuations indicated that the magnitude of coupling was directly proportional to the square of total turbulent kinetic energy and the amplitude of the induced oscillation but indirectly proportional to the energy dissipation rate. While other proportionalities can be derived, those presented here aligned well with experimental results comparing of the effects of excitation on the undeveloped and developed flows. The total turbulent kinetic energy was higher in the developed flow than the undeveloped flow. In addition, despite increased energy dissipation rate being one of the most significant effects of forcing, the energy dissipation rate in the undeveloped flow was higher than that of the developed flow both with and without applied forcing. Furthermore, raising the amplitude of the oscillation produced by the actuator resulted in higher redistribution of energy from large scales to small scales.

4.2 Future Work

A question which remains open within the area of high frequency excitation is whether or not excitation near the end of the dissipative subrange can be an effective form of flow control. One of the largest issues with piezoelectric excitation sources such as the actuator used in this study is the fact that resonant-based devices are not suited for investigating the effects of excitation frequency. However, the potential does

exist for the realization of Kolmogorov scale excitation in other forms of excitation sources. Pulsed plasma actuators possess the capability to achieve excitation frequencies well into the kHz range. However, instrumentation for such a study could prove challenging. Hot wire anemometers are ideal for turbulence studies due to their high response frequencies, but hot wire anemometer systems with a response frequencies in the range of tens of kHz are scarce and expensive.

The redistribution of energy from large scale turbulent structures to small scale turbulent structures which was shown in this study provided further evidence that the physics of high frequency excitation are distinct from instability-based excitation, which rely on enhanced turbulent mixing to achieve active flow control. Past studies have indicated that the direct aerodynamic benefits of high frequency excitation sources may outweigh those of instability-based excitation sources. Furthermore, the reliance of instability-based excitation on targeting a specific unstable mode may not be a limiting factor for high frequency excitation, which instead appears to target a wide range of frequencies in the dissipative subrange. These advantages warrant further investigation of high frequency excitation sources in more applied settings.

Additionally, future work should focus on the visualization of turbulent flow under high frequency excitation similar to this study. Past work has suggested that high frequency energy redistribution results in the breakdown of larger structures and an abundance of smaller structures in the flow. Validation of the appearance of the structures which were measured in this study will help to further the field of high frequency excitation. The effectiveness of the eddy viscosity model and the proposed proportionalities for the coupling mechanism of the induced oscillations can be used as

a starting point for the implementation of similar, more robust models to assist CFD visualization of flow with high frequency forcing.

Finally, the relative success of the eddy viscosity model with approximating the form of the experimental $\tilde{r}_{12}$ closure term indicates that it can be used as a starting point for the implementation of more robust models in theoretical and numerical studies in high frequency excitation. The success of this model should lead to adaptation of modified Orr-Sommerfeld equations for high frequency excitation studies as was done previously in the context of instability-based excitation. Further validation of the proportionalities of the coupling term will also be necessary for the creation of a more theoretically vigorous model of the fluctuation kinetic energy.

Bibliography

[1] Seifert, Avi, and Latunia G. Pack. *Oscillatory Excitation of Unsteady Compressible Flows over Airfoils at Flight Reynolds Numbers*. Proc. of 37th AIAA Aerospace Sciences Meeting and Exhibit, Reno, NV. New York: AIAA, 1999. 1-15.

[2] Huang, L. S., L. Maestrello, and T. D. Bryant. *Separation Control Over an Airfoil at High Angles of Attack by Sound Emanating From The Surface*. Proc. of AIAA 19th Fluid Dynamics, Plasma Dynamics and Lasers Conference, Honolulu, Hawaii. New York: AIAA, 1987. 1-6.

[3] Samimy, Mo, Jin-Hwa Kim, Jeff Kastner, Igor Adamovich, and Yurii Utkin. "Active Control of a Mach 0.9 Jet for Noise Mitigation Using Plasma Actuators." *AIAA Journal* 45.4 (2007): 890-901.

[4] Ben-Hamou, Eli, Eran Arad, and Avi Seifert. "Generic Transport Aft-body Drag Reduction Using Active Flow Control." *Flow, Turbulence and Combustion* 78.3-4 (2007): 365-82.

[5] Post, Martiqua L., and Thomas C. Corke. "Separation Control Using Plasma Actuators: Dynamic Stall Vortex Control on Oscillating Airfoil." *AIAA Journal* 44.12 (2006): 3125-135.

[6] Thomas, F. O., A. Kozlov, and T. C. Corke. "Plasma Actuators for Cylinder Flow Control and Noise Reduction." *AIAA Journal* 46.8 (2008): 1921-931.

[7] Bar-Sever, A. "Separation Control on an Airfoil by Periodic Forcing." *AIAA Journal* 27.6 (1989): 820-21.

[8] Collins, Frank G., and James Zelenevitz. "Influence of Sound upon Separated Flow over Wings." *AIAA Journal* 13.3 (1975): 408-10.

[9] Oster, D., I. Wygnanski, B. Dziomba, and H. Fiedler. "On the Effect of Initial Conditions on the Two Dimensional Turbulent Mixing Layer." *Structure and Mechanisms of Turbulence I Lecture Notes in Physics* (1978): 48-64.

[10] Greenblatt, David, and Israel Wygnanski. "The Control of Flow Separation by Periodic Excitation." *Progress in Aerospace Sciences* 36.7 (2000): 487-545.

[11] Wiltse, John, and Ari Glezer. "Direct Excitation of Small-scale Motions in Free Shear Flows." *Physics of Fluids* 10.8 (1998): 2026-036.

[12] Yeh, C., Munday, P., Taira, K., and Munson, M., “Drag Reduction and Control for Flow over a Hump with Surface Mounted Thermoacoustic Actuators,” AIAA SciTech, Orlando, Fl., 2015.

[13] Reynolds, W.C., and A. K. M. F. Hussain. "The Mechanics of an Organized Wave in Turbulent Shear Flow. Part 2. Experimental Results." *Journal of Fluid Mechanics* 54.02 (1972a): 241-58.

[14] Yeung, P. K., James G. Brasseur, and Qunzhen Wang. "Dynamics of Direct Large-small Scale Couplings in Coherently Forced Turbulence: Concurrent Physical- and Fourier-space Views." *Journal of Fluid Mechanics* 283.1 (1995): 43-95.

[15] Dryden, H. L. "Fifty Years of Boundary-Layer Theory and Experiment." *Science* 121.3142 (1955): 375-80.

[16] Wygnanski, I. *Boundary Layer and Flow Control by Periodic Addition of Momentum*. Proc. of 4th Shear Flow Control Conference, Snowmass Village, CO. New York: AIAA, 1997. 1-21.

[17] Schubauer, G. B., and H. K. Skramstad. "Laminar Boundary-layer Oscillations and Transition on a Flat Plate." *Journal of Research of the National Bureau of Standards* 38.2 (1948): 1-31.

[18] Viets, Herman, Michael Piatt, and Mont Ball. *Unsteady Wing Boundary Layer Energization*. Proc. of 5th Atmospheric Flight Mechanics Conference for Future Space Systems, Guidance, Navigation, and Control, Boulder, CO. New York: AIAA, 1979.

[19] Katz, Y., B. Nishri, and I. Wygnanski. "The Delay of Turbulent Boundary Layer Separation by Oscillatory Active Control." *Physics of Fluids A: Fluid Dynamics* 1.2 (1989): 179-81.

[20] Nagib, H. M., P. H. Reisenthel, and D. J. Koga. *On the Dynamical Scaling of Forced Unsteady Separated Flows*. Proc. of AIAA Shear Flow Control Conference, Boulder, CO. New York: AIAA, 1985.

[21] Chun, K. B., and H. J. Sung. "Control of Turbulent Separated Flow over a Backward-facing Step by Local Forcing." *Experiments in Fluids* 21.6 (1996): 417-426.

[22] Nishri, B., and I. Wygnanski. "Effects of Periodic Excitation on Turbulent Flow Separation from a Flap." *AIAA Journal* 36 (1998): 547-56.

[23] Ahuja, K. K., R. R. Whipkey, and G. S. Jones. *Control of Turbulent Boundary Layer Flows by Sound*. Proc. of AIAA 8th Aeroacoustics Conference, Lockheed-Georgia Company, Atlanta, Georgia. New York: AIAA, 1983.

[24] Joslin, Ronald D., and Daniel N. Miller. *Fundamentals and Applications of Modern Flow Control*. Reston, VA: American Institute of Aeronautics and Astronautics, 2009.

[25] Pope, Stephen B. *Turbulent Flows*. Cambridge: Cambridge UP, 2000.

[26] Reynolds, W.C., and A. K. M. F. Hussain. "The Mechanics of an Organized Wave in Turbulent Shear Flow. Part 3. Theoretical Models and Comparisons with Experiments." *Journal of Fluid Mechanics* 54.02 (1972b): 263-88.

[27] Liu, J. T. C. "Nonlinear Development of an Instability Wave in a Turbulent Wake." *Physics of Fluids* 14.11 (1971): 2251-257.

[28] Chan, Y. Y. "Spatial Waves in Turbulent Jets. Part II." *Physics of Fluids* 17.9 (1974): 1667-670.

[29] Reau, N., and A. Tumin. "Harmonic Perturbations in Turbulent Wakes." *AIAA Journal* 40 (2002): 526-30.

[30] Dewan, Anupam. *Tackling Turbulent Flows in Engineering*. Heidelberg: Springer, 2011.

[31] Yeung, P. K., and James G. Brasseur. "The Response of Isotropic Turbulence to Isotropic and Anisotropic Forcing at the Large Scales." *Physics of Fluids A: Fluid Dynamics* 3.5 (1991): 884-97.

[32] Mininni, P. D., A. Alexakis, and A. Pouquet. "Large-scale Flow Effects, Energy Transfer, and Self-similarity on Turbulence." *Physical Review E* 74.1 (2006): 1-13.

[33] Cattafesta, Louis N., and Mark Sheplak. "Actuators for Active Flow Control."*Annual Review of Fluid Mechanics* 43.1 (2011): 247-72.

[34] Bell, D. J., T. J. Lu, N. A. Fleck, and S. M. Spearing. "MEMS Actuators and Sensors: Observations on Their Performance and Selection for Purpose." *Journal of Micromechanics and Microengineering* 15.7 (2005): 153-64.

[35] Glezer, Ari, and Michael Amitay. "Synthetic Jets." *Annual Review of Fluid Mechanics* 34.1 (2002): 503-29.

[36] Wiltse, John, and Ari Glezer. "Manipulation of Free Shear Flows Using Piezoelectric Actuators." *Journal of Fluid Mechanics* 249 (1993): 261-85.

[37] Vukasinovic, B., D. Lucas, and A. Glezer. *Direct Manipulation of Small-Scale Motions in a Plane Shear Layer*. Proc. of 2nd AIAA Flow Control Conference, Portland, Oregon. New York: AIAA, 2004. 1-13.

[38] Vukasinovic, B., Z. Rusak, and A. Glezer. "Dissipative Small-scale Actuation of a Turbulent Shear Layer." *Journal of Fluid Mechanics* 656 (2010): 51-81.

[39] Glezer, Ari, Michael Amitay, and Andrew M. Honohan. "Aspects of Low- and High-Frequency Actuation for Aerodynamic Flow Control." *AIAA Journal* 43.7 (2005): 1501-511.

[40] Xiao, Lin, Zhuo Chen, Chen Feng, Liang Liu, Zai-Qiao Bai, Yang Wang, Li Qian, Yuying Zhang, Qunqing Li, Kaili Jiang, and Shoushan Fan. "Flexible, Stretchable, Transparent Carbon Nanotube Thin Film Loudspeakers." *Nano Letters* 8.12 (2008): 4539-545.

[41] McGrath, Stephen, and Leonard Shaw. *Active Control of Shallow Cavity Acoustic Resonance*. Proc. of 27th Annual AIAA Fluid Dynamics Conference, New Orleans, Louisiana. New York: AIAA, 1996. 1-9.

[42] Stanek, Michael J., Ganesh Raman, John A. Ross, Jessaji Odedra, James Peto, Farouk Alvi, and Valdis Kibens. *High Frequency Acoustic Suppression - The Role of Mass Flow, The Notion of Superposition, And The Role of Inviscid Instability – A New Model (Part II)*. Proc. of 8th AIAA / CEAS Aeroacoustics Conference & Exhibit, Breckenridge, CO. New York: AIAA, 2002.

[43] Freeman, A. P., and H. J. Catrakis. "Direct Reduction of Aero-Optical Aberrations by Large Structure Suppression Control in Turbulence." *AIAA Journal* 46.10 (2008): 2582-590.

[44] Cain, Alan B., and Michael M. Rogers. "High-frequency Excitation of a Plane Wake." *Annual Briefs* (2000): 55-65.

[45] Stanek, Michael J., Miguel R. Visbal, Donald P. Rizzetta, Stanley G. Rubin, and Prem K. Khosla. "On a Mechanism of Stabilizing Turbulent Free Shear Layers in Cavity Flows." *Computers & Fluids* 36.10 (2007): 1621-637.

[46] Dandois, Julien, Eric Garnier, and Pierre Sagaut. "Numerical Simulation of Active Separation Control by a Synthetic Jet." *Journal of Fluid Mechanics*574 (2007): 25-58.

[47] Rajaratnam, N. *Turbulent Jets*. Amsterdam: Elsevier Scientific Pub., 1976.

[48] Melling, A., and J. H. Whitelaw. "Turbulent Flow in a Rectangular Duct." *Journal of Fluid Mechanics* 78.02 (1976): 289-315.

[49] Misri, Isaac, Prakruthi Hareesh, Shuang Yang, and Don. L. Devoe. "Microfabrication of Bulk PZT Transducers by Dry Film Photolithography and Micro Powder Blasting." *Journal of Micromechanics and Microengineering* 22.8 (2012): 085017.

[50] Hareesh, Prakruthi, Isaac Misri, Shuang Yang, and Don L. Devoe. "Transverse Interdigitated Electrode Actuation of Homogeneous Bulk PZT." *Journal of Microelectromechanical Systems* 21.6 (2012): 1513-518.

[51] Copp, Peter. "Swashplateless Helicopter Experimental Investigation: Primary Control with Trailing Edge Flaps Actuated with Piezobenders." Thesis. University of Maryland College Park, 2013.

[52] Sirohi, Jayant, and Inderjit Chopra. "Fundamental Behavior of Piezoceramic Sheet Actuators." *Journal of Intelligent Material Systems and Structures* 11.1 (2000): 47-61.